CUKUROVA UNIVERSITY

INSTITUTE OF NATURAL AND APPLIED SCIENCES

Ph.D. THESIS

Sedat YAYLA

FLOW CHARACTERISTICS OF DIAMOND AND LAMBDA WINGS AT DIFFERENT FLIGHT CONDITIONS

DEPARTMENT OF MECHANICAL ENGINEERING

ADANA, 2009

INSTITUTE OF NATURAL AND APPLIED SCIENCES

UNIVERSITY OF CUKUROVA

FLOW CHARACTERISTICS OF DIAMOND AND LAMBDA WINGS
AT DIFFERENT FLIGHT CONDITIONS

By Sedat YAYLA

A THESIS OF DOCTOR OF PHILOSOPHY

MECHANICAL ENGINEERING DEPARTMENT

We certified that the thesis titled above was reviewed and approved for the award of
degree of the Doctor of Philosophy by the board of jury on 09/12/2009.

Signature: ....   Signature: ....   Signature: ....

Prof. Dr. Beşir ŞAHİN   Assoc. Prof. Dr. .Ahmet PINARBAŞI   Assoc. Prof. Dr. Hüseyin AKILLI

Supervisor   Member   Member

Signature: ....   Signature: ....

Assoc. Prof. Dr. Galip SEÇKİN   Assoc. Prof. Dr. Muammer ÖZGÖREN

Member   Member

This PhD Thesis is performed in Mechanical Engineering Department of Institute of Natural
and Applied Sciences of Cukurova University

Code No:

Prof.Dr. İlhami YEĞİNGİL
Director of institute

ABSTRACT

Ph.D.THESIS

<div style="border:1px solid">

FLOW CHARACTERISTICS OF DIAMOND AND LAMBDA WINGS AT DIFFERENT FLIGHT CONDITIONS

</div>

Sedat YAYLA

DEPARTMENT OF MECHANICAL ENGINEERING
INSTITUTE OF NATURAL AND APPLIED SCIENCES
UNIVERSITY OF ÇUKUROVA

The aim of this study is to investigate the time-averaged flow structure around a nonslender diamond and lambda wing using a laser based 3-dimessional Particle Image Velocimetry (PIV) technique. The flow structure in close region of the stationary diamond wing surface and formation of the vortex breakdown were studied by varying the yaw angle of the wing within the range of $0°≤θ≤15°$ for the angle of attack of $α=7°$ and $10°$.

Secondly, the flow structure in the near-surface and other crosssections of the wing and formation of the vortex breakdown were investigated by varying the angle of attack of the wing within the range of $7°≤α≤17°$.

Finally, a lambda wing is subjected to small-amplitude perturbations over a range of periods to simulate leading-edge vortex control concepts. Perturbations near the inherent frequency of the predominantly unsteady flow event on the stationary wing yield substantial changes of the near surface flow structure. Experimental analyses are composed of time-average patterns of streamlines, contours of vorticity distributions, Reynolds stress correlations, transverse and streamwise velocity components, distribution of fluctuating velocities and turbulent kinetic energy.

Keywords: Diamond Wing, Lambda Wing, PIV, Turbulent Statistics, Yaw Angle.

ÖZ

DOKTORA TEZİ

FARKLI UÇUŞ ŞARTLARINDA ELMAS VE LAMBDA KANATLARIN AKIŞ KARAKTERİSTİKLERİ

Sedat YAYLA

ÇUKUROVA ÜNİVERSİTESİ
FEN BİLİMLERİ ENSTİTÜSÜ
MAKİNA MÜHENDİSLİĞİ ANABİLİM DALI

Bu çalışmada, 3 boyutlu parçacık görüntülemeli hız ölçme tekniği (PIV) kullanılarak düşük süpürme açısına sahip elmas ve lambda kanat üzerindeki ortalama akış yapısı incelenmiştir. Elmas kanat yüzeyine yakın bölgede akış yapısı ve girdap çökmesinin oluşumu hücum açısı $\alpha=7°$ ve $10°$ değeri için kanatların sapma açısı $0°\leq\theta\leq15°$ aralığında değiştirilerek çalışılmıştır.

İkinci olarak, lambda kanat için deneyler üstten ve arkadan görünüş düzlemlerinde gerçekleştirilmiştir. Kanat yüzeyine yakın bölgede ve diğer kesitlerde akış yapısı ve girdap çökmesinin oluşumu kanat hücum açıları $0°\leq\alpha\leq17°$ aralığında değiştirilerek incelenmiştir.

Son olarak, kanat uç girdap kontrol kavramlarını benzeştirmek için, lambda kanat birkaç farklı periyotta küçük salınıma tabi tutulmuştur. Sabit kanat üzerinde çoğunlukla daimi olmayan akış yapısının doğal frekansına yakın değerde kanata salınım hareketi verilmesi halinde yüzeye yakın bölgede ve akış yapısında temel değişiklikler meydana gelmektedir. Deneysel analizler; zaman-ortalama eşdeğer akım çizgileri, girdap eğrileri dağılım konturları, Reynolds stres korelasyonları, akış yönündeki u ve akışa dik yöndeki v hız bileşenleri, çalkantı hız dağılımları ve türbülans kinetik enerjisi gibi akış karakteristiklerinden meydana gelmektedir.

Anahtar Kelimeler: Elmas Kanat, Lambda Kanat, PIV, Sapma Açısı, Türbülans İstatistikleri.

TEŞEKKÜR

NOMENCLATURE

U	: Free stream velocity
C	: Diamond and Lambda wing chord
α	: Angle of attack
θ	: Yaw angle
Λ	: Sweep angle
u'	: Instantaneous streamwise velocity fluctuation
v'	: Instantaneous transverse velocity fluctuation
w′	: Instantaneous vertical velocity fluctuation
$<\omega>$	: Time-averaged vorticity
$<\Psi>$	: Time-averaged streamline
$<V>$	: Time-averaged velocity distribution
$<v>/U$	: Time-averaged component of transverse velocity
x/C	: The dimensionless chord axis
Re_c	: Reynolds number depending on the delta wing chord
u_{rms}	: rms of streamwise velocity fluctuation
v_{rms}	: rms of transverse velocity fluctuation
x	: Distance from the wing apex measured in the free stream direction
y	: Distance from chord axis measured to plane of symmetry of wingspan
L_{VB}	: Distance from apex measured along axis of leading-edge vortex
u′u′	: Streamwise Reynolds stress correlations
v′v′	: Transverse Reynolds stress correlations
w′w′	: Vertical Reynolds stress correlations
TKE	: Turbulent kinetic energy
$<\ >$	: Time-averaged value of quantity

TABLE OF CONTENTS   Page

VII

LIST OF FIGURES Page

X

XI

XIII

1. INTRODUCTION

Many flows in nature and technology involve cases where the free stream velocity is time-dependent (unsteady). Unsteady aerodynamics, separated and vortex-dominated flows are very often observed. A maneuvering Unmanned Combat Air Vehicles are the simplest case, where the time-lag associated with the separated vortices becomes a significant factor affecting the dynamics aerodynamics parameters of Unmanned Combat Air Vehicles.

Delta wings have evolved over the years and are now used primarily on many fighter aircraft. Heron and Myose (2004) stated that these aircrafts become more and more maneuverable, delta wing vortex dynamics and their effects and understanding of the physics of time-dependent unsteady flows have become substantially important. Lee and Ho (1989) observed the typical angle of attack for maximum lift of a delta wing is about 35°, which is much higher than for a two-dimensional airfoil. The delta wing is therefore suitable for highly maneuverable aircraft.

The delta wing vortex dynamics have several variables. Some of these variables include angle-of-attack, leading edge geometry, wing thickness, sweep angle, free stream conditions and Reynolds number. Yaniktepe (2006) reported that the Reynolds number depending on the delta wing geometry has to be defined more precisely due to the effect of vortex breakdown location. Elkhoury (2004) has observed at moderate to high angle-of-attack, an Unmanned Combat Air Vehicle (UCAV) exhibits complex flow structure due to vortex interaction/breakdown, the onset of separation and stall. These features of the flow patterns have received little attention. Elkhoury (2004) reported that the present investigation addresses the degree of interaction of vortices, the onset of vortex breakdown, and the occurrence of a separation as a function of both Reynolds number and angle-of-attack, via dye visualization and quantitative imaging.

Delta wings behave very differently from other wings type because pair of stationary leading edge separation vortices is most of the time present above the wing. On the delta wing, the flow separates along the entire leading edge and produces the leading-edge vortex. The primary advantage of the delta wing flow field

is that stable flow can be maintained over a wide range of attitudes and Mach numbers. A delta wing can also provide high lift coefficients at very large angles of attack. As much as 40% of the total lift is attributed by these leading edge vortices (vortex lift) at high angles of attack. The leading-edge vortices remains stationary on the airfoil because the vorticity originating from the leading edge is balanced by the vorticity transported along the cores of the separation vortices.

Lin (1998) investigated the effect of increasing angle of attack. He recorded that the strength of the primary vortices increases steadily until a brutal disorganization of the structures occurs. A rapid dilatation of the structure, a profound alteration of its velocity field, and the occurrence of large-scale fluctuations and turbulence characterize this phenomenon, known as *vortex* breakdown or vortex bursting. The burst vortex causes an abrupt change in the axial velocity distribution from a jet-like axial velocity profile to a wake-like one. When the breakdown reaches the apex, the delta wing behaves like a bluff body as vortex shedding occurs. Vortex breakdown is an important aerodynamic property for slender delta wings because it affects the induced flow fields and causes the loss of aerodynamic lift forces, leading to stalling of the lifting surfaces. Furthermore, the breakdown may be asymmetrical and/or unsteady, which causes the appearance of asymmetric loading, lateral forces and moments, and induces phenomena such as wing rock.

Darpa (2002) has presented the UCAVs capable of undergoing severe maneuvers would be a major tactical advantage. Future configurations of the UCAVs are presented in Figure 1.1. The assumption is that the maneuverability of all these configurations will be limited by the onset of vortex breakdown and stall phenomenon, which, in turn, dictates both the overall forces and moments on the aircraft. Moreover, with the current trend towards lighter aircraft, an increasingly important limitation will be the onset of vibration and potential failure of aerodynamic surfaces of the UCAV arising from buffeting.
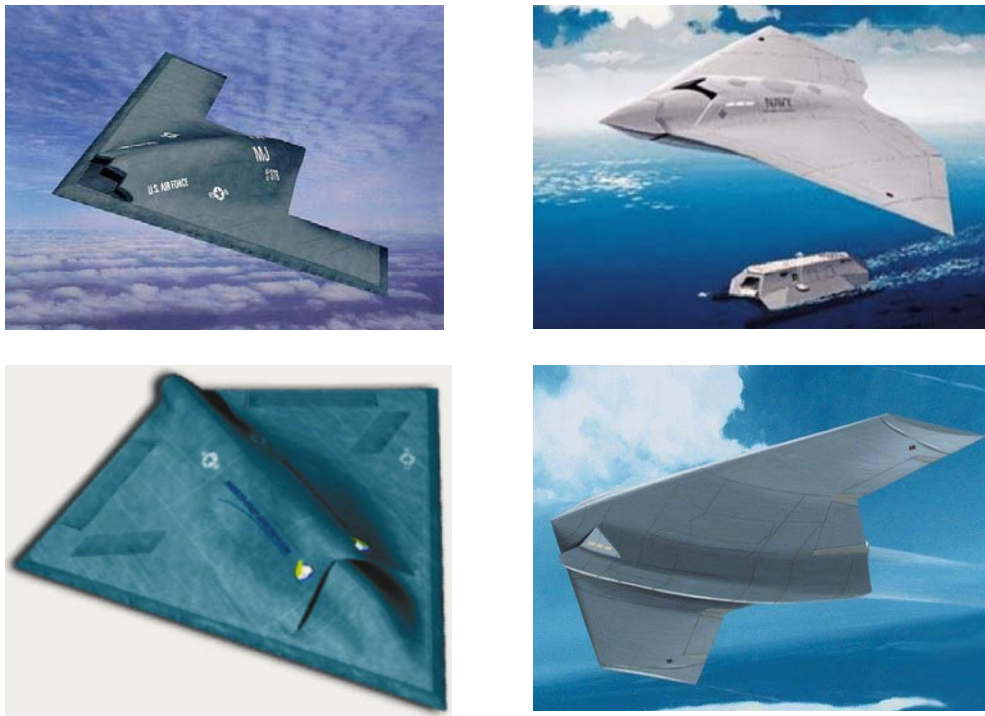
Figure 1.1. Different types of UCAV planforms with small sweep angle Darpa (2002).

Sarpkaya (1995) declared that at high Reynolds numbers (Re=22500), vortex breakdown geometry gradually arrives at its-cone-like form. He considered fourth fundamental type of vortex breakdown (the conical type) in addition to the double-type, sprial and nearly axismmetric type. The swirling flow is highly unstable to spiral disturbances for Reynolds numbers between approximately 1000 and 2000. The axismmetric breakdown evolves either from double helix, or from a spiral, or directly from an axismmetric swelling of the vortex core. He also suggested that the vortex breakdown phenomenon is governed by two basic and conceptually different mechanisms, hydrodynamic instability and finite-transition to sequent state. Kurosaka et al. (2003) investigated the connection between the bubble and the spiral form of vortex breakdown and types of vortexbreakdown as shown Figure 1.2.

Figure 1.2. Bubble and spiral vortex breakdown Kurosaka et al. (2003).

The flow is dominated by two large and counter-rotating vortices at considerable high angle of attack shown in Figure 1.3 (Taylor and Gursul, 2004).
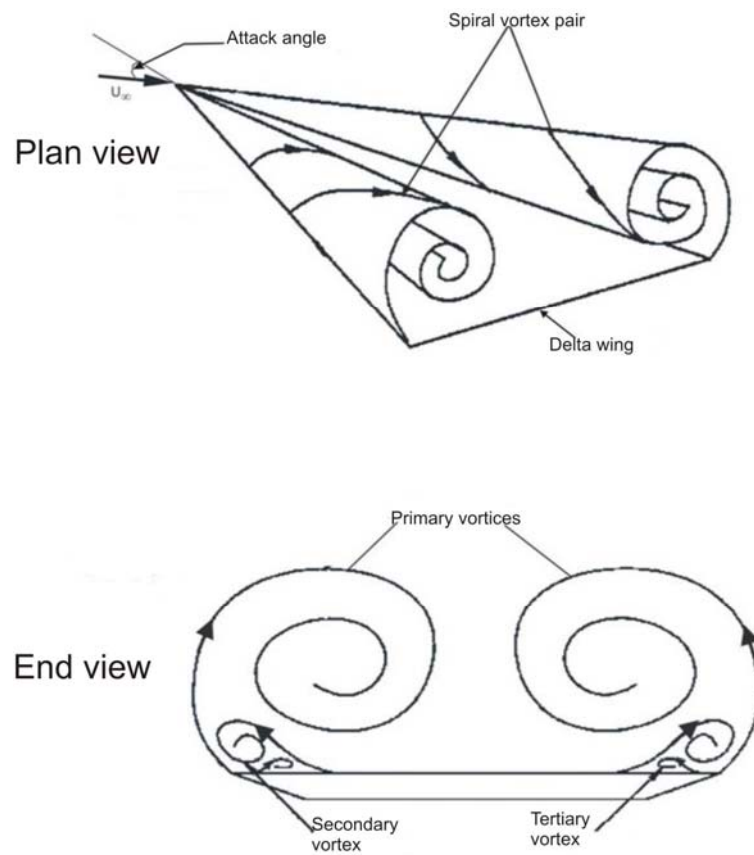
Figure 1.3. Sketch of vortical flow around a delta wing (Taylor and Gursul, 2004).

Rockwell (2000) observed quantitative characterization of unsteady separated flows-structure interactions, which can give rise to vibration and noise generation. Global, instantaneous representation, obtained from high-image-density particle image velocimetry, can provide a basis for identification and classification of flow patterns. An understanding of the physics of the loading is typically based on a form of qualitative flow visualization. Over the years, these approaches have yielded considerable insight and guidance for modeling not only the loading of a stationary body, but also the coupled interaction between a vibrating body, the associated noise generation and surrounding flow.

Yaniktepe and Rockwell (2004) presented based on patterns of averaged velocity and vorticity in the cross flow plane. They showed that the wing of low sweep angle of $\Lambda \leq 50°$ (non-slender) exhibited distinctive features, especially at a higher angle of attack, as a result of the earlier onset of vortex breakdown and a large-scale collapse of the rolled-up, leading-edge vortex structure. They pointed out several interesting features of dye-visualized vortex cores.

The UCAVs are used in variety of missions that require high maneuverability over a wide range of speed. Unsteady aerodynamics of non-slender delta wings, consisted of shear layer instabilities, structure of vortices, occurrence of breakdown, and fluid/structure interactions were extensively reviewed by Gursul et. al. (2005a). They emphasized on the sensitivity of the vortical flow structures with attack angle of the delta wing. Yaniktepe and Rockwell (2004) stated that the non-slender delta wings exhibited distinctive features than slender delta wings especially at a higher angle of attack. Yavuz et. al.(2004) studies the vortical flow structure on a plane immediately adjacent to the surface of non-slender delta wing with $\Lambda=38.7^{o}$ sweep angle using the Particle Image Velocimetry (PIV) technique. Their main finding are;

i.   The time-averaged flow data distributions are symmetric with respect to the plane of symmetry of the delta wing.

ii.   The time- averaged flow data presents well-defined critical points occurring on both side of central axis of the wing. The pattern of instantaneous vorticity

varies rapidly and indicates critical points at different locations comparing the time-averaged streamline topology. But vorticity concentrations are not present in both instantaneous and time-averaged streamline topology. High rate of velocity fluctuations occur in regions of the vortex breakdown.

Gursul et. al. (2005a) reviewed unsteady aerodynamics of nonslender delta wings, covering topics of shear layer instabilities, structure of nonslender vortices, breakdown, maneuvering wings, and fluid/structure interactions. They stated that vortical flows develop at very low angles of attack, and form close to the wing surface. This results in strong interactions with the upper surface boundary layer and in a pronounced dependence of the flow structure on Reynolds number. Vortex breakdown is observed to be much less abrupt compared to breakdown over slender wings. This results in challenges for the precise determination of vortex breakdown location and the interpretation of flow visualizations. One of the distinct features of nonslender wings is the location of the primary attachment zone outboard of the symmetry plane. Reattachment location correlates with the wing stall process and increased buffeting. Dramatic fluid/structure interactions emerge with increasing wing flexibility and result in substantial lift enhancement in the post-stall region. This recently discovered phenomenon appears to be a feature of nonslender wings. Rigid delta wings undergoing small amplitude oscillations in the post-stall region exhibit many similarities to flexible wings, including reattachment and re-formation of the leading-edge vortices. Unusual self-excited roll oscillations have also been observed for free-to-roll nonslender wings.

Yaniktepe and Rockwell (2005) performed experimentally investigations on the flow structures at trailing-edge regions of diamond and lambda type wings. In both wings vortical flow structures in the cross-flow planes of trailing edge vary rapidly with the attack angles. Vortical flow structure and flow topology in regions close to the plane surface of a delta wing are characterized under the trailing-edge blowing by Yavuz and Rockwell (2006). It was found that the trailing-edge blowing can significantly alter the topological flow patterns in close region proximity to the delta wing surface.

Gursul (2005b) reviewed a wide range of unsteady phenomena relevant to slender vortex flows over stationary and maneuvering delta wings and dynamic response of leading edge vortices for maneuvering wings and mechanisms of hysteresis and time lag effects. He discussed the origin, characteristics, and physical mechanisms of these unsteady phenomena and their role in buffeting. He led to reseachers about unresolved and well-understood issues. For example, he stated that although the main features of the unsteady phenomena related to slender delta wings are relatively well understood, many aspects require further study. The details of the shear layer instabilities, steady and unsteady substructures, and transition need to be investigated further. He counted lots of things which should observe in details about unsteady aerodynamics.
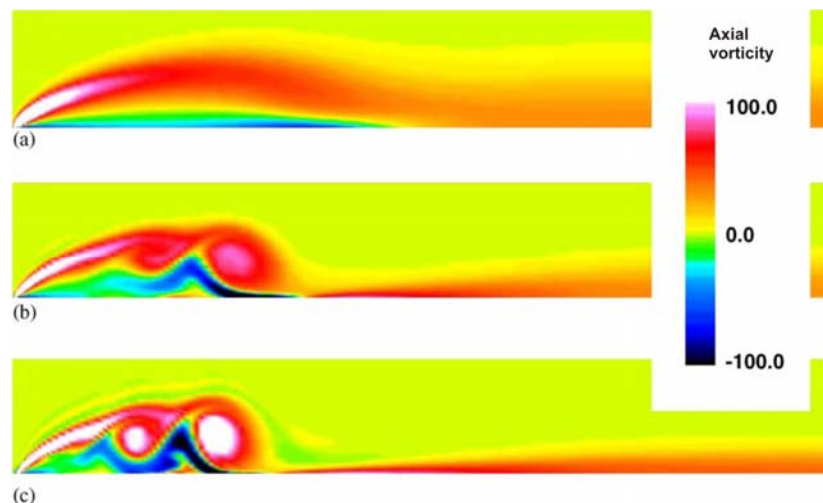
Figure 1.4. Influence of Reynolds number on dual vortex structure (a) Re=10000, (b) Re= 20000, (c) Re=50000 (Gursul et. al. 2005b).

Ol and Gharib (2003) measured the velocity field near the apex region of moderately swept delta wings in a water tunnel, using a version of stereoscopic digital particle imaging velocimetry (PIV). Flow visualization was also used to verify these results shown in Figure 1.5. Delta wings of 50- and 65-deg leading-edge sweep and 30-deg windward-side bevels were tested at Reynolds numbers of $6x10^3$ – $1.5x10^4$. They have stated that at these low Reynolds numbers, secondary leading-

edge vortices were weak, giving way to essentially stagnant flow outboard of the primary leading-edge vortices at the higher angles of attack. It was concluded with increasing angle of attack, the slender delta wing exhibits jet like axial velocity profile of stable primary leading edge vortices, on the other hand the 50° wing fails to have a significant axial velocity peak even for conditions devoid of identifiable vortex breakdown.
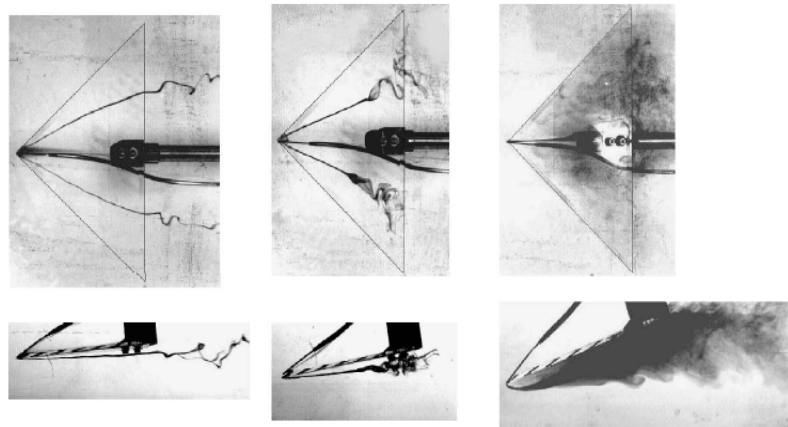
Figure 1.5. Dye streaks following primary LEVs for 50° wing: α = 5, 10, and 20 deg; planform and side views (Ol and Gharib, 2003).

Taylor and Gursul (2004) reported the unsteady vortex flows and buffeting response of a nonslender delta wing with 50-deg leading-edge sweep angle. It was found that there was a profound effect of Reynolds number on the structure of vortical flows. The breakdown of the leading-edge vortices was delayed significantly, and the vortices form more inboard at low Reynolds numbers. The primary vortex is into two separate concentrations of vorticity by the secondary vortex effectively resulting in a dual vortex structure at small incidences. This dual vortex structure diminishes, and a single primary vortex is developed at higher incidences. Unsteady loading, i.e, buffeting, of surfaces of a wing, as described in the previous section, involves flow physics that have certain features in common with vortex breakdown incident upon aerodynamic surfaces such as tails and fins of aircraft.

2. PREVIOUS STUDIES

2.1. Take Shape of Vortex Breakdown

One of the most important formations of vertical flow on the delta wing surface is vortex breakdown. There are many studies, both experimentally and theoretically, for understanding formation mechanism and controlling the vortex breakdown.

During the past four decades, substantial advances, both in theoretical and numerical investigations, have furthered our understanding of the criteria and mechanisms for the onset of vortex breakdown in basic types of flow configurations, which include flow past a highly swept delta wing, swirling flow in a tube, and in a cylindrical vessel.

Levinski et. al. (2001) stated that although the Euler and Navier-Stokes codes can be successfully applied to the simulation of vortex breakdown in flows over delta wings and other simple geometries, they require enormous computing resources to study more complex configurations. Vortex breakdown location over delta wings is not steady and exhibits fluctuations along the axis of the vortices. Menke, (1999) presented that experiments on the nature and source of these fluctuations were carried out. Spectral analysis and other statistical concepts were used to quantify the unsteady behavior of vortex breakdown location obtained from flow visualization. The fluctuations consist of quasi-periodic oscillations and high-frequency low amplitude displacements. The quasi-periodic oscillations are due to an interaction between the vortices, which cause the antisymmetric motion of breakdown locations for left and right vortices. The oscillations are larger and more coherent as the time-averaged breakdown locations get closer to each other as angle of attack or sweep angle is varied.

Being a source of high energy, relatively high vorticity flow, the local static pressure in the vicinity of the vortices is small. Hence, the surface pressure on the top surface of the delta wing is reduced near the leading edge and is higher and reasonably constant over the middle of the wing. The qualitative variation of the

pressure coefficient in the spanwise direction is sketched in figure 2.1. The spanwise variation of pressure over the bottom surface is essentially constant and higher than the freestream pressure (a positive C_p). Over the top of surface, the spanwise variation in the midsection of the wing is essentially constant and lower than the freestream pressure (a negative C_p) (Anderson, 2001).
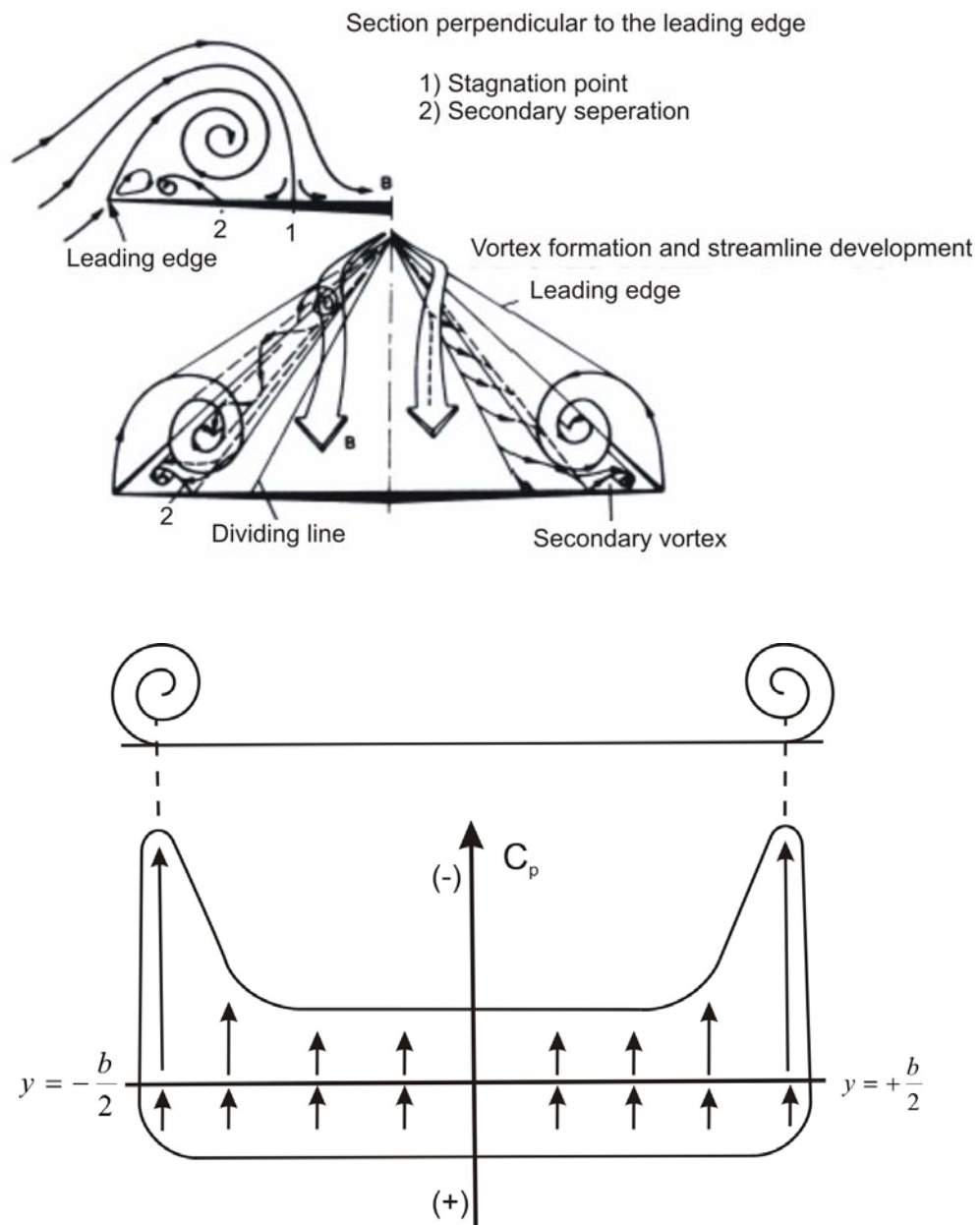
Figure 2.1. Schematic of the subsonic flow field over the top of a delta wing at angle of attack (Anderson, 2001).

The onset of vortex breakdown and stall phenomenon for all classes of aircraft, which are related to the overall forces and moments on the aircraft, can produce localized buffeting. Figure 2.2. shows the simplest case of a delta wing of relatively small sweep angle. The onset of vortex breakdown is indicated in an idealized fashion. The occurrence of large-scale stall-like regions at the wing surface illustrated, which arise in regions between the leading-edge vortices at higher angles of attack.
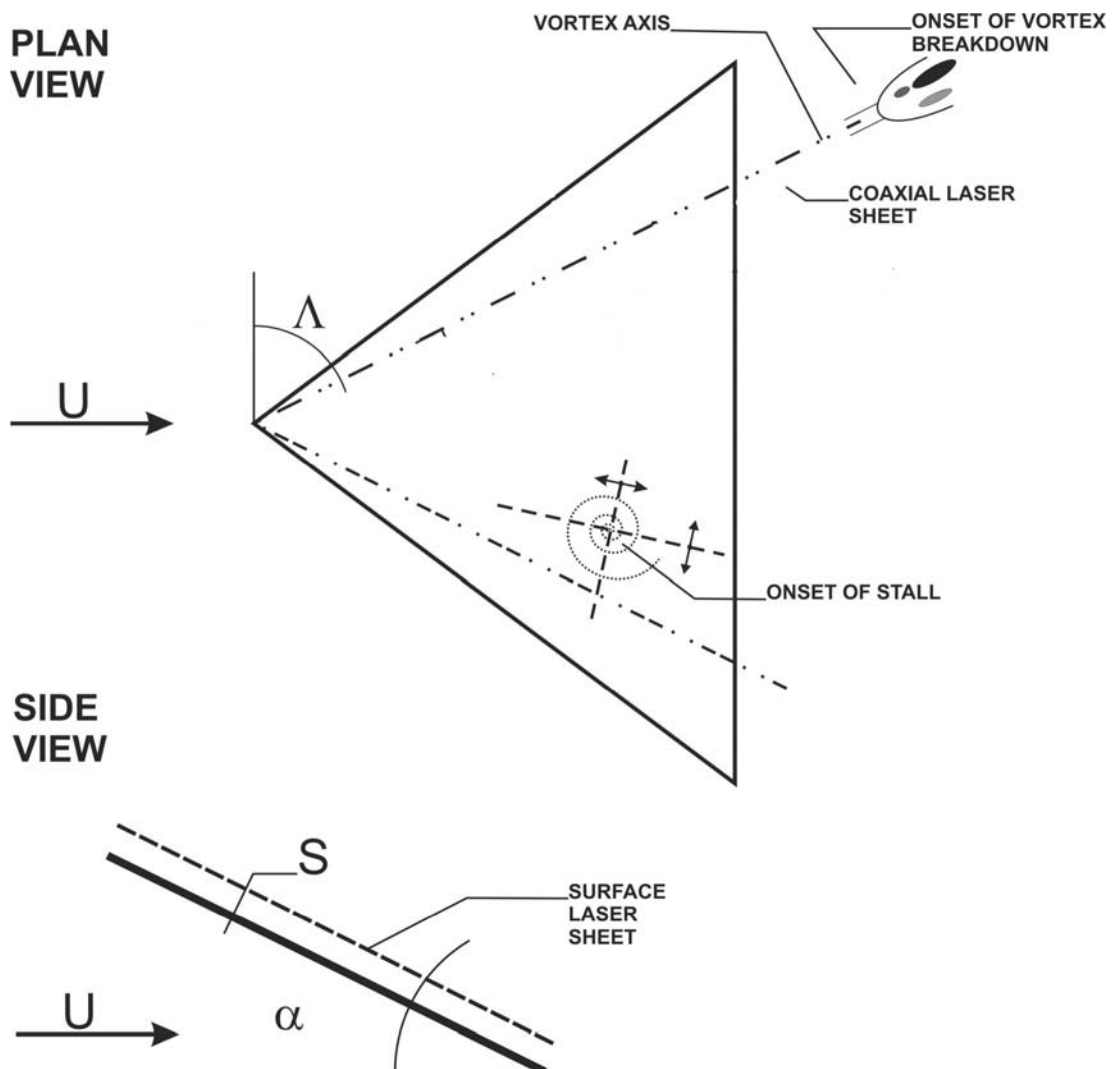
Figure 2.2. Schematic of simple delta wing showing onset of vortex breakdown and stall.

11

Canpolat et al. (2009) observed the change of flow structure on the delta wing depending on angle of attack, α and yaw angle, θ for sweep angle of Λ=40°. The flow characteristics over the delta wing in the plan-view plane was presented for angles of attack such as α= 7, 10, 13, and 17 deg, and yaw angles such as θ= 0, 6, 8, and 15 deg. Dye visualization experiments in the crossflow plane were performed at locations of *x/C*=0.6, 0.8, and 1. On the other hand, for the plan-view measuring planes, the laser sheet was located along the central axes of leading-edge vortices. Examining all dye visualization experiments, there is a symmetrical flow structure on the delta wing in the case of zero yaw angle θ. Also, there was a coherent pair of leading-edge vortices starting from the apex of the delta wing. The structure of these coherent leading-edge vortices decomposes developing vortex breakdown further downstream in the freestream flow direction. Examining all images in the side-view plane, it can be seen that a high-scale Kelvin-Helmholtz vortex structure occurs at the bottom of the unstable flow region, especially for the angles of attack of α=13 and 17 deg. When the delta wing is under the effect of a yaw angle θ, the symmetrical flow structure deteriorates and a vortex breakdown occurs earlier on the windward side of the delta wing as compared with the leeward side. The flow structure close to the surface of the non-slender diamond wing by Yayla et al. (2009) was investigated both qualitatively and quantitatively using dye visualization and the 3-D Particle Image Velocimetry (PIV) techniques. The flow structure and formation of the vortex breakdown were studied by varying the yaw angle of the wing within the range of $0^o \leq \theta \leq 15^o$ for the angle of attack of α=7° and Reynolds number of 10 000. They determined that when the yaw angle was increased, the location of vortex breakdown at one side approached to the wing apex, the other one moved towards the trailing edge. Kurosaka et. al. (2003) experimentally investigated the connection between the bubble and the spiral form of vortex breakdown. In their study; an external disturbance in the form of an azimuthally spinning waveform was imposed in a pipe. The azimuthal wave number was varied by adjusting the phase difference among four oscillating pistons mounted circumferentially on the pipe. By imposing a disturbance of zero azimuthal wave number, a spiral was transformed into a bubble, and this occurred only for selective piston frequencies; the vortex

breakdown which altered from the spiral to the bubble moved upstream, where it remained as a bubble as long as the external disturbance remained.

By varying, systematically and independently, the flow rate and the circulation imparted to the fluid (water) in a slightly diverging cylindrical tube, Sarpkaya (1995) observed three types of vortex breakdown: double helix, spiral, and axisymmetric (bubble). Lucca-Negro and Doherty, (2001) characterized vortex breakdown by a stagnation point on the swirl axis, followed by an abrupt expansion of the centerline dye filament to form the envelope of a bubble of recirculation fluid as seen in Fig. 2.3a. This envelope is nearly axisymmetric over most of its length, but the interior is dominated by low frequency motions. This could be caused by fluid exchange with the outer flow at the downstream end of the bubble. A 'tail' can be observed at the rear. The bubble is also only quasi-steady in axial location. The spiral vortex breakdown is characterized by a rapid deceleration of the dye filament marking the swirl axis, which causes stagnation, and by an abrupt kink, followed by a corkscrew-shaped twisting of the dye as seen in Fig. 2.3b. This latter persists for one or two turns before breaking up into large-scale turbulence (Lucca-Negro and Doherty, 2001). A strong periodicity of the flow pattern is also noticed with the frequency related to the swirl level. A dye filament introduced on the vortex axis is decelerated and expands into a slightly curved triangular sheet. Each half of the sheet is wrapped around the other to form a double helix as seen in Fig. 2.3c. At higher Reynolds numbers, the only characteristic geometric forms are the bubble and the spiral. Similarly, above delta wings, only the bubble and spiral forms have been noted, depending on the angle of attack and the wing aspect ratio.
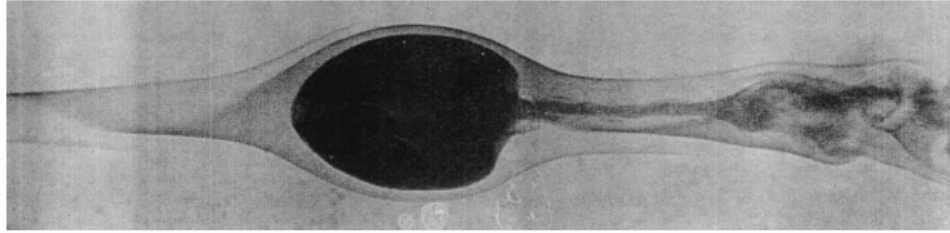
a) Bubble type breakdown
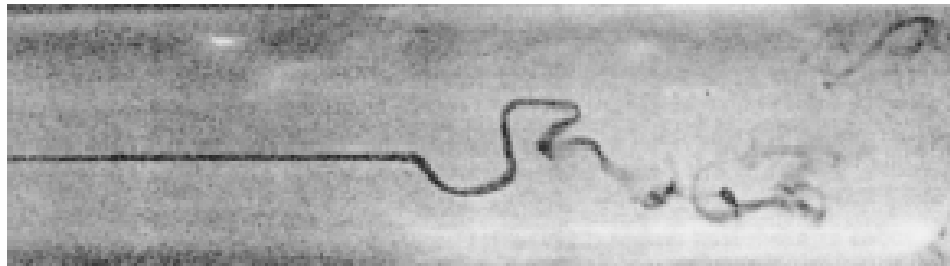
b) Spiral type breakdown
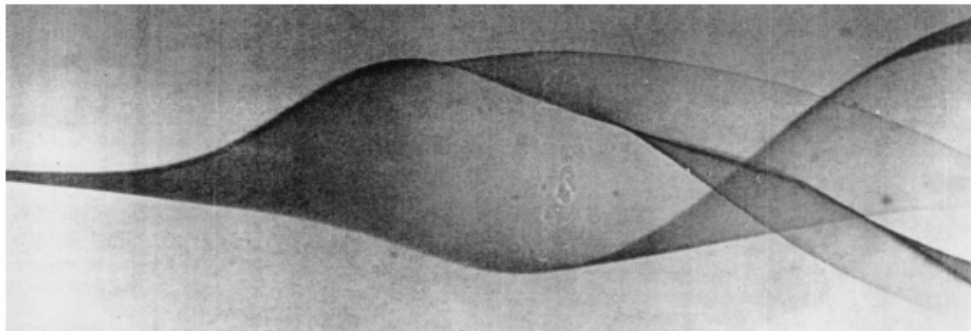
c) Double helix breakdown

Figure 2.3. Types of vortex breakdown in a tube (Lucca-Negro and Doherty, 2001).

2.2. Aerodynamic of Delta Wing having Low-Moderate Sweep Angle

Taylor et all. (2003) have presented the results of a recent investigation into the vortex structure over a non-slender delta wing with leading edge sweep angle, $\Lambda = 50^0$. A flow visualization study in water tunnel experiments has shown profound sensitivity of the vortex structure to Reynolds number. As Reynolds

number was reduced, the trajectory of the vortex core moved inboard toward the wing center-line, and the onset of breakdown was noticeably delayed.

Wang and Zhang (2008) presented that the dye injection and hydrogen bubble visualization techniques were used to investigate the dual-vortex structures, vortex breakdown positions and their spatial distributions for flow over delta wings with Λ = 45°-65° and the emphasis was given on the effects of Reynolds numbers and sweep angles, and their main conclusions were as follows:

(1) The angle of attack α, sweep angle Λ and Reynolds number Re influence the dual-vortex structure significantly. First, the dual-vortex structure can only be generated at small angle of attack and in a narrow range of angle of attack. Secondly, the dual-vortex structure can only be formed when the Reynolds number Re is greater than a critical value. Lastly, the delta wing with Λ= 65° can also generate dual-vortex structure under the present experimental conditions.

(2) The angle θ_{in} decreases with angle of attack α, therefore, θ_{out} is independent of Re and α, and a simple linear relationship between θ_{out} and Λ is proposed. Moreover, both Re and α influence the breakdown locations of dual-vortex structure.

(3) The vortex breakdown location moves upstream gradually with the increase of α, and downstream with the increase of Λ, thus the high sweep delta wing can persist the existence of leading-edge vortex structure at higher angle of attack.

Yaniktepe and Rockwell, (2005) were presented that the abrupt change in sweep angle, which is characteristic of both diamond and lambda planforms, along with the different trailing edge configurations of these planforms, yields distinctive features of the patterns, relative to the case of a simple delta wing. The streamline topology for both the diamond and lambda planforms show, at low angle of attack, a focus (apparent center) of a spiral pattern of streamlines at the leading edge, rather than inboard of the leading edge. At moderate angle of attack, this focus shifts inboard of the leading edge, and at high angle attack, where a large scale separated zone occurs adjacent to the wing surface; the pattern of streamline topology loses its ordered definition. Furthermore, the occurrence of saddle points (apparent

intersection of streamlines) is influenced by a global effect of the trailing-edge configuration. For the lambda planform, a saddle point is located outboard of the leading edge; for the diamond planform, it is absent.

Hebbar et al. (2000) presented the determination of the influence of Reynolds number on vortex interactions/trajectories, and breakdown. It was found that there was a significant influence of Reynolds number. Specifically, with the increase of flow, Reynolds number the strake and wing vortex trajectories tend to move outboards and closer to the model surface, and the vortex breakdown location moves forwards toward the apex of the model. The intertwining or coiling-up feature of the vortex interaction phenomenon becomes less dominant and disappears altogether at high Reynolds numbers.

The other phenomenon for the delta wing is the side slip angle (yaw angle). The influence of sideslip on the flow about a sharp-edged biconvex delta wing of a unit aspect ratio is investigated using flow visualization techniques as well as pressure and force balance measurements. Verhaagen and Naarding (1989) reported at lower angles of sideslip, the vortex flow and pressure distribution was additionally influenced by asymmetric bursting. The flow about the yawed wing was computed using a slender-body free-vortex-sheet method. Good agreement was obtained with experimental data on the part of the wing away from the apex and trailing edge.

Yavuz et al. (2004) investigated the near-surface topology and flow structure for a wing of sweep angle $\Lambda=38.7°$, including the effect of wing perturbations and transient motion of the wing; a near-surface technique of PIV was employed. Gursul et. al. (2005) reviewed unsteady aerodynamics of nonslender delta wings, covering topics of shear layer instabilities, structure of nonslender vortices, breakdown, maneuvering wings and fluid/structure interactions. They stated that vortical flows develop at very low angles of attack, and form close to the wing surface. This results in strong interactions with the upper surface boundary layer and in a pronounced dependence of the flow structure on Reynolds number were shown in Figure 2.4. Vortex breakdown was observed to be much less abrupt compared to breakdown over slender wings. This results in challenges for the precise determination of vortex breakdown location and the interpretation of flow visualizations. One of the distinct

features of nonslender wings is the location of the primary attachment zone outboard of the symmetry plane. Reattachment location correlates with the wing stall process and increased buffeting. Dramatic fluid/structure interactions (Figure 2.4.) emerge with increasing wing flexibility and result in substantial lift enhancement in the post-stall region. This recently discovered phenomenon appears to be a feature of nonslender wings. Rigid delta wings undergoing small amplitude oscillations in the post-stall region exhibit many similarities to flexible wings, including reattachment and re-formation of the leading-edge vortices. Unusual self-excited roll oscillations have also been observed for free-to-roll nonslender wings.
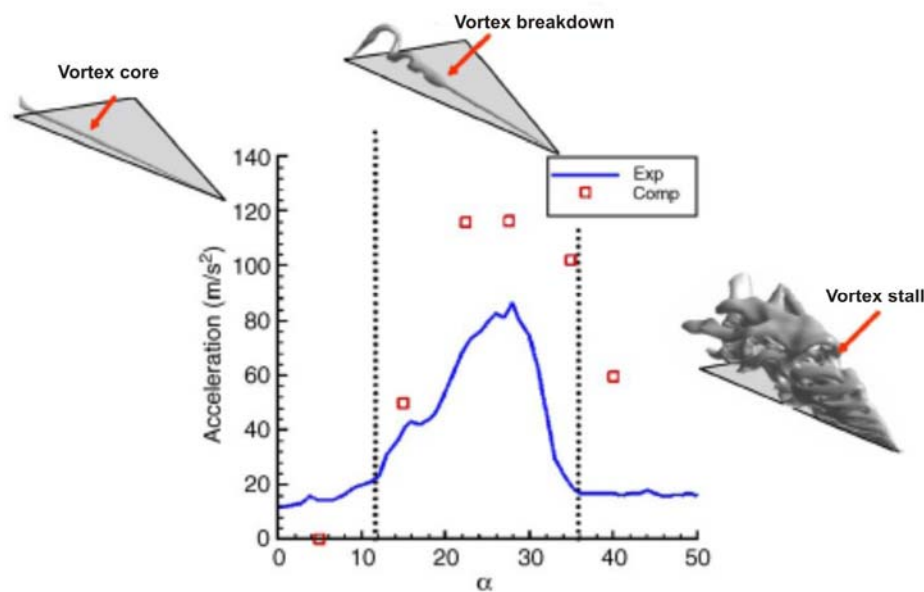
Figure 2.4. Variation of wing tip rms acceleration as a function of angle of attack for $\Lambda= 60^{o}$ sweep half delta wing model (Gursul et al., 2005).

Breitsamter, (2008) presented selected results from extensive experimental investigations on turbulent flow fields and unsteady surface pressures caused by leading-edge vortices, in particular, for vortex breakdown flow. Such turbulent flows may cause severe dynamic aero-elastic problems like wing and/or fin buffeting on fighter-type aircraft. The wind tunnel models were included a generic delta wing as

well as a detailed aircraft configuration of canard-delta wing type. Breitsamter, (2008) has stated that the turbulent flow structures were analyzed by root-mean-square and spectral distributions of velocity and pressure fluctuations as shown in Figure 2.5. Downstream of bursting local maxima of velocity fluctuations occur in a limited radial range around the vortex center. The corresponding spectra exhibit significant peaks indicating that turbulent kinetic energy was channeled into a narrow band. These quasi-periodic velocity oscillations arise from helical mode instability of the breakdown flow. Due to vortex bursting there was a characteristic increase in surface pressure fluctuations with increasing angle of attack, especially when the burst location moved closer to the apex. The pressure fluctuations also showed dominant frequencies corresponding to those of the velocity fluctuations. Using the measured flow field data, scaling parameters were derived for design purposes. It is shown that a frequency parameter based on the local semi-span and the sinus of angle of attack could be used to estimate the frequencies of dynamic loads evoked by vortex bursting.
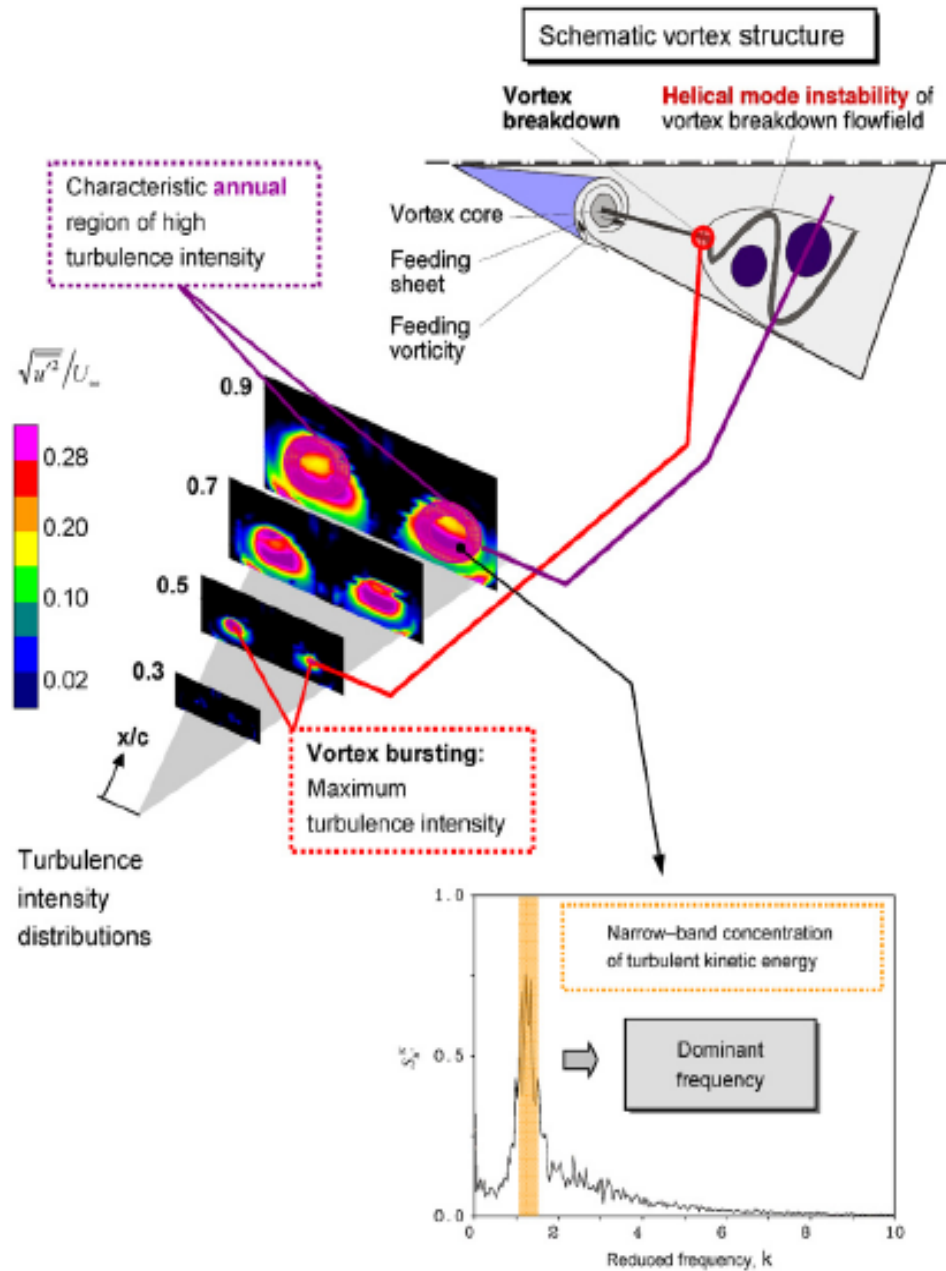
Figure 2.5. Characteristic of delta wing turbulence intensity distributions and power spectral densities for the leading-edge vortex breakdown flow field; $\Lambda=76^{\circ}$, $Re_C = 1.07 \times 10^6$ (Breitsamter, 2008).

Khan et. al. (2006) reported that a rigorous calculation of the turbulent kinetic energy TKE, requires knowledge of all three rms-velocity components as in

$k = \dfrac{1}{2}(\overline{u'^2} + \overline{v'^2} + \overline{w'^2})$. Use of the angle-resolved rms velocities avoids broadening of the turbulence kinetic energy due to the periodicity of this flow. With 2-D PIV data, there is no knowledge of the third rms velocity component (usually tangential) and k can only be estimated using a pseudo-isotropic assumption: $k = 0.75(\overline{u'^2} + \overline{v'^2})$. Here it was possible to check out the validity of this assumption, using both 2-D and 3-D PIV measurements.

2.3. Control of Flow Structure over Delta Wing

Efforts to control the structure and trajectory of leading-edge vortices formed from leading-edge extensions, as well as actual leading-edges of wings, have involved passive techniques, in the form of geometrical modifications at or upstream of the leading-edge and placement of a small wire within the leading-edge vortex; and active (open loop) approaches, which include blowing at the leading-edges of the wing and perturbations of the wing at very small amplitudes and high frequencies, in order to simulate leading-edge actuators. These approaches were briefly described by Yanıktepe, (2006).

Gursul et. al. (2007) reviewed vortex control concepts employed for slender and nonslender wings. Important aspects of flow control include flow separation, vortex formation, flow reattachment, vortex breakdown, and vortex instabilities. The occurrence and relative importance of these phenomena strongly depend on the wing sweep angle. They discussed various flow control methods: multiple vortices, control surfaces, blowing and suction, low-frequency and high-frequency excitations, feedback control, passive control with wing flexibility and plasma actuators. For slender delta wings, control of vortex breakdown was achieved by modifications to swirl level and external pressure gradient acting on the vortex core. Effects of flow control methods on these two parameters were discussed and their effectiveness was compared whenever possible. With the high-frequency excitation of the separated shear layer, reattachment and lift enhancement in the post stall region was observed which was orders of magnitude more effective than steady blowing. This effect was more pronounced for nonslender wings. Reformation of vortices was possible with

sufficient amplitude of forcing at the optimum frequency. Passive lift enhancement on flexible wings is due to the self-excited wing vibrations, which occur when the frequency of wing vibrations is close to the frequency of the shear layer instabilities and promote flow reattachment.

2.3.1. Active Control

Cui et. al. (2007) proposed a control method which was referred to as freebody slot blowing that exploited the benefits of both the spanwise slot blowing and the effectiveness of canards. Flow visualizations showed that this technique could be used to delay vortex breakdown on a delta wing more effectively than some existing blowing techniques. However, due to the constraints of the experimental setup, the study did not resolve the issue of why a single sided blowing delayed the formation of vortex breakdown on the blowing side but has an opposite effect on the non-blowing side. Figure 2.6a. shows the time-averaged flow images for double-sided blowing for AOA (angle of attack) = 20 deg and U=15.5 cm/s (Re = 4.5 x 10^4). It can be seen that with no blowing, the mean vortex breakdown location occurred at about 0.54 c (close to the second line from the trailing edge), and there was a slight asymmetry between the two breakdown locations. However, when a small blowing momentum of Cm = 0.084 was applied, there was a noticeable delay in the breakdown locations (Fig. 2.6b), and further increases in the blowing momentum led to additional delays in the breakdown location, as can be seen in Figs. 2.6c and 2.6d.
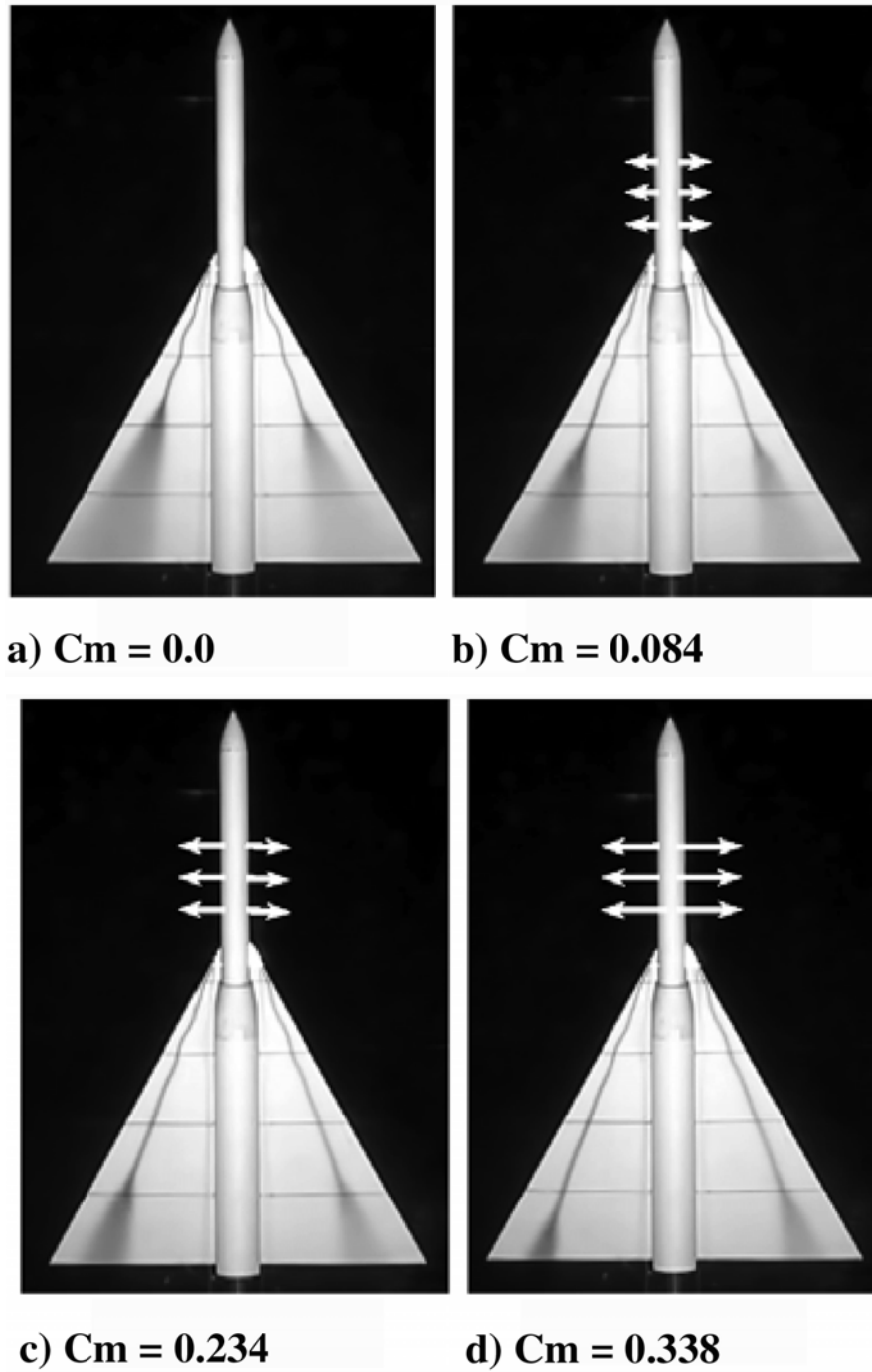
Figure 2.6. The images of vortex breakdown structures for different blowing momentum coefficients for double-sided blowing (SL = 40 mm and W =0.5 mm) at AOA = 20 deg and Re = 4.5 x 10^4. Arrows indicate the direction of forebody slot blowing (Cui et al., 2007).

Figure 2.7. shows the time-averaged results at AOA = 20 deg and Re = 6.8 x 10^4 for the three different arrangements, namely, a basic configuration, a basic configuration with canards, and a basic configuration with forebody slot blowing. It could be seen that both the canards and the slot blowing (Cm = 0.2) configurations were able to delay vortex breakdown locations (see Figs. 2.7b and 2.7c), but the trailing vortices from the canards appeared to have trajectories slightly closer to the centerline of the body.

a)   b)   c)
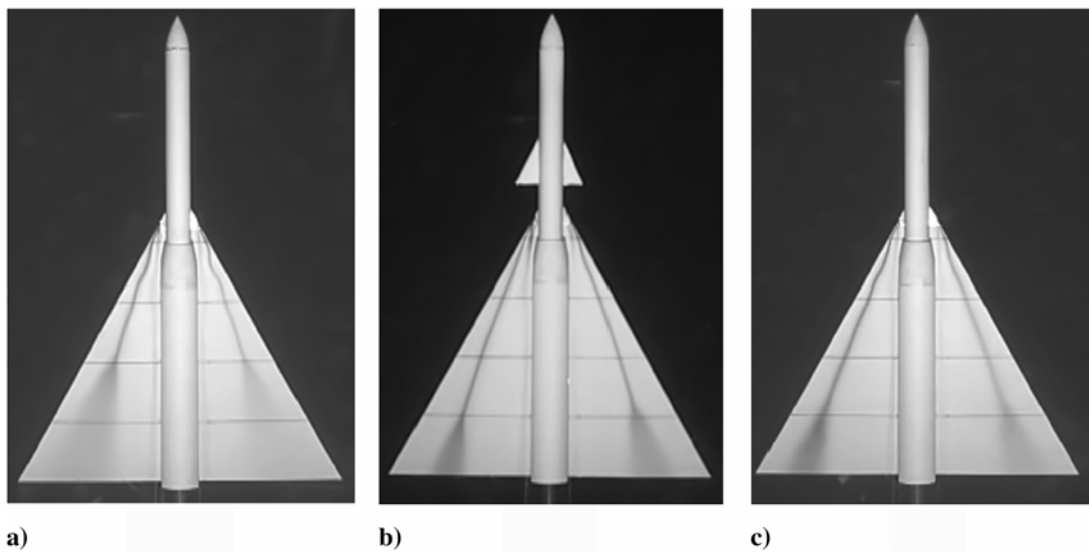
Figure 2.7. Effects of canards and double-sided forebody slot blowing on the vortex breakdown location at AOA = 20 deg and Re = 6.8 x 10^4 for a) basic configuration, b) basic configuration with canards, and c) basic configuration with double-sided slot blowing at Cm = 0.2 (Cui et al., 2007).

Yavuz and Rockwell (2006) observed the near-surface patterns on a delta wing at low sweep angle have been investigated as a function of both angle of attack and magnitude of localized blowing from slots at the trailing edge. A technique of high-image-density particle image velocimetry is employed to determine the topological critical points adjacent to the surface and in the near wake of the wing, in relation to the dimensionless magnitude of the blowing coefficient. The inside of the delta wing was machined in the form of a cavity, in order to allow generation of

23

uniform blowing from the trailing edge; this blowing is represented in the schematic of Figure 2.8.
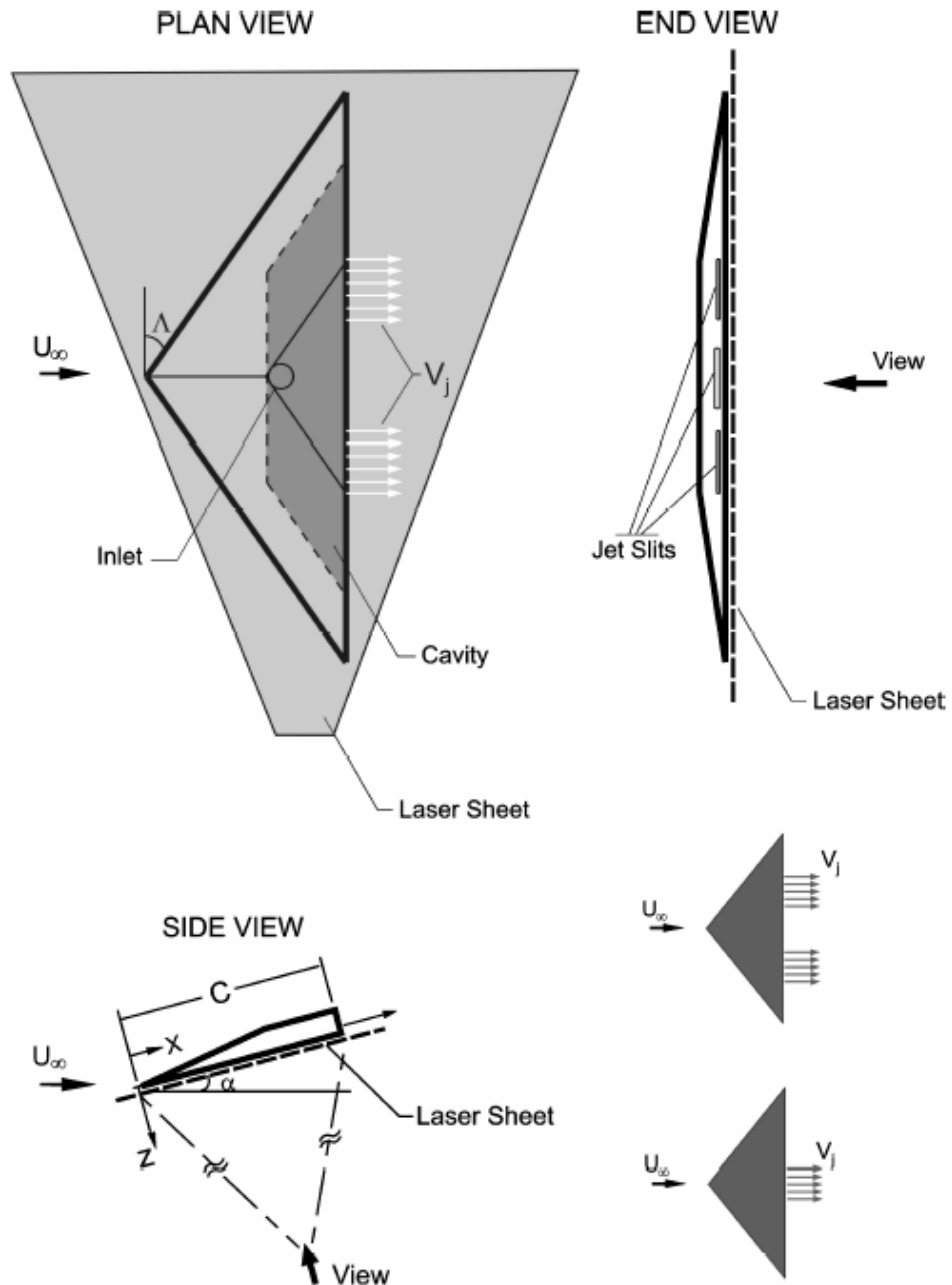
Figure 2.8. Overview of experimental setup including delta wing and laser sheet orientation (Yavuz and Rockwell, 2006).

Control of the leading-edge vortex breakdown location over a delta wing was accomplished by utilizing both symmetric and asymmetric trailing edge injection. Trailing edge injection demonstrated the capability to manipulate the vortex breakdown locations over a delta wing. The control is possible although its effectiveness is highly dependent on the trailing edge jet velocity ratios used as well as the configuration and orientation of the jets (Mitchell et al., 1999).

In the work of Renac et. al. (2005) an attempt was made for fluidic control of the vortical flow and its related vortex breakdown phenomenon over a delta wing with a particular geometry. Their the model had a sweep angle of $\Lambda=60$ deg and a rounded leading edge. The control system was based on four rectangular slots along the portside leading edge, and it provided continuous or pulsed jets normal to the leading-edge surface and parallel to the leeward side plane. The mass flow rate and the frequency of injection could be varied independently. They compared to a reference case defined by a microflap fixed along the leading edge and set perpendicular to it. Qualitative measurements were obtained with surface flow visualizations and boundary-layer transition detections with acenaphthene. Quantitative data consist in mean and instantaneous surface pressure distributions measurements under the primary vortex axis and in mean three-dimensional velocity held measurements.

Akilli et al. (2001) have investigated the sensitivity of vortex breakdown. They have studied that a small wire oriented orthogonally to the axis of the leading-edge vortex on a delta wing at high angle-of-attack generates substantial changes in the vortex structure, which is characterized using a technique of high-image-density particle image velocimetry. They have used a wire having a diameter two orders of magnitude smaller than the diameter of the leading-edge vortex prior to the onset of vortex breakdown. They concluded that a wire can substantially advance the onset of breakdown by as much as fifteen vortex diameters. They have found that depending upon the dimensionless diameter of the wire and wire location along the axis of the vortex, the onset of vortex breakdown can occur either upstream or downstream of the wire. They also showed that contours of constant velocity indicating the rate of decrease of streamwise velocity along the centerline of the vortex is substantially

enhanced, even for locations well upstream of the wire, relative to the case of vortex breakdown in absence of a wire. They also conclude that patterns of instantaneous vorticity in presence of the wire typically exhibit a form characteristic of either a spiral- or bubble-like mode of breakdown that occurs in absence of the wire. It is possible to classify the pressure fluctuations on the surface of the delta wing in terms of dimensionless frequencies which, in turn, represent various features of the flow unsteadiness, including the onset of vortex breakdown.

Goruney and Rockwell, (2009) characterized the near-surface flow patterns for delta wings having sinusoidally shaped leading edges of various values of amplitude and wavelength. The nominal value of (low) sweep angle was kept constant, and the wing was oriented at a high value of angle of attack. At high angle of attack, where large-scale three-dimensional separation occurred from the wing with a straight leading edge, amplitude of the leading-edge protuberance as small as one-half of one percent of the chord of the wing could substantially alter the near-surface topology. When the amplitude reached a value of four percent of the chord, it was possible to completely eradicate the negative focus of large-scale, three-dimensional separation, in favor of a positive focus of attachment. Moreover, alteration of the near-surface topology was most effective when the ratio of the wavelength to amplitude of the sinusoidal leading edge was maintained at a small value. Figure 2.9. shows generic categories of topological patterns involving negative and positive bifurcation lines, saddles of attachment and separation and stable and unstable foci and nodes.
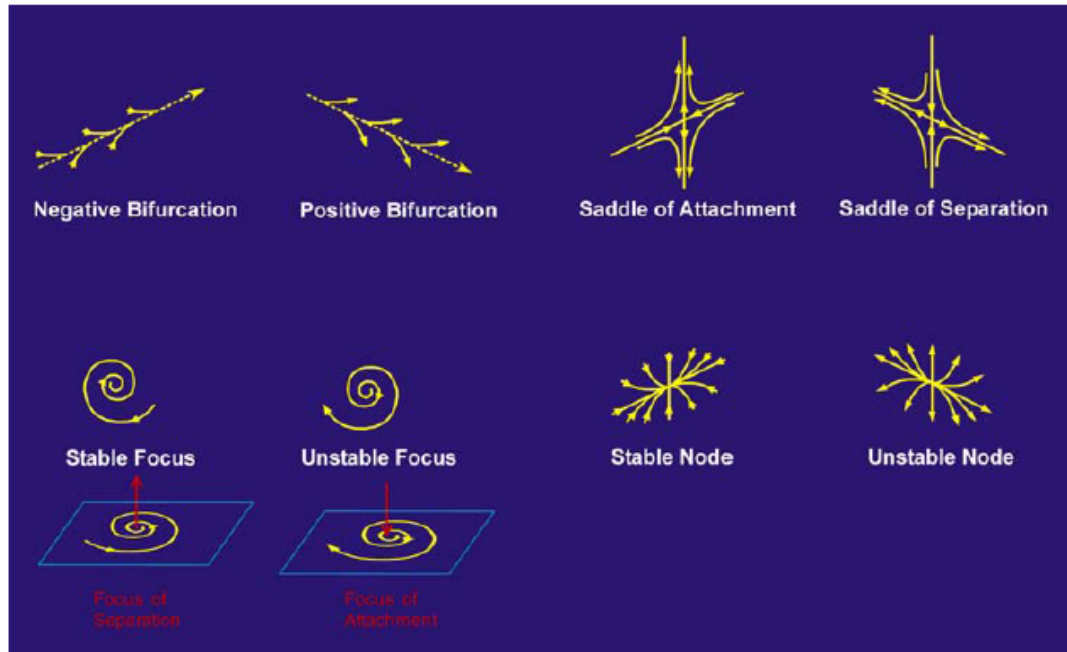
Figure 2.9. Overview of basic classes of critical points of flow topology (Goruney and Rockwell, 2009).

Another study of Akilli et al., (2003) recorded that a very small diameter wire was tethered from the apex of a delta wing and nominally aligned with the centerline of the leading-edge vortex. An overview of the delta wing arrangement with a deployed wire is shown in Figure 2.10. (Akilli et al., 2003). The wire could alter both the onset and structure of vortex breakdown. A technique of high-image-density particle image velocimetry allowed acquisition of patterns of instantaneous and averaged vorticity and velocity, which revealed the relationship between: Advancement of vortex breakdown towards the apex of the wing; and corresponding changes of patterns of vorticity and velocity contours. The diameter of the wire was one percent of the core diameter of the pre-breakdown vortex. It was possible to alter the onset of vortex breakdown by as much as approximately one chord length of the wing.
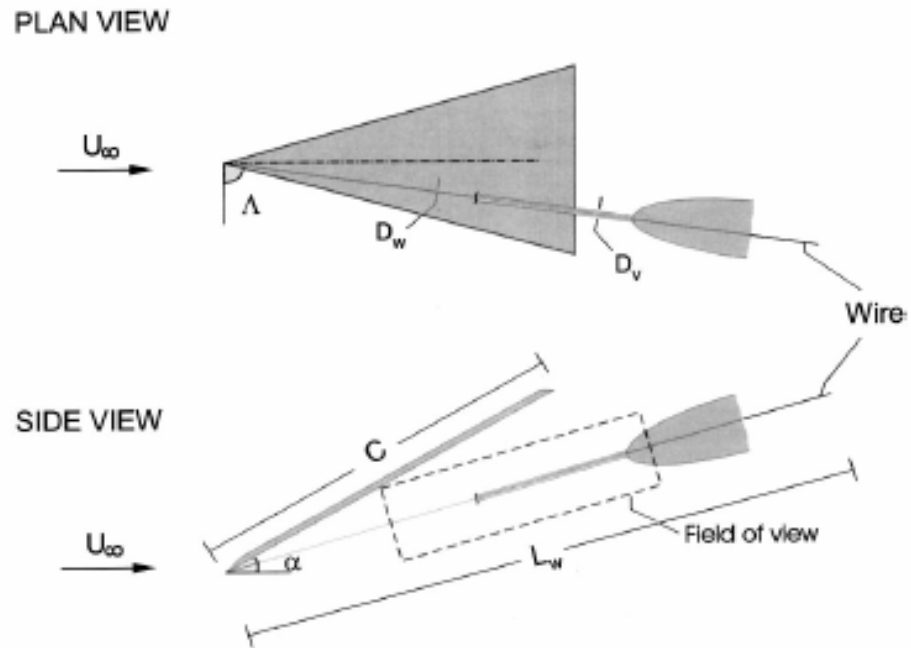
Figure 2.10. Overview of delta wing showing concept of small wire of diameter D_w
and length L_w aligned with axis of the leading-edge vortex having a
pre-breakdown diameter of D_v . Leading end of wire is tethered from
tip of apex of wing. Field of view of image corresponds to $0.7C$ (Akilli
et al., 2003).

Sahin et. al., (2001) employed high-image-density particle image velocimetry
to determine the instantaneous and averaged features of distortion of vortex
breakdown incident on a stationary and an oscillating leading edge. It was
demonstrated that the onset of vortex breakdown could be advanced or retarded
substantially, depending on the period of the edge oscillation relative to the inherent
frequency of vortex breakdown. Matsuno and Nakamura (2000) presented an
experimental study on unsteady aerodynamics of 45° delta wings in rolling motion.
Self-induced oscillations could be observed for these wings with rounded leading
edges at high angles of attack, which have different features from that of wing rock.
As a result, it was found that nonlinear characteristics of the leading-edge vortices
had a strong effect on the wing motion. The flow visualization confirmed that this
oscillation was attributed to asymmetry of the leading-edge vortices. Mochizuki et al.
(2006) observed oscillation of the angle of attack of the wing induced a periodic

perturbation in the strength of the streamwise vortex. Analysis by triple velocity decomposition and phase averaging showed that the oscillation induced periodic variations in the strength, radius, and position of the streamwise vortex center. Generally speaking, the unsteadiness on a delta wing must also include contributions due to random displacements of the vortex core and fluctuations of the position of vortex breakdown, as shown respectively by Gursul and Yang (1995). Deng and Gursul (1997) presented flow visualization and LDV measurements were carried out for a delta wing with oscillating leading-edge flaps. The effect of leading-edge flaps on leading-edge vortices and vortex breakdown was investigated. It was shown that the response of breakdown location strongly depended on the amplitude of the flap oscillations and angle of attack.

Ozgoren and Sahin, (2002) reported the variation of breakdown location hysteresis loops. The time-averaged breakdown location over one cycle may move upstream or downstream when compared to the quasi-steady case, depending on the amplitude of flap oscillations and angle of attack. Flow past the leading edge of a delta wing oscillating about its mid-cord in a pitch plane with a reduced frequency of K=0.74 generated primary vortices having mostly elongated shapes. Their shapes and orientations varied with the pitching angle of the delta wing in upstroke and down stroke directions. They stated that for the pitching delta wing, the development of the vortex core and degree of hysteresis were found to be a strong function of reduced frequency.

Ozgoren et al. (2001) characterized the effect of perturbations of the entire wing on the time-averaged features of the multiple shear layer structure of the leading-edge vortex, including the onset of vortex breakdown. They subjected a delta wing to very small amplitude oscillations in the pitching mode, but at a sufficiently high frequency such that the structure of the leading-vortex was substantially altered. These modified leading-edge vortices impinged upon a downstream plate, and the instantaneous and averaged features of the vortex-plate distortion showed that the buffet velocity field was considerably modified, relative to the case of a stationary wing without perturbations at, or of the leading-edge. They perturbed the wing sinusoidally over a tenfold range of reduced frequency in order to determine the

nature of the vortex development and breakdown. They found that the vortex core developed in the upstream direction towards the apex at low frequencies; on the other hand, there was ejection of the downstream direction at high frequencies. They defined reduced frequency as $K=\pi f_e C/U_{ref}$. This dimensionless frequency represented the ratio of the wing chord C to the wavelength U_{ref}/f_e of the forced motion. They examined the flow structure over the range of reduced frequency $0.025<K<1.94$ and mean angle-of-attack $5^o<\alpha_m<20^o$. Here, U_{ref} was the reference velocity; f_e was the frequency of the delta wing perturbation. It is known that delta wing in steady flow can provide high lift at large angles of attack and are therefore used on many high-performance aircrafts. The oscillation of a body in a flowing fluid creates a time-dependant, three dimensional flow fields which in turn give rise to the fluctuating pressure field on the surface of the body, involving most complex fluid/structure interactions (Deniz and Staubli, 1977). Coton et al. (2001) presented experiments to measure the upper-surface-pressure distribution on a pitching 60-deg delta wing with sharp leading edges were carried out. It was demonstrated that the high spatial and temporal resolution of the data was, via analysis of the unsteady pressures, facilitated identification of key features of the flow. In addition to allowing the forward progression of vortex breakdown with incidence to be tracked, it was possible to isolate dominant post breakdown buffet frequencies.

2.3.2. Passive Control

The new unmanned combat air vehicle (UCAV) configurations being developed will need to be highly maneuverable while allowing for increased flexibility in the wing structure. These vehicles often incorporate delta-type wing shapes of more moderate sweep (40°–60°). While extensive investigations of highly swept ($\Lambda>60°$); rigid delta wings have been made both experimentally and computationally, significantly less research was undertaken for these higher aspect ratio delta wing configurations. Furthermore, very few researchers were examined the interaction of the resulting unsteady vortical flow with a flexible delta wing. Further research was required to provide a better understanding of the aero elastic

response of a delta wing at angle of attack as expressed by Gordnier and Visbal, (2004).

In recent years aerodynamic of flexible wings has been searched and it has been shown that flexible wings affect the structure of vortical flow (Gordon ve Gürsul, 2004). Kawazoe and Kato (2006) were experimentally studied the aerodynamics forces and moments of flexible delta wing in pitching motion in a low-speed wind tunnel. Three types of flexible delta wing were investigated, the flexible parts of which were 44, 70 and 99 % of the delta wing. Aerodynamic characteristics were different among the three types of flexible and completely hard delta wing, and it was found that the winding-up of the leading edge of the delta wing was the key factor for determining the leading edge vortex on the upper side of the wing and pressure distribution on the windward side. Lift, drag, and pitching moment formed a hysteresis loop with an angle of attack in pitching motion, particularly in a region with a large attack angle, accompanied by leading edge vortex breakdown. The deformation appearance of the flexible delta wing, type C, in the airflow is shown in Figure. 2.11. compared with that of the stationary wing.

(a)

(b)
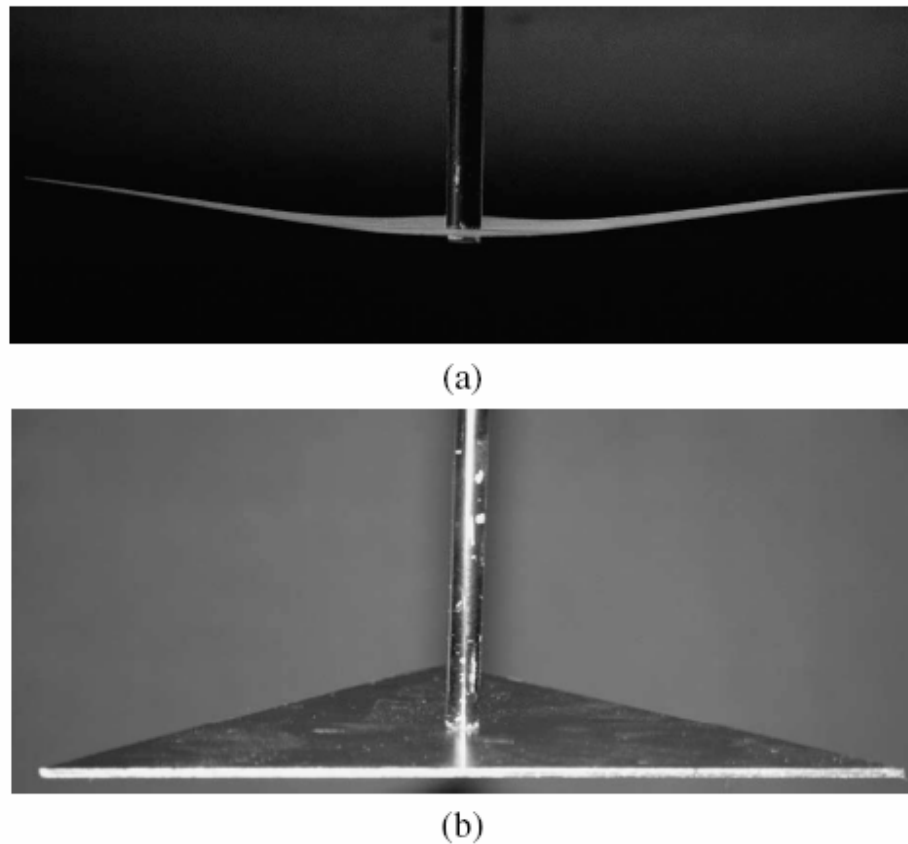
Figure 2.11. Deformation of C-type flexible delta wing compared with that of hard delta wing. a) C-type flexible delta wing and b) hard delta wing (Kawazoe and Kato, 2006).

Viieru et al. (2006) proposed the fixed wing research focus that was on the low Reynolds number aerodynamics, including the leading edge separation bubble and the thereafter incurred laminar to turbulence transition. As previously discussed, fixed wing can use flexible material as its lifting surface. One advantage for the flexible wing is that it could facilitate passive shape adaptation, which resulted in delayed stall. Waszak et al., (2001) was experimentally shown that under modest angles of attack, both rigid and membrane wings demonstrated similar lift characteristics with the stiffer wings having slightly higher lift coefficient. However, it was clear that the membrane wings stall at higher angles of attack than the rigid

wing. This aspect was a key element in enhancing the stability and agility of MAVs. For example, typical rigid wings had stall angles between 12 and 15 degrees, while the stall angles of the flexible wings were between 30 and 45 degrees (Waszak et al., 2001).

Passive lift enhancement for flexible delta wings was demonstrated as a potential method for the control of vortex-dominated wing flows (Taylor et al., 2003). Gursul et al. (2006) investigated force measurements over a range of nonslender delta wings (with sweep angles $\Lambda = 40°$ to $55°$) that demonstrated the ability of a flexible wing to enhance lift and delayed stall compared with a rigid wing of similar geometry. This recently discovered phenomenon appeared to be a feature of nonslender wings. Flow visualization, PIV and LDV measurements showed that flow reattachment takes place on the flexible wings in the post-stall region of the rigid wings. The lift increase in the post-stall region was accompanied with large self-excited vibrations of the wings.

Sohn et. al (2004) examined the vortical flow at sideslip of a delta wing with LEX through off-surface visualization of the wing leeward flow region. Angles of attack of $12°$, $16°$, $20°$, and $24°$ were tested at sideslip angles of $0°$, $−5°$, and $−10°$. The flow Reynolds number based on the main-wing chord was 1.82×10^5. The wing vortex and the LEX vortex coiled around each other while maintaining comparable strength and identity at a zero sideslip. The increase of angle of attack intensified the coiling and shifted the cores of the wing and LEX vortices inboard and upward. By sideslip, the coiling, the merging and, the diffusion of the wing and LEX vortices increased on the windward side, whereas they became delayed significantly on the leeward side. Also the migration behavior of vortices on the windward and leeward sides of the wing changed considerably. The present study confirms that the sideslip angle has a profound effect on the vortex structure and interaction of a delta wing with LEX, which characterized the vortex-induced aerodynamic load. It is worth to mentioned that there is only this article which reports the effect of yaw angle of the delta wing on the vortical flow structure. Figure 2.12 shows the experimental model in the test section of the wind tunnel.

Figure 2.12. Experimental model (Sohn et. al., 2004).

Wang and Xu (2004) presented the effect of the apex flap on the aerodynamic performance of the delta wing for a 30%*c* apex flap. When the flap was deflected downward, the effective angle of attack decreased for the entire delta wing; thus lift increased at high angles of attack. Delta wing model with apex flaps is shown in Figure 2.13.
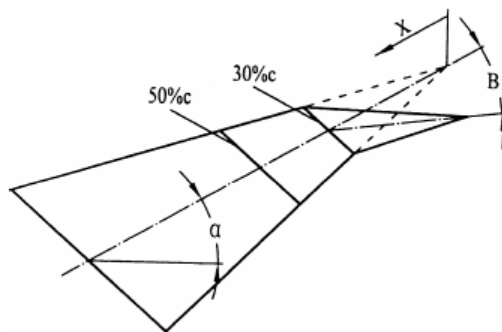
Figure 2.13. Delta wing model with apex flaps (Wang and Xu, 2004).

In the results of the investigation of Moul et al. (1995), the three arrow wings experienced a pitch-up that became more severe as aspect ratio were increased. This pitch-up could be reduced by deflecting the leading-edge flaps. When deflected symmetrically, the trailing-edge flaps produced relatively small pitching moments on all the wings. These pitch-control increments were more linear with deflection angle in the nose-up direction than in the nose-down direction. Also, the nose-down control effectiveness was less than the nose-up effectiveness at the higher angles of attack. Although all the configurations would require small changes in longitudinal stability, each of them could be statically trimmed at angles of attack up to maximum lift by using the inboard and middle flaps together (Moul et al. 1995). However, additional control power might be needed to provide a control margin for dynamic situations such as maneuvering or countering turbulence. Another limit on the trim capability of these wings might be imposed by the need to budget the amount of flap deflection available for each type of control (pitch, roll, or yaw). The combination of pitch-up and reduced nose-down control effectiveness resulted in a hung stall (trim condition at which there was insufficient nose-down control for recovery) for some of the configurations. As seen in Figure 2.14 from a geometric point of view, the arrow planforms could be considered to be built up from the diamond planform by the addition of outboard panels having the same sweep angles as the diamond planform (Moul et al. 1995).
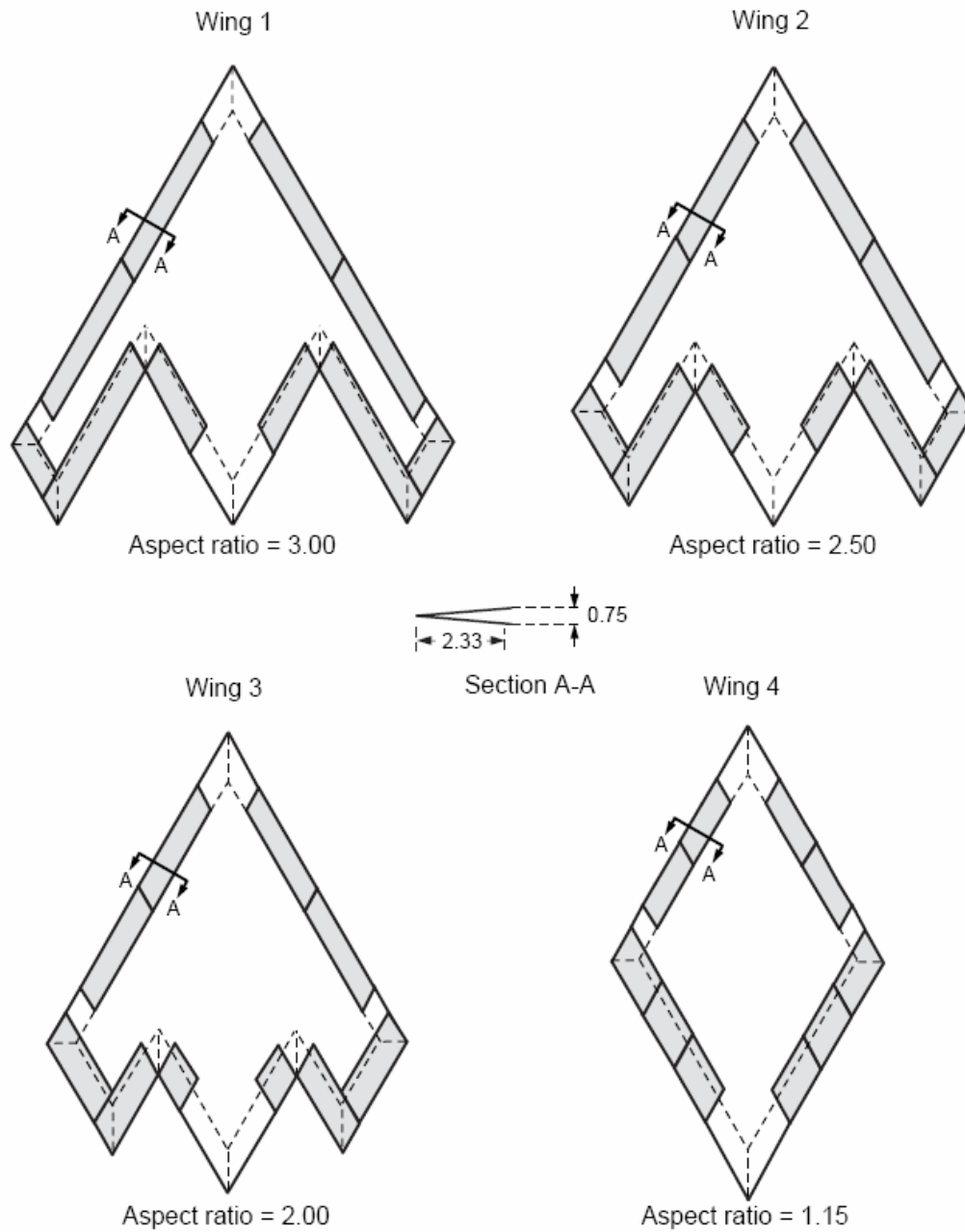
Figure 2.14. Wing planforms. Control surfaces (shaded areas) and bevel lines (dashed lines) (Moul et. al., 1995).

3. MATERIAL AND METHODS

3.1. Channel System

Experiments were conducted in a large scale and circulating free-surface water channel. The internal dimensions of the water channel were of $8000 \, mm \times 1000 \, mm \times 750 \, mm$ which was made from $15 \, mm$ thick transparent plexiglass sheet with upstream and downstream fiberglass reservoirs. Before reaching the test chamber, the water was pumped into a settling chamber and passed through a honeycomb section and a 2:1 channel contraction. These reservoirs and honeycomb screen arrangements were used to maintain the turbulence intensity below 0.1 %.

3.2. Experimental Apparatus

In the present study, the delta wing was kept stable in water by using servo motor. A special aperture was designed for servo motor and attack angles of the delta wing was adjusted by using specially designed mechanism which was connected to the servo motor. Servo system unit contained one servo motor, servo motor driver and control unit as shown in Figure 1. A brief fundamental description of the servo system can be explained as follows:

A servo motor has an output shaft which can be positioned to specific angular positions by sending the servo a coded signal. As long as the coded signal exists on the input line, the servo will maintain the angular position of the shaft. As the coded signal changes, the angular position of the shaft changes. The desired position of motor shaft can be provided by a control unit by sending suitable signals. Servo motor's shaft can be rotated by 180^{0}.

The wing was maintained in a nominally horizontal position by a slender support strut that extended vertically from the midchord of the wing. This strut has a width of 4 mm and a streamwise length of 35 mm. Assessment of this type of strut arrangement involved comparison with complementary experiments involving a nominally horizontal sting and comparison of the location of vortex breakdown for

wings of different attack and yaw angles. As a consequence, this strut arrangement has an insignificant effect on the flow structure on the leeward side of the wing.

Figure 3.1. Servo Motor and its control Unit

3.3. Dye and Particle Image Velocimetry (PIV) Experiments

3.3.1. Dye Visualization Experiments

A fluorescent dye which shines under laser sheet was used to create color change in water to visualize flow characteristics over the delta wing during the dye experiments. Dye was located in a small container which is located 500 mm above the free surface of the water channel. Dye was injected near field of the delta wing trailing edge by plastic pipe and dye was passed through a narrow and close channel in the delta wing to its apex. The video camera which was SONY HD-SR1 was used to capture the instantaneous video images of the vortex flow structures. The images were captured by frame grabber software of camera. The dye visualization technique gives no numerical information about flow structure of vortical flow, but demonstrates a brief and rough idea about flow structure over the delta wing.
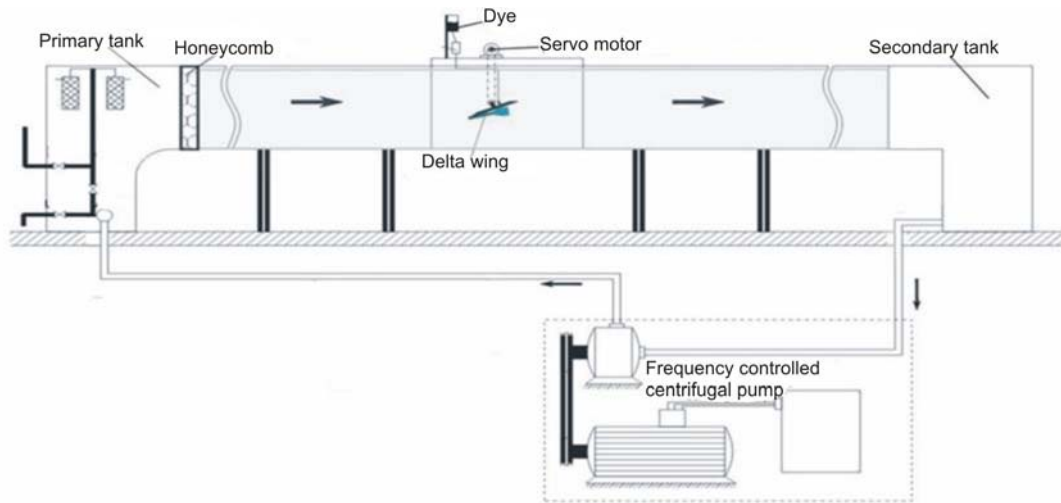
Figure 3.2. Schematics of channel and its mechanism

3.3.2. Particle Image Velocimetry (PIV)

Particle Image Velocimetry (PIV) is a measurement technique to determine the velocities at many points in a fluid flow field simultaneously. The technique involves seeding the flow field, illuminating the region under investigation and capturing two images of that region in rapid succession. From the displacement of the tracer particles, provided that the time interval between image captures is known, a velocity vector map can be calculated in the flow field.

3.3.2.1. Principles of PIV

The general principle of PIV is to illuminate tracer particles in the flow field of interest with a plane sheet of light, and acquire two images of the flow field with a known time separation. When a digital CCD camera is used for image acquisition, one uses the acronym DPIV. The displacement field is determined from the motion of the tracer particles between the two images, and by dividing this with the known time separation one obtains the velocity field. The problem in PIV is to determine the displacement field. The time separation is assumed to be known with sufficient

accuracy. The technique of PIV can be considered as consisting of two stages; image acquisition and image evaluation (Figure 3.3).
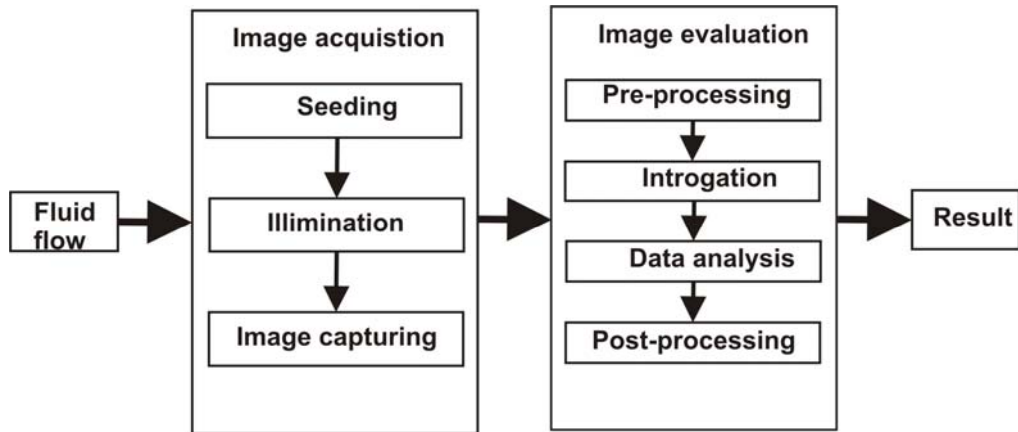
Figure 3.3. General PIV process

3.3.2.2. Image Acquisition

Figure 3.4 shows a typical experimental arrangement for carrying out PIV measurements. Tracer particles added to the flow under investigation are illuminated by laser sheet and images of the illuminated flow field are captured and stored for later analysis.
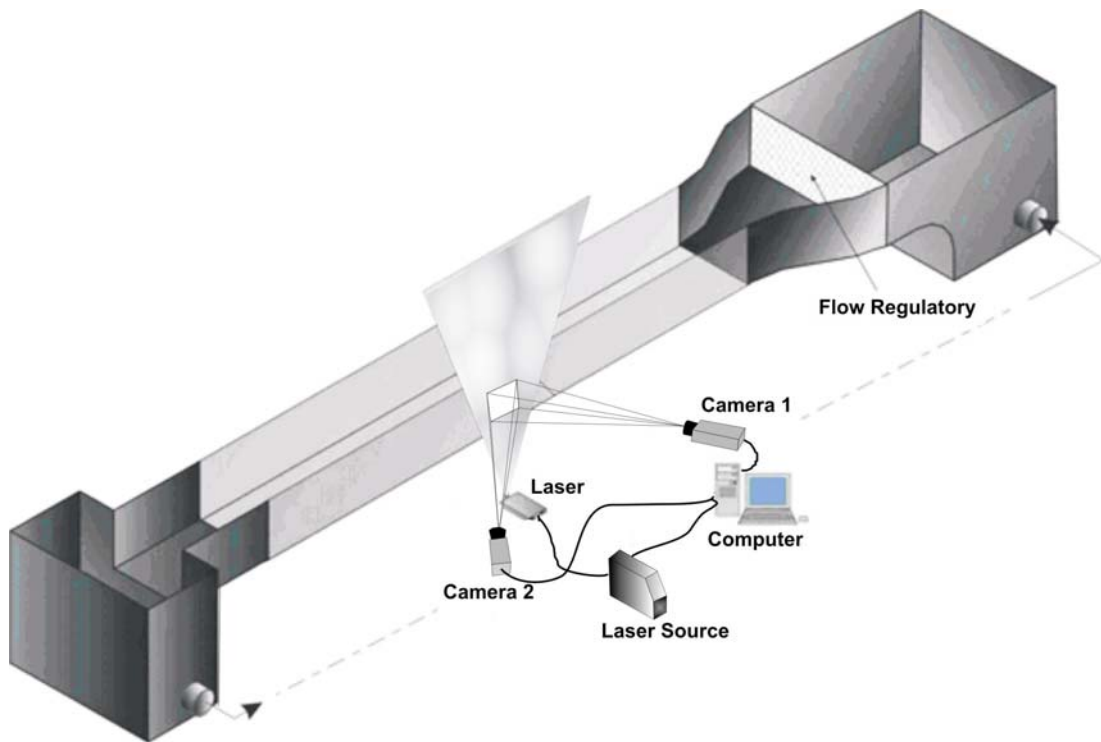
Figure 3.4. PIV equipages of measurement system

3.3.2.3. Seeding

Particle size and density, and fluid density and viscosity, determine the effects of buoyancy and inertia. Exact neutral buoyancy is difficult to achieve, but particles must remain suspended throughout an experiment.

In general, seeding is easier in fluids. Lower velocities and accelerations combined with the higher density and viscosity of liquid means larger, more easily detectable images. In fluids, they may be up to tens of microns in diameter; in air diameters range from 5 microns to sub micron.

The light scattered from the particles is only a fractions of the light introduced into the flow. Of this scattered light, only that within the solid angle defined by the lens aperture of the imaging system will be collected to form an image. Conventional PIV set-ups record side-scattered light, which can be orders of magnitude weaker than forward-scattered light. The size and material of the seed particles can affect scattering efficiency and small particles also affect particle image intensity. The

average particle image should exceed the fog level of photographic emulsions or the noise level of solid-state detectors.

Seeding is, in general, easier in water than in air. Lower velocity and accelerations combined with the higher density and viscosity of liquid mean larger, more easily detectable particles can be used.

3.3.2.4. Illumination

In PIV, the displacement field is determined as average displacements within so-called interrogation areas of the image plane. A typical size of these interrogation areas is 32x32 pixels, which means that one gets about 7227 vectors from an image with a resolution of 1600 x 1186 pixels. For single exposed images, the displacement is determined by forming the cross-correlation of corresponding interrogation areas in the first and second images. The location of the highest correlation peak in the correlation plane corresponds to the most likely average particle displacement in the interrogation area. Sub-pixel accuracy of the displacement is obtained by fitting a Gaussian distribution to the correlation peak, and finding the exact peak location. Since the cross-correlation method uses all information within the interrogation area for finding the displacement, the method is robust and often provides reasonable results even for non-ideal conditions. Another advantage is that the displacement field is obtained on a regular grid.

For the illumination, it is preferable to use a laser, since the laser beam is easy to form into a sheet by a cylindrical lens. A pulsed laser is preferred, since one obtains a high light energy during a very short time interval (typically 5 ns for a YAG-laser), which means that the particle images will be practically frozen even for high velocities (> 100 m/s). The repetition rate of a YAG-laser is typically 15 Hz, which is too low except for very low velocities (< 1 cm/s). One therefore needs two lasers to get full freedom in terms of time separation between the pulses. Special PIV YAG-lasers are available that combine two laser cavities with a common beam outlet (Dantec Dynamics user manual, 2005).

3.3.2.5. Image Capturing

Three-dimensional PIV is based on the same fundamental principle as human eyesight: stereoscopic vision. Our eyes see slightly different images. Comparing these images, the brain derives a 3-dimensional interpretation. Using just one eye, you can recognize motion up, down or sideways but will have difficulty judging distances and motion towards or away from you. As with 2D measurements, stereo PIV measures displacements rather than actual velocities, with the cameras playing the role of "eyes". The larger the angle between the two cameras, the more accurate the determination of the out-of-plane displacement if optical access is restricted, smaller angles can be used, but at the cost of accuracy in determining the third velocity component.

The actual stereo measurements begin with conventional 2D-PIV processing of simultaneous recordings from the two cameras. This produces two 2-dimensional vector maps showing the instantaneous flow field as seen from each of the cameras. Using the calibration function with the parameters obtained during camera set-up, the points in the chosen interrogation grid are now mapped from the light sheet plane and onto the left and right image planes (CCD-chip). With a 2D displacement seen from both left and right camera estimated at the same point in physical space, the true 3D particle displacement can be calculated by solving the equations obtained in the calibration.

3.3.2.6. 3D PIV Calibration Features

3D stereo PIV measurements are based on the same fundamental principles as human eye-sight; i.e. stereo vision. "When we look at a given object, our left and right eyes see two similar but not identical images. The brain compares the two images and interprets the slight variations to re-build the 3-dimensional information of the object observed." Similarly, Stereo-PIV system measures particles displacements using two CCD/CMOS Cameras:

- Each camera plays the role of the human eye, looking at the flowfield from different angles.

- The software plays the role of the brain, relating the observed (2x2D) displacements to 3D displacements (Dantec Dynamics Software Manual).
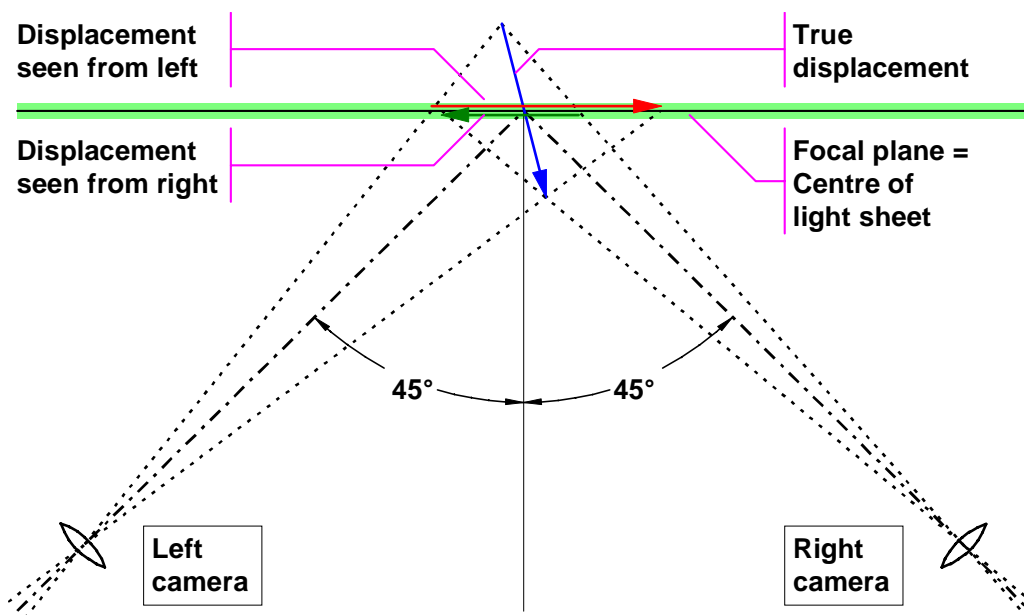
Figure 3.5. Principle of stereo-vision.

Mathematically, the most accurate determination of particles displacements (and thereby velocities) is obtained when the angle between the two cameras is set to 90°. In the case of a restricted optical access, stereoscopic imaging at smaller angles has been demonstrated at the cost of a somewhat reduced accuracy. Further, experience indicates that excellent 3D stereo PIV measurements can also be performed with camera viewing angles of $\pm 30^{0}$.

In practice, the two camera views are calibrated by recording images of a calibration target and fitting an imaging model on the top of the records. This

calibration target contains markers with well-defined (X, Y, Z)-positions/coordinates and the model parameters are calculated by comparing the positions of these markers on each camera images(Dantec Dynamics Software Manual).
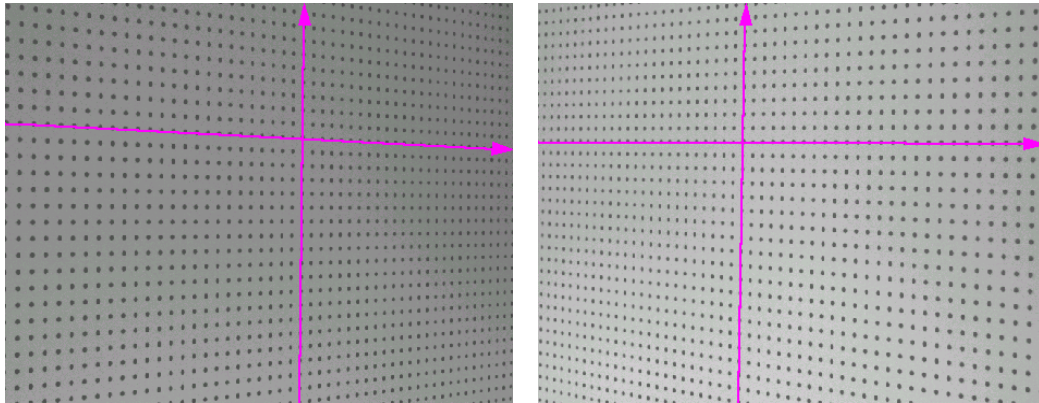
Figure 3.6. Example of calibration images recorded from camera 1 and camera 2.

Stereo-measurements start with conventional 2D PIV processing of PIV images recorded (simultaneously) with the two cameras. This produces two 2D vector maps representing the instantaneous flowfield as seen from the cameras. Using the camera view calibrations calculated earlier, these two 2D vector maps are then combined into one single 3D vector map. Due to perspective distortion, each camera covers a trapezoidal region of the light sheet. This means only partial overlap (see Figure 3.7) is obtained when recombine the camera views for 3D-PIV data calculations. 3D measuring system eliminates the error (1-2%) that is occurred in 2D system. In 2D measuring system, two dimensional projections of the displacements of laser lightened particles are measured. In reality these displacements are in 3 dimensional plane. This problem brings out an error factor on measurements since velocity compound in 3rd dimension cant be taken into measurements in 2D PIV system (Prasad ve Adrian, 1995).
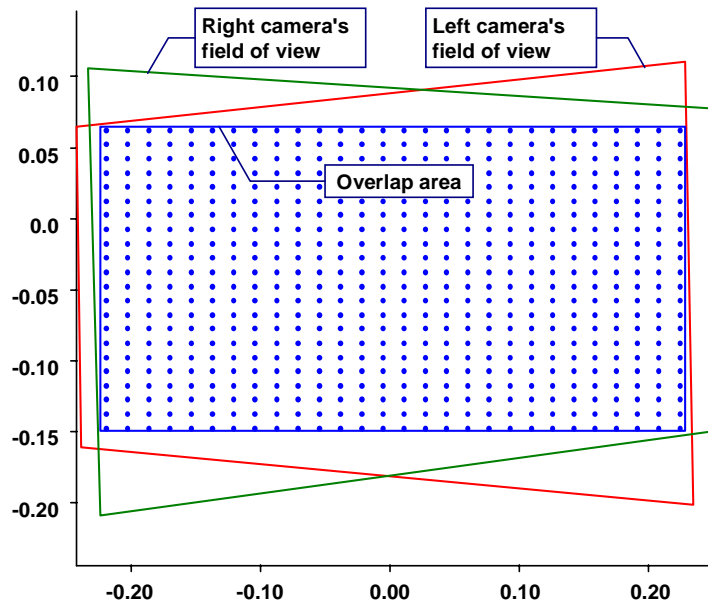
Figure 3.7. Overlapping fields of view.

Within this region of overlap, interrogation points are chosen in a rectangular grid. In principle 3D calculations can be performed on an infinitely dense grid. In practice, however, the 2D results have limited spatial resolution, and using a very dense grid for 3D evaluation will not improve the fundamental spatial resolution of the technique. Beside, this will considerably reduce the accuracy of particle displacement identification and thereby raw 2D-velocity determination (Dantec Dynamics Software Manual).
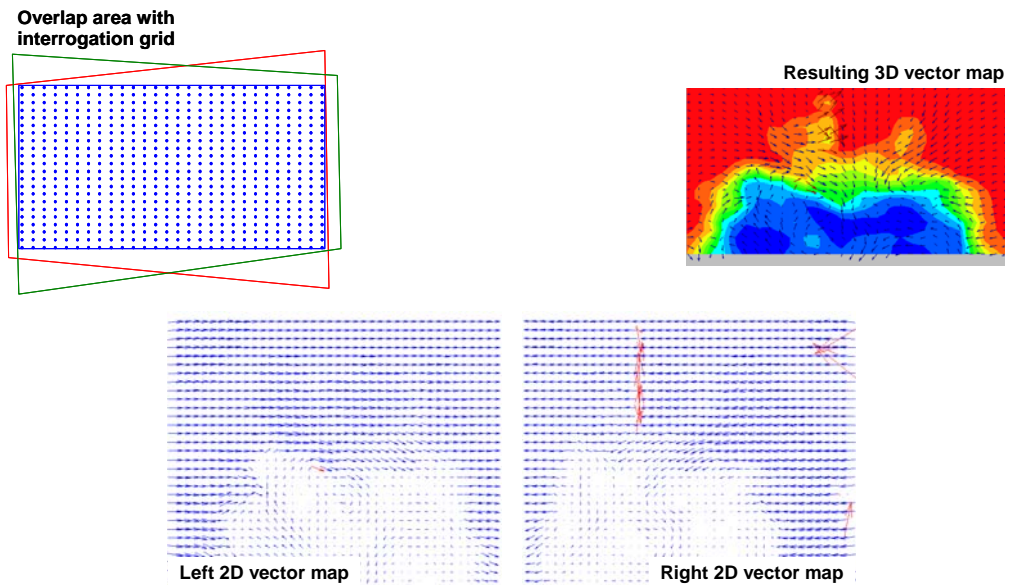
Figure 3.8. 3D PIV data reconstruction.

To enforce the Scheimpflug condition (which requires that the object plane, the lens plane and the image plane are collinear) a special camera mount is required. In principle, the two cameras point at the calibration target at an optional angle. Both have one CCD/CMOS tilt axis and in this plane the Scheimpflug condition is satisfied and the cameras are tilted according to the object-plane or calibration target (Figure 3.9).
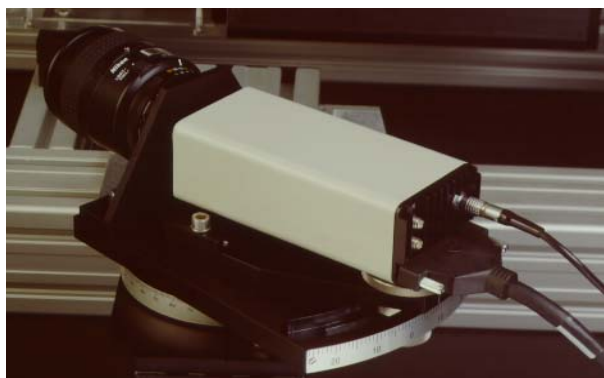
Figure 3.9. Scheimpflug condition camera plane.

The calibration uses a well defined grid of dots usually mounted on a traverse system (see Figure 3.10) (Dantec Dynamics Software Manual). The calibration target is aligned with the light sheet and normally traversed through the light sheet in several positions. The dots on the calibration target are used to calculate linear or higher order calibration equations for each camera. The linear calibration compensates for differences in scale and lack of orthogonally while higher order calibration equations compensate for non-linear distortions like radial and barrel distortion. It is shown that this calibration scheme provides highly accurate mapping functions with final displacement errors smaller than is expected from the other error sources, like the basic particle image velocimetry (PIV) correlation algorithm for real images (Wieneke, 2005). For a more extensive description of the principles of SPIV we refer to Turney et al. (*2009*), van Doorne and Westerweel (2007), Soloff et al. (*1997*) and Willert (*1997*).
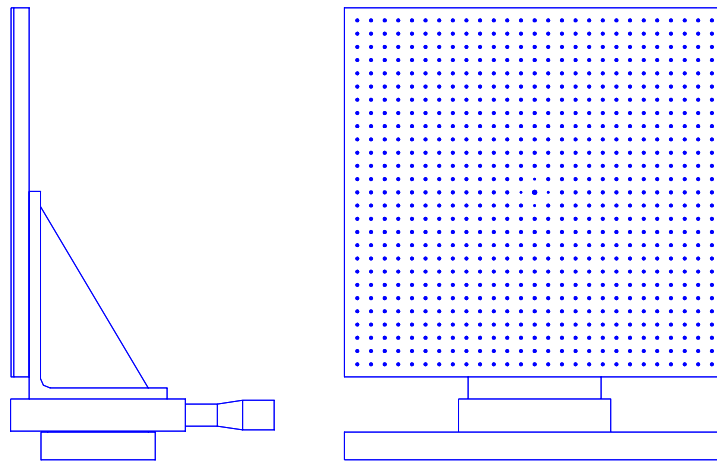
Figure 3.10. Standard calibration target mounted on traverse.

3.4. Experimental Setup

The dimensions and measurement planes on the diamond and lambda wing models are shown in Figures 3.11 and 3.12. These figures show the system

coordinates and critical length scales for diamond and lambda wings. The fore region of the wings was matched. That is, the delta wing portion of the leading region of each wing, having a chord $C' = 101$ mm, was maintained the same for each planform, in order to allow a direct comparison of the consequence of trailing-edge configuration on the flow development. The chord C of the diamond and lambda wings had value of 168 mm. The sweep angle of each wing was specified as $\Lambda = 40°$. In addition, the wing had a thickness t of 3 mm, and was beveled on the windward side at an angle of 45°. The value of Reynolds number based on chord C was maintained at 10,000 for each wing. The corresponding values of free-stream velocity for the wing was $U_\infty = 59.5$ mm/sec.

For acquisition of images, a digital charge-coupled device (CCD) camera was used to record the patterns of particle images. The camera was equipped with a 60 mm focal-length lens. Dantec flow grabber digital PIV software employing frame-to-frame adaptive-correlation technique was used to calculate the raw displacement vector field from the particle image velocity data. In PIV, the displacement field was determined as average displacements within so-called interrogation areas of the image plane. A typical size of these interrogation areas is 32x32 pixels, which means that one gets about 94x72=6768 vectors from an image with a resolution of 1600 x 1186 pixels. During the interrogation process, an overlap of 50% is employed in order to satisfy Nyquist criterion (Dantec Dynamıcs). A total of 900 instantaneous velocity vector fields were taken, with an acquisition frequency of 15 Hz for each continuous run. These instantaneous flow images were captured, recorded and stored on a computer in order to get the time-averaged velocity vectors and other flow statistics. The magnification factor *M* was determined to be 1:8.45, from the image of a millimeter scale located on the laser sheet in the flow field. Taking the magnification factor *M* into account, the actual grid size in the physical plane of the laser sheet was 2.64 mm X 2.64 mm. The overall field of view in the plane of the laser sheet was 248 mm X 190 mm. The digital PIV technique used in this study was similar to the one employed by Westerweel (1993), who calculated that the uncertainty in the velocity field was less than 2%. Extensive information about these

uncertainty factors affecting PIV measurements was reported by Gallanzi (1998), Hart (2000), Huang (1997) and Adrian (2005).
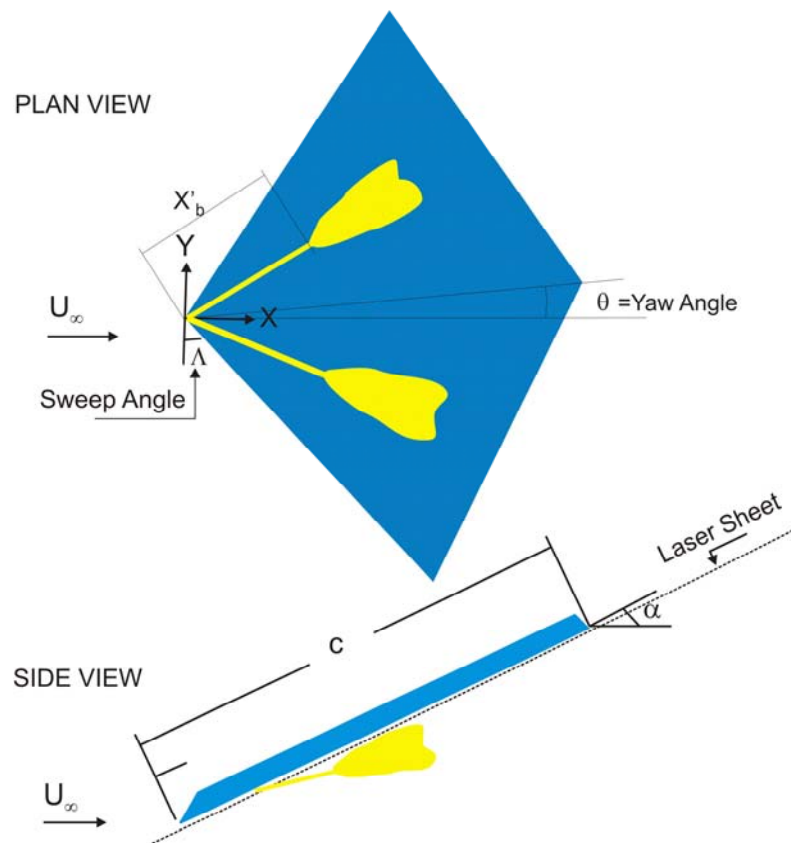
Figure 3.11. Simplified schematic of experimental arrangement of diamond planform.
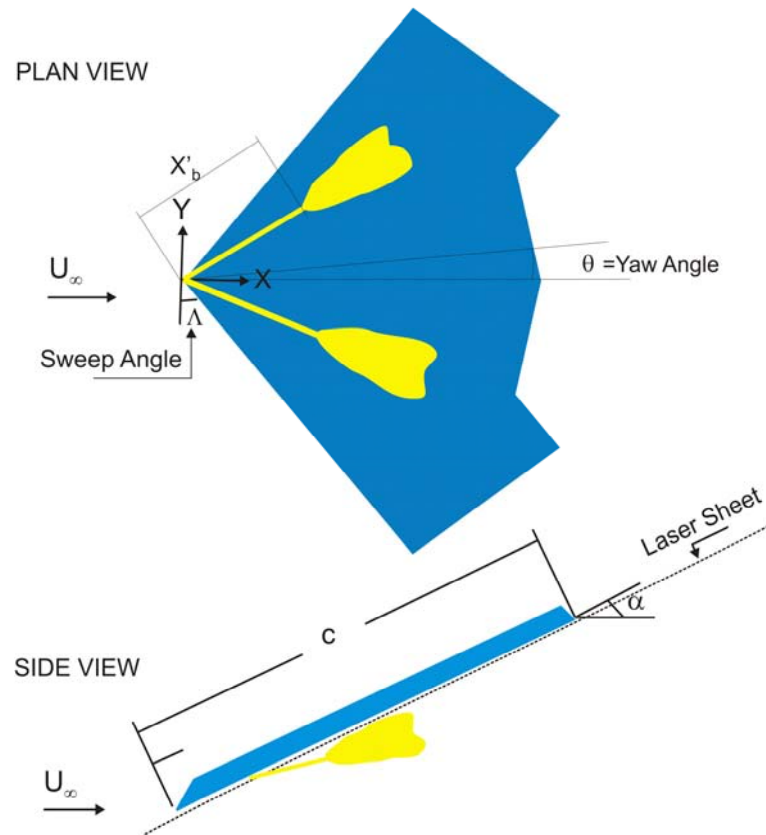
Figure 3.12. Simplified schematic of experimental arrangement of lambda planform.

4. RESULT AND DISCUSSIONS

4.1. Yaw Angle Effect on Flow Structure over the Nonslender Diamond Wing

4.1.1. Introduction

Delta wings have evolved over the years and are used primarily on many fighter aircrafts. As these aircrafts become more and more maneuverable, delta wing vortex dynamics and the effects and understanding of the physics of time-dependent unsteady flows have become substantially important (Heron and Myose, 2004). Several variables influence delta wing vortex dynamics. Some of these variables include angle-of-attack, leading edge geometry, wing thickness, sweep angle, free stream conditions, Reynolds number and yaw angle. The yaw angle, θ has a profound effect on the vortex structures. Little attention has been devoted to understanding the flow structure on simple delta wings of low sweep angle, let alone complex configurations such as Unmanned Combat Air Vehicle (UCAV) planforms. Digitally-based high-image-density particle image velocimetry is presently employed to determine the averaged structure of flows over the nonslender diamond wing.

4.1.2. Objective of the Present Work

In the present work, the structure of the vortical flow, occurred due to varying the yaw angle of the wing within the range of $0^o \leq \theta \leq 15^o$ for the angle of attack of $\alpha=10°$, is observed over a 40° sweep angle diamond wing using a laser based 3-dimensional Particle Image Velocimetry (PIV) technique and dye visualization technique. Experimental investigation on the unsteady flow over a wide range of yaw angles provided crucial understanding of the variations of the leading edge vortex cores, their breakdown behavior, aerodynamic hysteresis, and wing aerodynamic characteristics.

4.1.3. Experimental Arrangements and Instrumentations

Average free-stream velocity in the plan-view planes is U_{av} = 59.5 mm/sec which corresponds to Reynolds number Re_c = 10 000 based on the chord (C) and to Re_h =61 285 based on the open-channel hydraulic diameter for all experiments. The chord (C) of the diamond wing had a length of 168 mm. Actually, the diamond wing is consisted of a delta wing and an attachment part. The sweep angle of the wing was specified as Λ = 40°. In addition, the wing had a thickness (t) of 3 mm, and was beveled on the windward side at an angle of 45°. Dimensions of the diamond wing model and location of measuring plane are shown in Figure 4.1. During the experiments, the diamond wing model was kept stationary against the free-stream flow by a specially designed apparatus which include a servo motor.
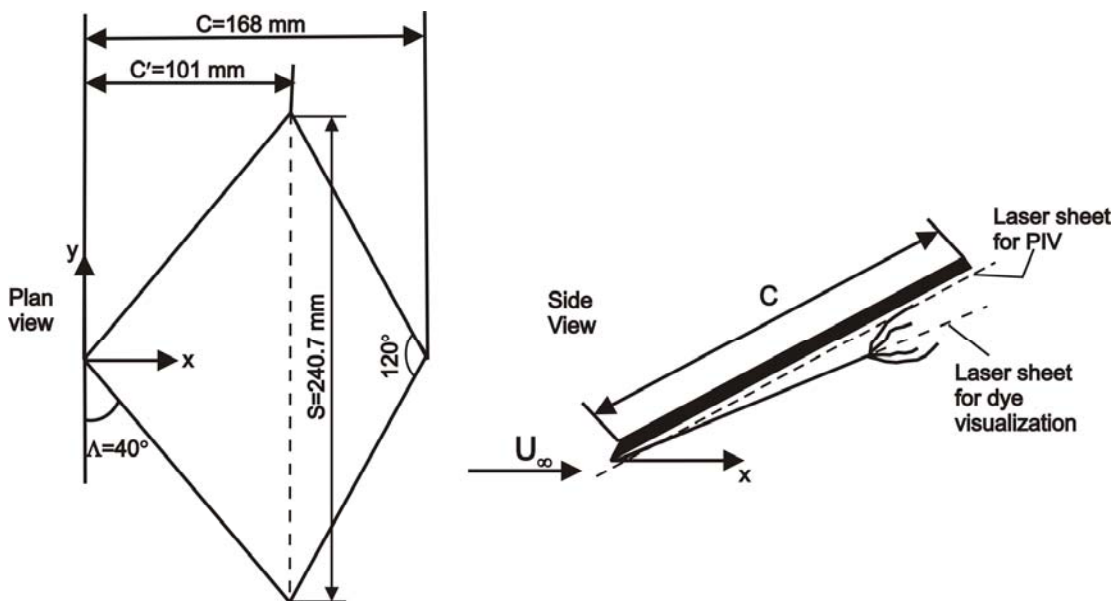
Figure. 4.1. Schematic of experimental arrangement showing diamond wing and laser-sheet location.

4.1.4. Dye Visualization

The results of dye visualization experiments at angles of attack of α=7° and 10° and yaw angles of θ=0°, 4°, 6° and 15° are shown in Figure 4.2. In the first column of Figure 4.2, the apparent centerlines of leading edge vortices are clearly

identified and vortex breakdown occurs after a certain distance from the diamond wing apex close to the trailing edge of the delta wing attachment for $\alpha=7^{o}$. The natural flow structure of the diamond wing generally contains a pair of main coherent vortices emanating from the leading edge of the diamond wing and vortex breakdown which is defined as decomposition of the leading edge vortex occurs.

As seen in the first row of Figure 4.2, which presents dye flow visualizations for zero yaw angle, the location of vortex breakdown comes closer to the diamond wing apex when the angle of attack is increased from $\alpha=7^{o}$ to $\alpha=10^{o}$. Moreover, there is a symmetrical flow structure over the diamond wing in the case of zero yaw angle. When the yaw angle gradually increases, the symmetrical flow structure between both sides of the chord axis of the diamond wing begins to deteriorate. The vortex breakdown location on the leeward side of the diamond wing is delayed comparing to that of the windward side. In other words, vortex breakdown moves upstream on the windward side of the diamond wing while it moves further downstream on the leeward side. As can be seen in Figure 4.2 for angles of attack of $\alpha=7^{o}$ and 10° for the cases of yaw angle less than $\theta=4^{o}$, the flow structure on both sides of the chord axis of the diamond wing is almost symmetric. Canpolat et al. (2009) indicated that the asymmetric flow structure started at the yaw angle of $\theta=6°$ for delta wing having a sweep angle of $\Lambda=40°$. Leading edge vortex axis on the windward side of the wing shifted its location towards the central chord axis and the vortex breakdown occurred at the location further upstream in the case of higher yaw angles, θ. Asymmetrical flow characteristics start at the yaw angle of $\theta=4°$ in the diamond wing case compared to the delta wing result reported by Canpolat at al. (2009). This changes in the flow characteristics occur due to the trailing edge configuration attached to the delta wing. At yaw angle, $\theta=15^{o}$, vortex breakdown occurs in the downstream region of the diamond wing's trailing edge of the leeward side but on the windward side vortex breakdown takes place close to the apex of the wing for both angles of attack $\alpha=7^{o}$ and 10°,.

From time to time, a well defined vortex in the wake flow region downstream of the onset of vortex breakdown reverses back anticlockwise direction to form a

swirling-type of flow which rotates anticlockwise about its axis which is perpendicular to the measuring plane (paper plane) and moves in the upstream direction when the yaw angle increases to a value of $\theta=15^o$ at $\alpha=10^o$. In addition, the leading edge vortex is arced starting from the apex and later this curved leading edge vortex is divided into two branches as seen in the third images of Figure 4.3. Finally, this curved leading edge vortex turns into elongated shape and continues to rotate around the straight line as a core vortex and hence onset of the vortex breakdown moves further downstream as seen in Figure 4.3. Between the curved part of the leading edge vortex and windward side edge of the wing a rather week swirling-type vortex takes place rotating about its axis which is perpendicular to the measuring plane. Furthermore, similar observation on the delta wing with sweep angle of $\Lambda=40^o$ was also done by Canpolat et al. (2009) as seen in last two images of Figure 4.3. In the case of the delta wing, this swirling-type (focus) vortex is well defined next to the curved leading edge vortex comparing to the diamond delta wing case. In both wing cases, the domain of this swirling-type vortex enlarges its size time to time in a quasi periodic basis. When this vortex gets its largest shape, the leading edge vortex disintegrates in the upper stage causing vortex breakdown location to occur close to the apex.
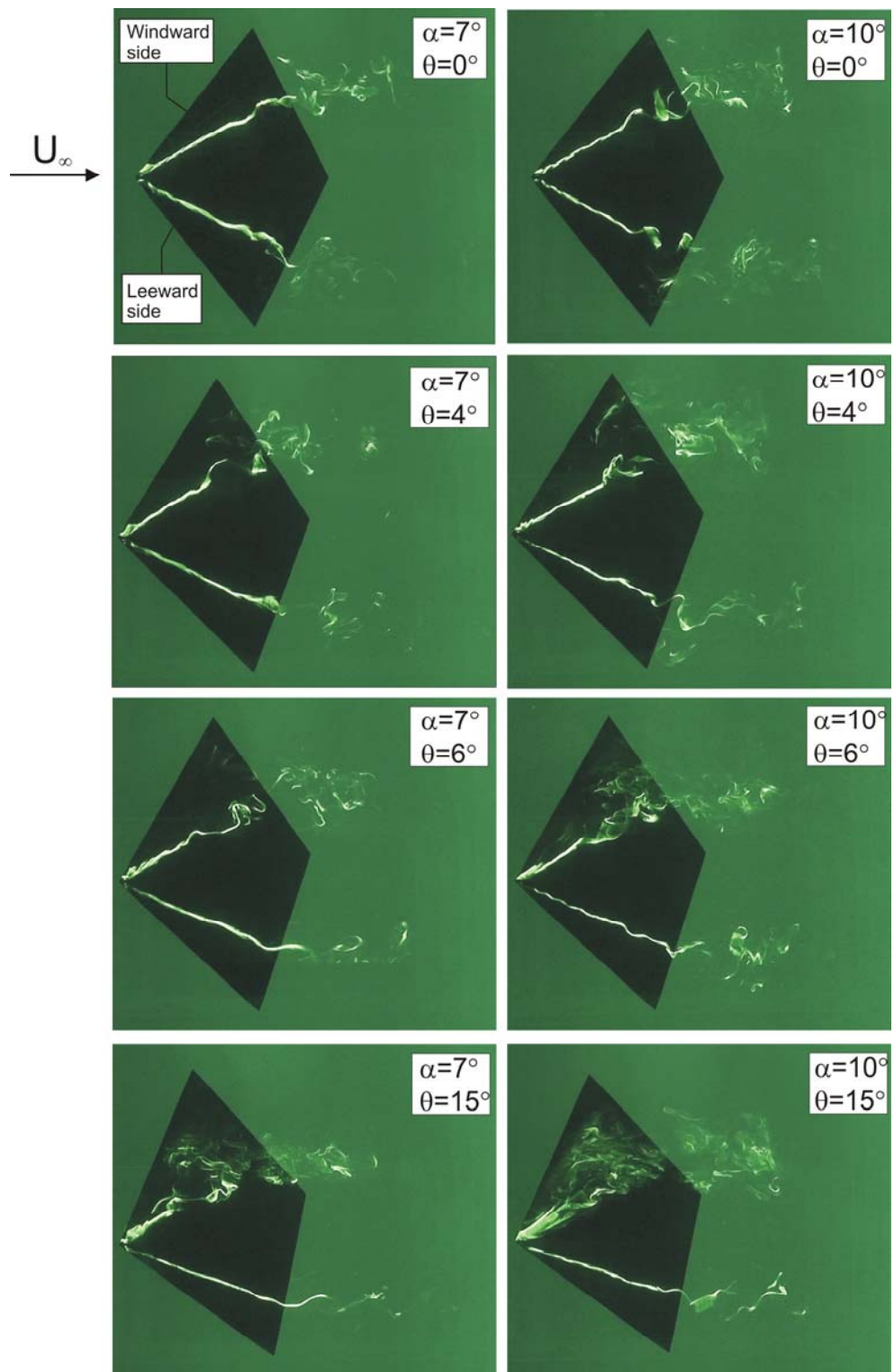
Figure. 4.2. Formation and development of leading edge vortex, vortex breakdown and separated flow region as a function of angle of attack, α and yaw angle, θ.
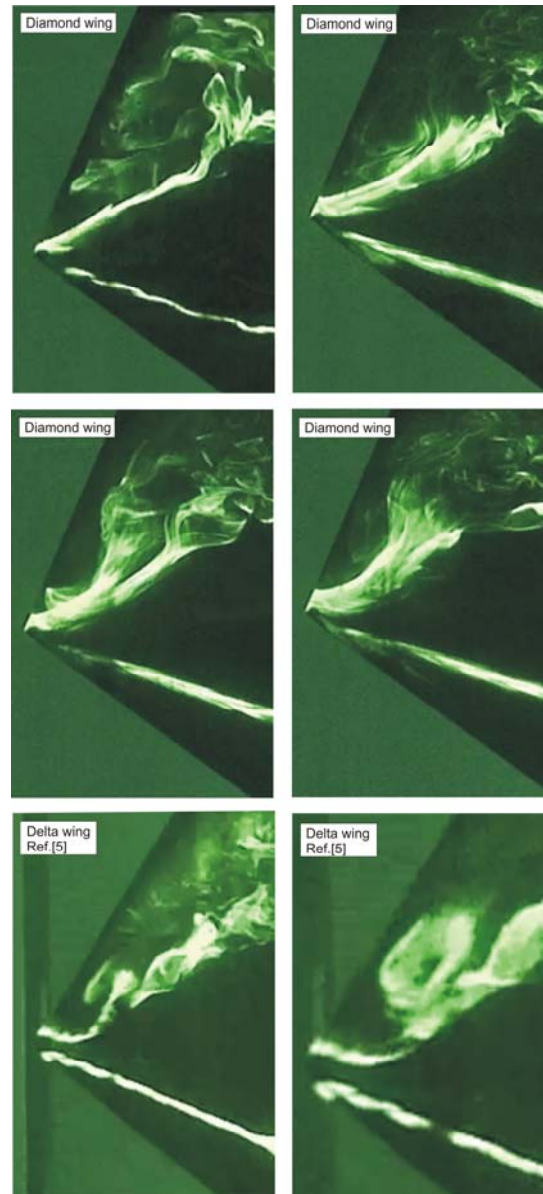
Fig. 4.3. Formation and distortion of leading edge vortex, vortex breakdown and swirling-type vortex for angle of attack, $\alpha=10^{o}$ and yaw angle, $\theta=15^{o}$.
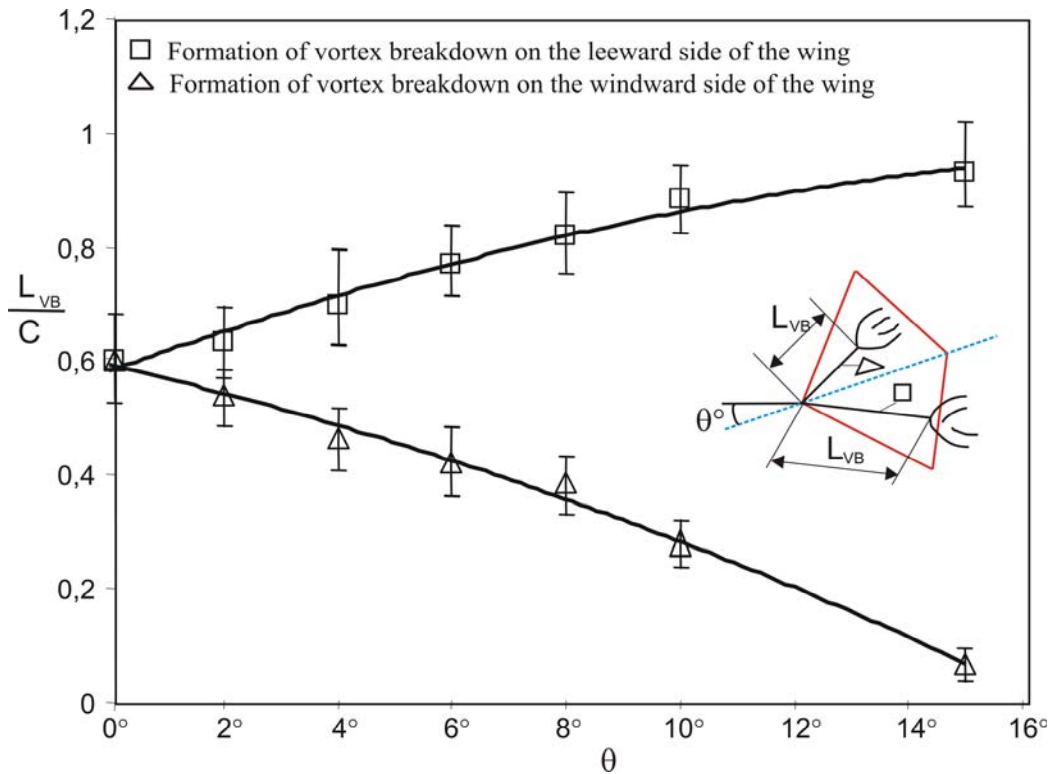
Figure. 4.4. Location of vortex breakdown, L_{VB}/C for the angle of attack of $\alpha=10°$.

Variations in dimensionless location of vortex breakdown, L_{VB}/C against yaw angle is presented in Figure 4.4 for angles of attack of $\alpha=7°$ and $10°$. Distance between the leading edge of the wing and vortex breakdown location is designated as L_{VB} and normalized by cord length as L_{VB}/C. Vortex breakdown location on the windward side moves towards the leading edge of the wing whereas vortex breakdown location on the leeward side moves further downstream. For example, vortex breakdown at yaw angle of $\theta=15°$ occurs at a location of $L_{VB}/C=0.05$ for the angle of attack of $\alpha=10°$. Video of dye visualization indicates that vortex breakdown developed over the wing is obliged to move backwards and forwards along the leading edge vortex axis. These variations are shown with a vertical solid line between two bars on each data. Finally, it can be concluded that a symmetrical flow structure over the suction surface of the wing deteriorates substantially when yaw angle is increased to a higher level.

4.1.5. Patterns of Time-Averaged Streamwise and Transverse Velocity Components

The first column of Figure 4.5 shows the consequence of all yaw angles on the contours of streamwise velocity component, <u>/U. The second column of the same figure shows the patterns of dimensionless transverse velocity component, <v>/U. Contours represented by the solid and dashed lines, demonstrate positive and negative streamwise and transverse velocity components, respectively. The minimum and incremental values of contours of dimensionless streamwise velocity, <u>/U and transverse velocity, <v>/U components for all yaw angles were kept constant for better comparison between the time-averaged velocity components. The maximum values of positive streamwise, <u>/U and transverse velocity components, <v>/U are 0.92 and 0.25 on the other hand, magnitude of the maximum values of negative velocities are 0.1 and 0.25 for all yaw angles, respectively. The vortex breakdown occurs closer to the apex on the windward side of the wing and other vortex breakdown occurs close to the trailing edge on the leeward side of the wing as seen from the dye visualization images presented in figure 4.2. Nevertheless, it is remarkable that this discernible alteration of the onset of vortex breakdown seems to have remarkable influence on the patterns of <u>/U and <v>/U even in the near surface of the wing.

As seen in the first image of the contours of the time-averaged streamwise velocity component, <u>/U, a negative velocity distributions take place on both side edges of the wing. Dotted line located between positive and negative streamwise velocity components indicates the zero value of <u>/U. The domain of the negative velocities, <u>/U gets smaller in size when the yaw angle, θ of the wing increases. As indicated in the last image of the first column of figure 4.5 this negative velocity component is vanished on the leeward side at a yaw angle of $\theta=15°$.

In the second column of Figure 4.5, there are two well-defined clusters of main positive and negative contours at both sides of the wing chord axis in the case of

θ=0° for transverse velocity component, <v>/U. Three different pairs of clusters of transverse velocity, <v>/U components were developed over the surface of the wing. The first pair that is symbolized as A, generates clusters of main positive and negative contours at both sides of the diamond wing chord axis in the case of θ=0°. The second pair that is symbolized as B takes place between clusters A and C. Lastly, the third pair of clusters of transverse velocity, <v>/U designed as C occurs along the side edges of the wing. The transverse velocities patterns which is symbolized as A and C on the windward side of the wing are positive, and the transverse velocity patterns of A and C on the leeward side of the wing are negative. For the second pair clusters, B vice versa condition is valid, i.e. transverse velocity patterns of B on the windward side of the wing are negative, velocities on the leeward side of the wing are positive. The effect of free-stream velocity at the leading edge of the wing decreases by increasing yaw angle. As a result of increasing the yaw angle to a higher value, a wake flow region is expanded over the surface of the wing and transverse velocity patterns, <v>/U symbolized as B, is vanished at a yaw angle of θ=15°.
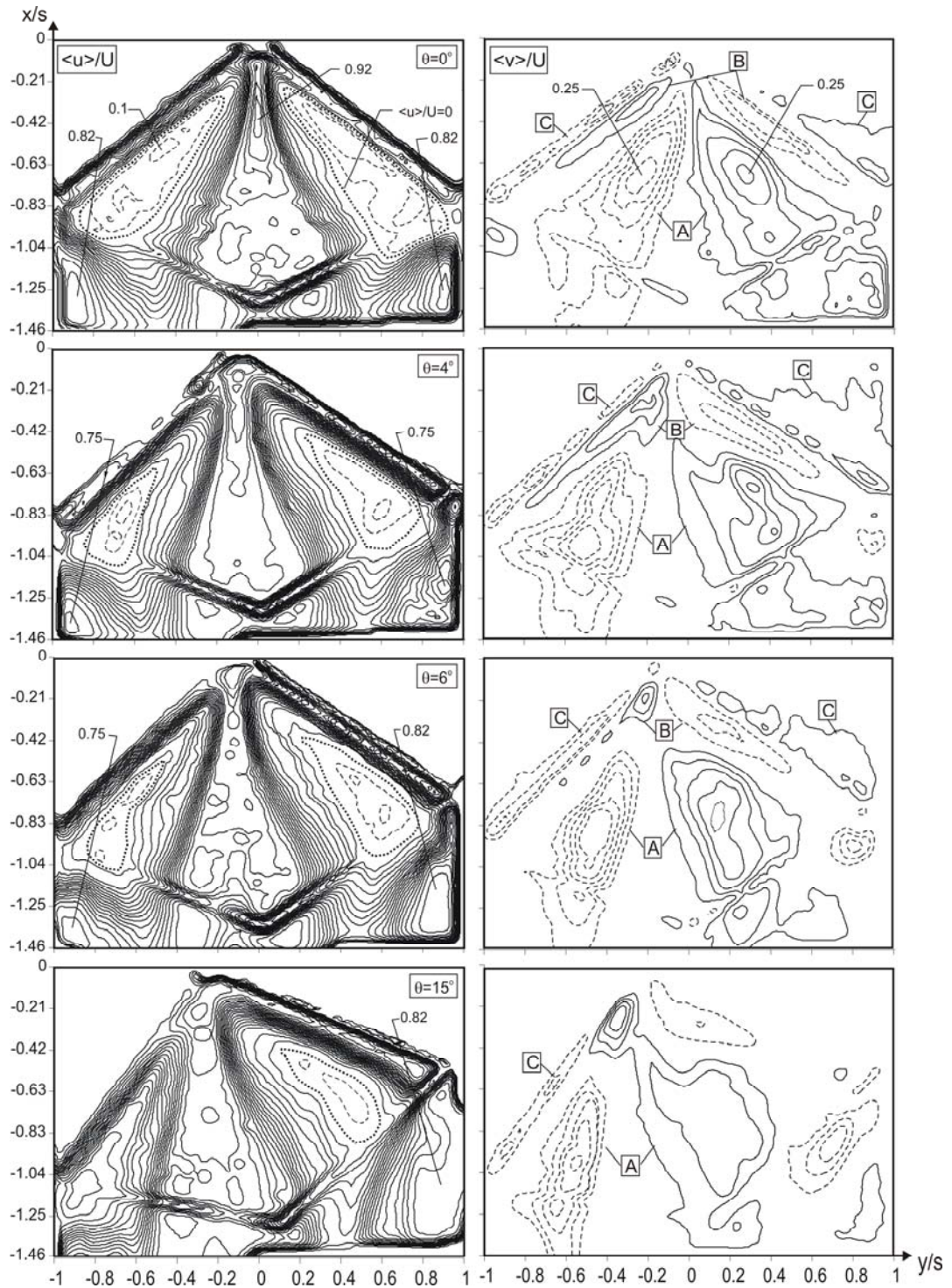
Figure. 4.5. Patterns of time-averaged components of streamwise, [<u>/U] and transverse, [<v>/U] velocity for the angle of attack *α*=10°. Minimum and incremental values are [<u>/U]_min =0.05, [<v>/U]_min =0.05 and Δ[<u>/U] =0.05, Δ[<v>/U] =0.05.

4.1.6. Patterns of Fluctuating Velocity

Patterns of the root mean square of streamwise, transverse and vertical velocity components, u_{rms}/U, v_{rms}/U and w_{rms}/U normalized by free-stream velocity U are presented in figure 4.6. The maximum values of the root mean square of these velocity coponents Are indicated on the images. The distributions of u_{rms}/U, v_{rms}/U and w_{rms}/U on both sides of the chord axis are identical for zero yaw angle $\theta=0^o$ and coincident with the footprint of the leading-edge vortices presented in Figure 4.2. But, the magnitudes of u_{rms}/U and v_{rms}/U are gradually attenuated over the surface of the wing on the leeward side and the location of the maximum values moves further downstream when the yaw angle of the wing is increased. On the other hand, the maximum values of u_{rms}/U are the same on the windward side of the wing and the locations of the maximum values move further upstream over the range of yaw angle $0°\leq \theta \leq15°$. Broader patterns of u_{rms}/U occur in accord with the onset of the swirling-type vortex shown in Figure 4.4 at the yaw angle of $\theta=15°$. Contrarily, u_{rms}/U is attenuated to a value of 0.09 over the wing surface on the leeward side of the wing. These attenuations happen due to the formation of onset of vortex breakdown downstream of the trailing edge of the wing. Root mean square of transverse velocity component v_{rms}/U attenuates over the whole wing surface as the yaw angle increases from $\theta=0°$ to $\theta=15°$. The patterns of w_{rms}/U are dramatically broadened over the wing surface comparing to the patterns of u_{rms}/U and v_{rms}/U and the peak values of w_{rms}/U are the same for the whole range of the yaw angle.

Reynolds stress correlations $<u'v'>/U^2$ and $<u'w'>/U^2$ normalized by the square root of the free-stream velocity U^2 are shown in figure 4.7. To allow direct comparison, the minimum and incremental values of Reynolds-stress contours were kept constant for all cases of yaw angle. Reynolds-stress concentration $<u'v'>/U^2$ has a coincidence with the components of root-mean-square of velocity fluctuations u_{rms}/U and v_{rms}/U.

Although images were taken in close proximity to the surface of the wing, the structure of vortex breakdown has a considerable effect on the wake region.

Reynolds-stress correlations $<u'v'>/U^2$ and $<u'w'>/U^2$ as a set of extreme on either side of the cord axis appear on the identical locations. The concentration of Reynolds-stress distributions $<u'v'>/U^2$ and $<u'w'>/U^2$ occupy a wider region on windward side and have a higher values comparing to the leeward side of the wing when yaw angle is increased. If a comparison done between cases of $\theta=4^o$ and $\theta=0^o$, it will be seen that there is a decrease in the value of maximum concentration of turbulence characteristics so that even very small yaw angles affect this concentration. Namely, the strength of $<u'v'>/U^2$ is attenuated and central point of the extreme moves further downstream in the flow direction when the yaw angle is increased.
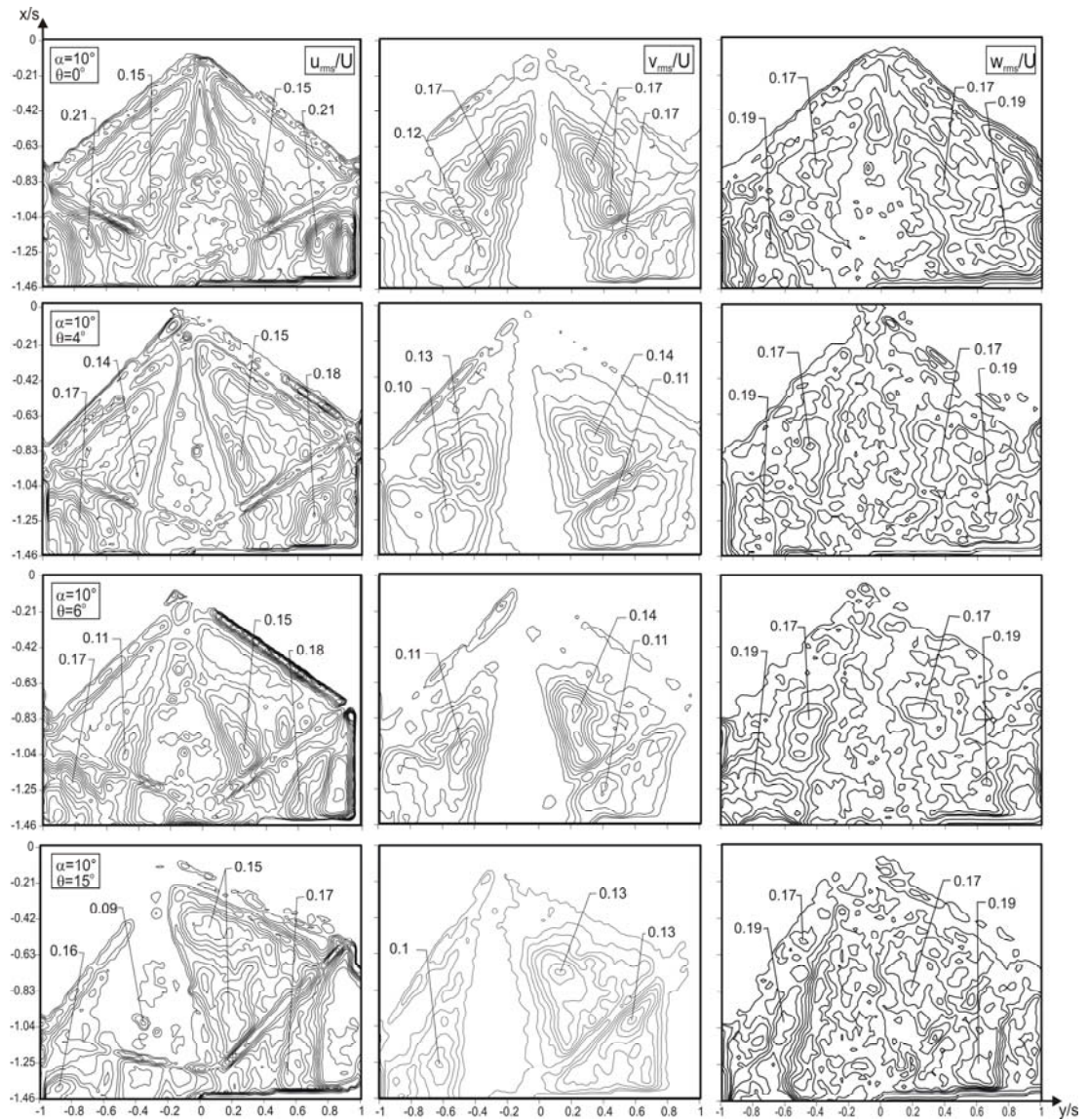
Figure. 4.6. Consequence of yaw angle on patterns of rms of the streamwise and transverse velocity fluctuation respectively, u_{rms}/U, v_{rms}/U for angle of attack of $\alpha=10^o$. For contours of constant u_{rms}/U, $[u_{rms}/U]_{min} = 0.01$, and $\Delta[\,u_{rms}/U] = 0.015$. For contours of constant v_{rms}/U, $[v_{rms}/U]_{min} = 0.01$, and $\Delta[\,v_{rms}/U] = 0.015$, $[w_{rms}/U]_{min} = 0.01$, and $\Delta[\,w_{rms}/U] = 0.015$.
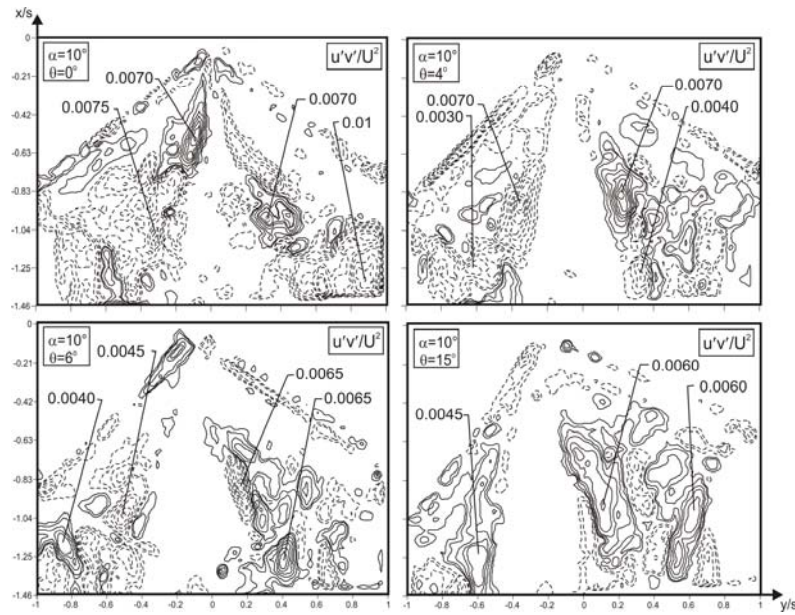
a) Contours of constant Reynolds-stress correlation, $[<u'v'>/U^2]_{min} = \pm 0.0005$, and $\Delta[<u'v'>/U^2] = 0.001$.
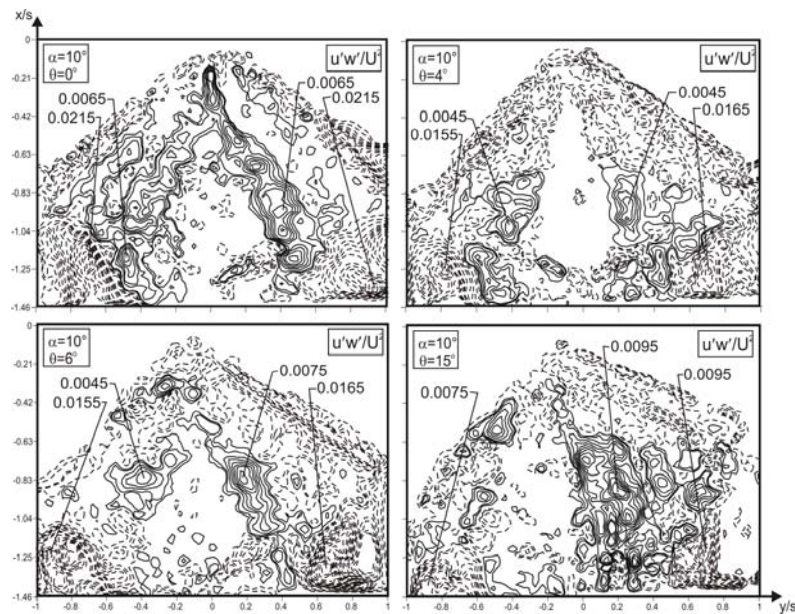
b) Contours of constant Reynolds-stress correlation, $[<u'w'>/U^2]_{min} = \pm 0.0005$, and $\Delta[<u'w'>/U^2] = 0.001$.

Figure. 4.7. Consequence of yaw angle on patterns of Reynolds stress correlations $<u'v'>/U^2$ and $<u'w'>/U^2$ for the angle of attack of $\alpha=10^o$.

4.1.7. Averaged Vorticity and Streamline Topology

Patterns of time-averaged vorticity $<\omega>$ and streamline topology $<\Psi>$ for angle of attack of $\alpha=10^o$ and yaw angles of $0°\leq \theta \leq 15°$ are presented in Figure 4.8. The first column of Figure 4.8 shows that patterns of the time-averaged streamline topology $<\Psi>$. There is a symmetrical flow structure in the case of zero yaw angle $\theta=0^o$. A pair of well defined foci which is designated as F_1 and F_2 are developed near the apex over the wing surface for angle of attack, $\alpha=10^o$ and zero yaw angle, $\theta=0^o$. On the other hand, foci, F_3 and F_4 occur in the outboard region of the wing. The positive bifurcation line of each vortex L^+ gets closer to each other because of the approximation of the foci, F_1 and F_2. Along the leading edge, negative bifurcation lines $\overline{L}$ are formed. On these bifurcation lines $\overline{L}$ saddle points S take place. These saddle points occur near the trailing edge of the diamond wing. At $\alpha=10^o$ and $\theta=0^o$ as seen in the first image of the first column of Figure 4.8, a negative bifurcation line $\overline{L}$ expends over a substantial extent of the leading edge. It corresponds to the merging of streamlines towards the single line, and represents a line of separation. In addition, a positive bifurcation line L^+ is evident. It can be recognized from the diverging motion of streamlines toward the single line. As seen in the case of $\alpha=10^o$ and $0°\leq \theta \leq15°$, the flow structure adjacent to the surface of the diamond wing is more sensitive with yaw angle. Figure 4.8 shows that well defined foci, F_1 and F_4 are formed on the windward side of the wing immediately downstream of the wing apex and foci, F_2 does not form on the leeward side of the wing in the case of yaw angle $\theta=4°$. As yaw angle is applied to the wing, the symmetry of the time-average flow topology is deteriorated. Generally, the time-averaged streamline pattern, $<\Psi>$ tends to be less curved and try to be elongated its lengthwise direction at the leeward side of the wing as a function of yaw angle.

The second column of Figure 4.8 shows the patterns of time-averaged vorticity $<\omega>$ for each yaw angles. To be able to make direct comparison, for the contours of time-averaged vorticity $<\omega>$ minimum and incremental values was taken same values as $[<\omega>]_{min} =0.4$ s^{-1} and $\Delta[<\omega>] =0.7$ s^{-1}, respectively. The maximum

value of the contours of time-averaged vorticity, $<\omega>$ is 4.9 s^{-1} and this value does not change on the windward side of the wing for all yaw angles. Figure 4.8 shows that when yaw angle is increased, values of the contours of time-averaged vorticity $<\omega>$ decrease on the leeward side of the wing due to the movement of vortex breakdown location further downstream of the trailing edge of the wing In the first image of the second column of the figure 4.8, there is a pair of well defined vortices which emanates from the leading edge of the diamond wing and consists of two well-defined clusters of negative and positive time-averaged vorticity $<\omega>$. These pair of vortices are designated as A. Along the side edges of the wing elongated vortices occur which are designated as E. They occur due to the three dimensional instability of the shear layer separating from the windward surface of the wing. When the wing is yawed, clusters of positive time-average vorticity occurred between two defined clusters of negative time-averaged vorticity on the windward side of the wing which is designated as D. These D contours can be seen in the cases of yaw angles $\theta \geq 4°$.
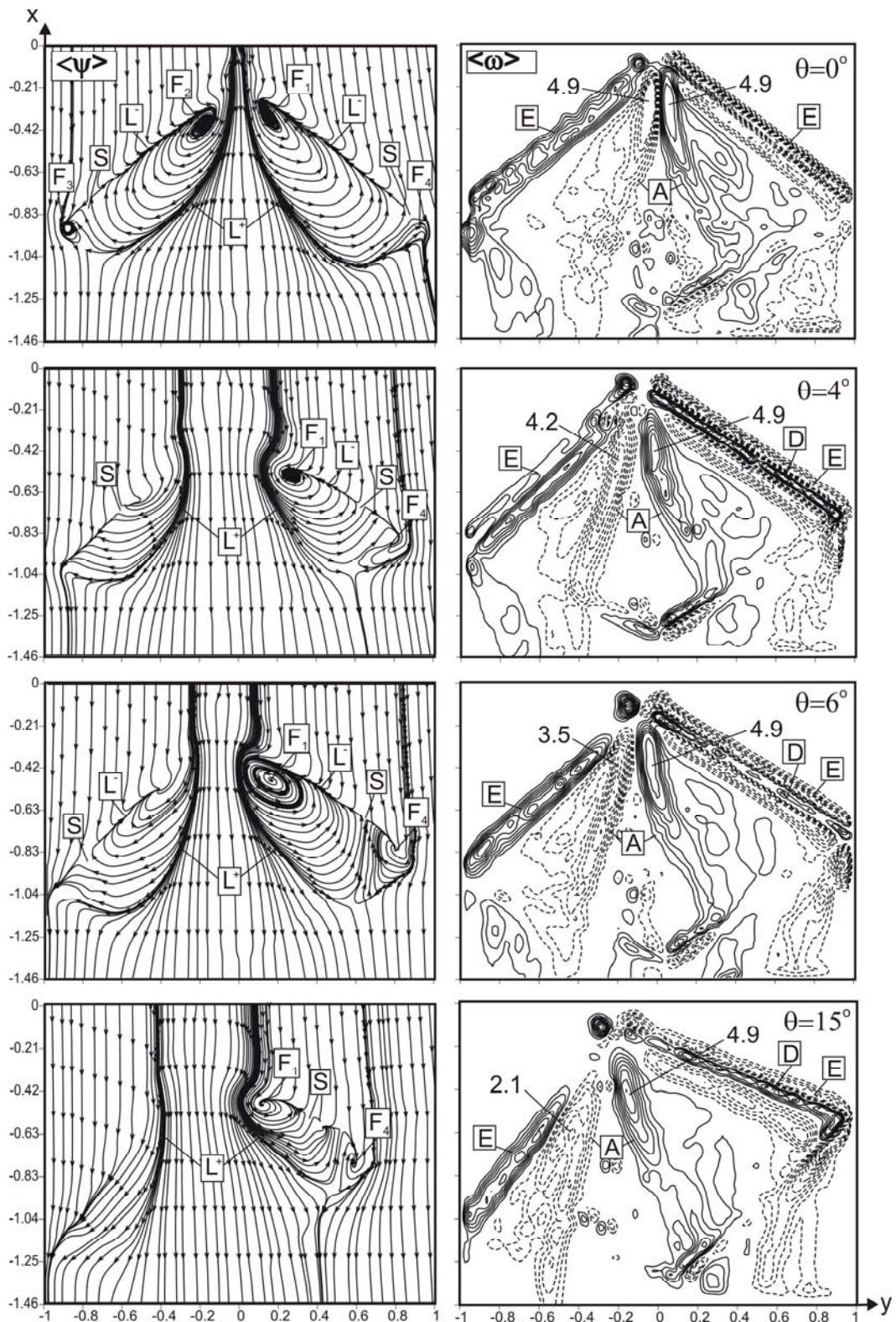
Figure. 4.8. Patterns of streamline, $<\psi>$ and time-averaged vorticity, $<\omega>$ for angle of attack of $\alpha=10^{\circ}$.

4.1.8. The Normalized Components of the Reynolds Normal Stresses and Turbulent Kinetic Energy (TKE)

As expected, the analysis of the dimensionless fluctuating velocity component indicates that the maximum of turbulence level occur in the shear layer. Figure 4.9 indicates streamwise, transverse and vertical Reynolds normal stress correlations, $<u'u'>/U^2$, $<v'v'>/U^2$ and $<w'w'>/U^2$ to reveal its effect on turbulent kinetic energy under the variation of the yaw angles such as $0° \leq \theta \leq 15°$. The minimum and incremental values of contours for streamwise and transverse Reynolds normal stresses, $<u'u'>/U^2$, $<v'v'>/U^2$ are the same and equal to 0.002 and 0.002, respectively. Also the minimum and incremental values of contours for vertical Reynolds normal stresses, $<w'w'>/U^2$ are 0.002 and 0.005, respectively. Figure 4.9 shows that the maximum values of transverse and streamwise Reynolds normal stresses, $<u'u'>/U^2$, $<v'v'>/U^2$ decrease with increasing yaw angle, on the other hand the maximum value of vertical Reynolds normal stress, $<w'w'>/U^2$ does not change with increasing yaw angle. The maximum values of normalized streamwise Reynolds normal stress, $<u'u'>/U^2$ are 0.042, 0.036, 0.036 and 0.028 and for normalized transverse Reynolds normal stress, $<v'v'>/U^2$ the values are 0.015, 0.014, 0.012 and 0.01, respectively, for yaw angle of $0° \leq \theta \leq 15°$. The maximum value of normalized vertical Reynolds normal stress, $<w'w'>/U^2$ is 0.035 for all yaw angles.

Results of the turbulent kinetic energy, TKE for all yaw angles in angle of attack of $\alpha = 10°$ are shown in Figure 4.10. In order to make a direct comparison, for minimum and incremental values of the contours of time-averaged turbulent kinetic energy, TKE was taken same values as $[<TKE>]_{min} = 0.004$ and $\Delta[<TKE>] = 0.004$, respectively. The maximum value of TKE for all yaw angles is 0.03. Turbulent kinetic energy, TKE is related to the normalized components of the Reynolds normal stresses, $<u'u'>/U^2$, $<v'v'>/U^2$ and $<w'w'>/U^2$. Figure 4.9 shows that, when yaw angle increases, magnitudes of the normalized components of the Reynolds normal stresses, $<u'u'>/U^2$, $<v'v'>/U^2$ and $<w'w'>/U^2$ get lower values on the leeward side

of the wing compared to the values on the windward side of diamond wing. TKE decreases on the leeward side of the wing surface since the fluctuations are less in this region, due to vortex breakdown location moves downstream region of the trailing edge of the wing. The change in the turbulent kinetic energy on the windward side of the wing is negligible for different yaw angles. In Figure 4.9, examining the maximum values of the normalized components of the Reynolds normal stresses, $<u'u'>/U^2$, $<v'v'>/U^2$ and $<w'w'>/U^2$, it is seen that, value of the transverse Reynolds normal stress, $<v'v'>/U^2$ is smaller than the streamwise and vertical Reynolds normal stresses, $<u'u'>/U^2$ and $<w'w'>/U^2$. So, effect of transverse Reynolds stress on the formation of TKE is smaller than the effects of streamwise and vertical Reynolds stresses.
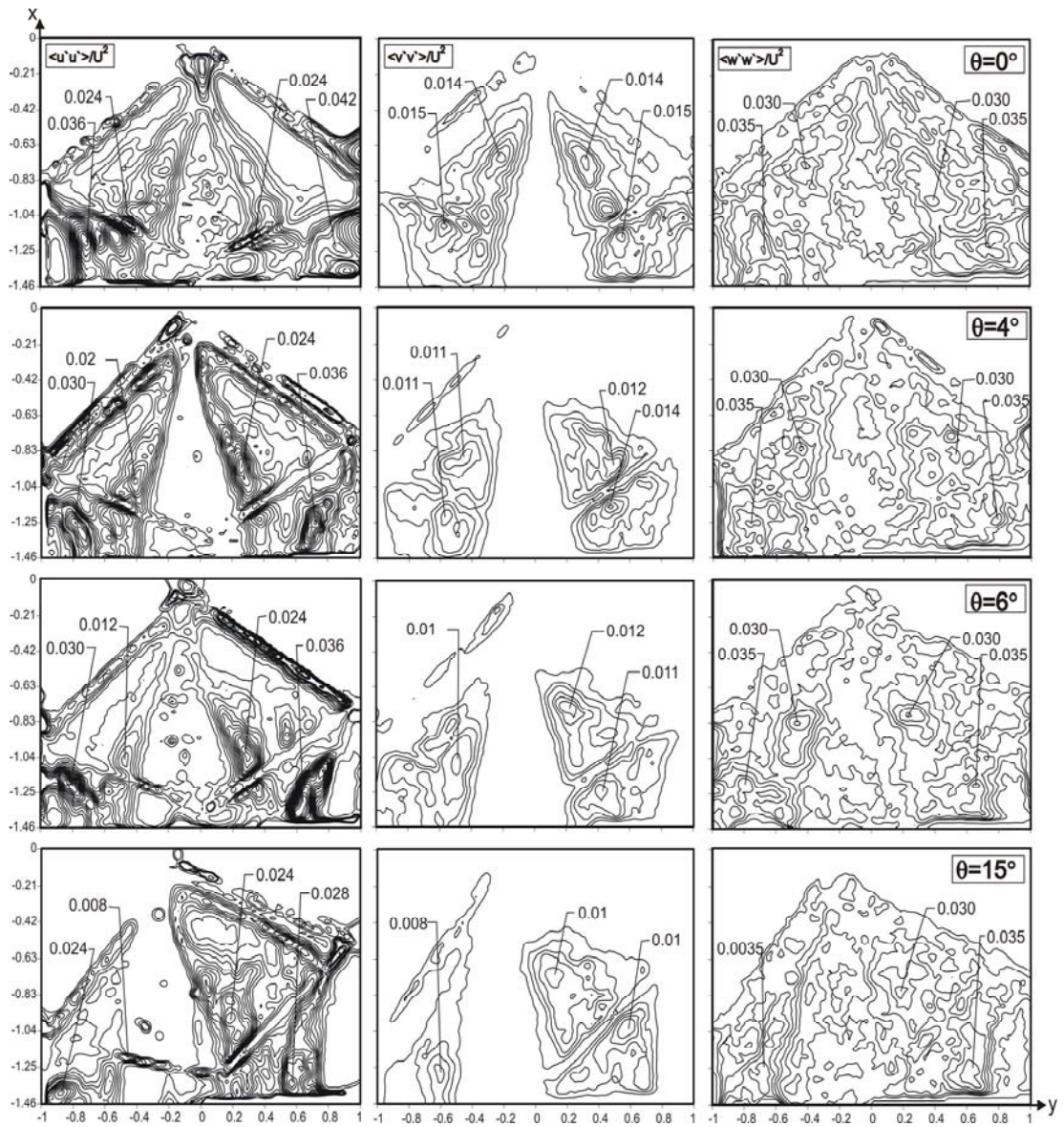
Figure 4.9. The contours of time-averaged Reynolds normal stress components for the angle of attack of $\alpha=10^o$.
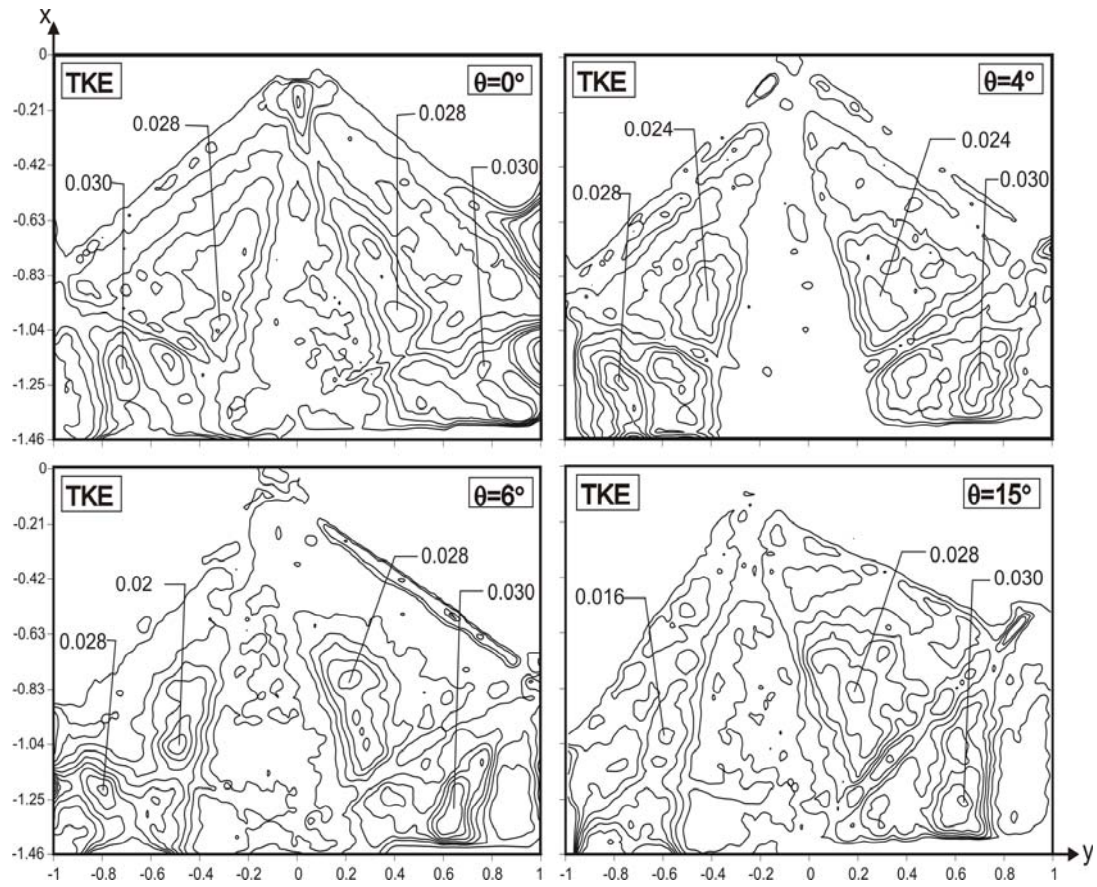
Figure 4.10. The contours of time-averaged turbulent kinetic energy (TKE) for the angle of attack of $\alpha=10^{\circ}$.

4.2. Effect of Angle of Attack on the Flow Structure over the Nonslender Lambda Wing

4.2.1. Introduction

Unsteady aerodynamics of nonslender delta wings, consisting of shear layer instabilities, the structure of vortices, the occurrence of breakdown, and fluid structure interactions were extensively reviewed by Gursul et al. (2005). They emphasized the sensitivity of the vortical flow structures varying the angle of attack α of the nonslender lambda wing. As already known, altitude loss of airplane on air (stall) is concerned by increasing angle of attack. Knowledge about the aerodynamic properties of the lambda wing in unsteady motion is vitally important in applications.

4.2.2. Objective of the Present Work

In the present work, the vortical flow structure, occurred due to variation of the angle of attack within the range of $7^o \leq \alpha \leq 17^o$ is observed over a $\Lambda = 40^o$ sweep angle lambda wing using a laser based 3-dimensional Particle Image Velocimetry (PIV) and dye visualization techniques. Experimental investigation on the unsteady flow over a wide range of angle of attacks provided crucial understanding of the variations of the leading edge vortex cores, their breakdown behavior, unsteady flow region downstream of the vortex breakdown and wing aerodynamic characteristics.

4.2.3. Experimental Arrangements and Instrumentations

Average free-stream velocity in the plan-view planes are U= 59.5 mm/sec which correspond to Reynolds numbers $Re_c = 10\ 000$ based on the chord (C) and $Re_h = 61\ 285$ based on the open-channel hydraulic diameter for all experiments. The chord (C) of the lambda wing had a length of 168 mm. The sweep angle of the wing was specified as $\Lambda = 40°$. In addition, the wing had a maximum thickness (t) of 3 mm, and was beveled on the windward side at an angle of 45°. Dimensions of the lambda wing model and location of measuring plane are shown in Figure 4.11. During the

experiment, the lambda wing model was kept stationary against the free-stream flow by a specially designed apparatus which included a servo motor.
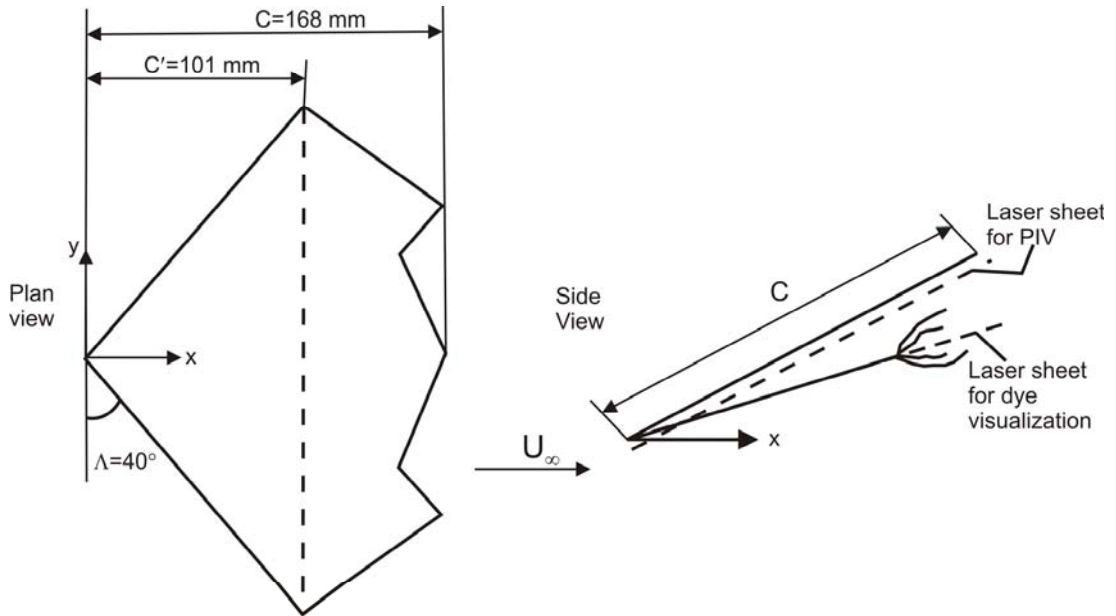
Figure. 4.11. Schematic of experimental arrangement showing lambda wing and laser-sheet or measuring plane locations.

4.2.4. Dye Visualization

The results of dye visualization experiments at four different angles of attack ($\alpha=7^o$, 10°, 13° and 17°) are shown in Fig. 4.12. For $\alpha=7^o$ and 10°, coherent leading edge vortices emanating from the leading edge of the lambda wing are clearly identifiable and it is obvious that vortex breakdowns occur after a certain distance from the lambda wing apex at a wandering locations. There is a symmetrical flow structure over the lambda wing on both side of the central axis for angle of attacks of $\alpha=7^o$ and 10° in macro scale. The mean structure of the vortex system changes as the angle of attack of the wing varies.

As can be seen from Figure 4.12 at an angle of attack of $\alpha=10°$, this elongated separated flow region can take on an interesting dual vortex structure. At upstream locations near the apex, the long, and thin shear layer that emanates from the leading edge of the lambda wing terminates in the formation of the primary vortex. Further

downstream a secondary vortex, with vorticity of the same sign as the primary vortex, emerges in the separated shear layer outboard of the primary vortex creating a dual vortex structure. This secondary vortex, which is slightly weaker and smaller than the primary vortex, arises from the interaction of the secondary flow with the primary shear layer. Distance between the leading edge of the wing and vortex breakdown location is designated as L_{VB} and normalized by cord length as L_{VB}/C. In addition, the leading edge vortex breakdown locations move in the upstream direction by a large L_{VB}/C fraction over a small range of angle of attack such as $7^0 < \alpha < 10^0$.

For the angle of attack $\alpha = 13^0$, both leading edge vortices are not seen at the wing apex, i.e. formation of vortex breakdown nearly starts form the wing apex. Since the dye is swept downstream past the trailing edge, the central portion of the wing looks unaffected from the dye. On the other hand, the regions of the wing outboard of this central portion show a low velocity region of dye adjacent to the surface. Vortex breakdown occurs earlier compared to the slender wings at low incidences due to the stronger adverse pressure gradient developed as a consequence of the trailing edge attached to the delta wing. At high angle of attack $\alpha = 17^0$ entire surface of the wing is covered with a region of low-velocity dye.

Distance from apex measured along plane of symmetry of wing is designated as x and normalized by chord length as x/C. Dye observation was also conducted in cross flow planes such at a location of x/C=0.6 as shown in Fig. 4.13 in order to study vortical flow structure at a cross-flow planes further downstream of the vortex breakdown location. As soon as vortex breakdown occurs a coherent leading edge vortex core disintegrates into small scale vortices. The main spanwise rotating vortices occur in the inner side of the leading edge close to the central axis of the lambda wing. Small size vortices are also developed next to the main rotating vortices. These secondary vortices get smaller in size when they move closer to the side edges of the lambda wing. The outer line of the separated flow region gradually moves downward from the surface of the lambda wing while the angle of attack is increased. Between the surface of the lambda wing and vortical flow structure, there is an interaction. By increasing angle of attack of the wing, area or diameter of

separated flow region increases in size and the flow covers the wing surface completely.
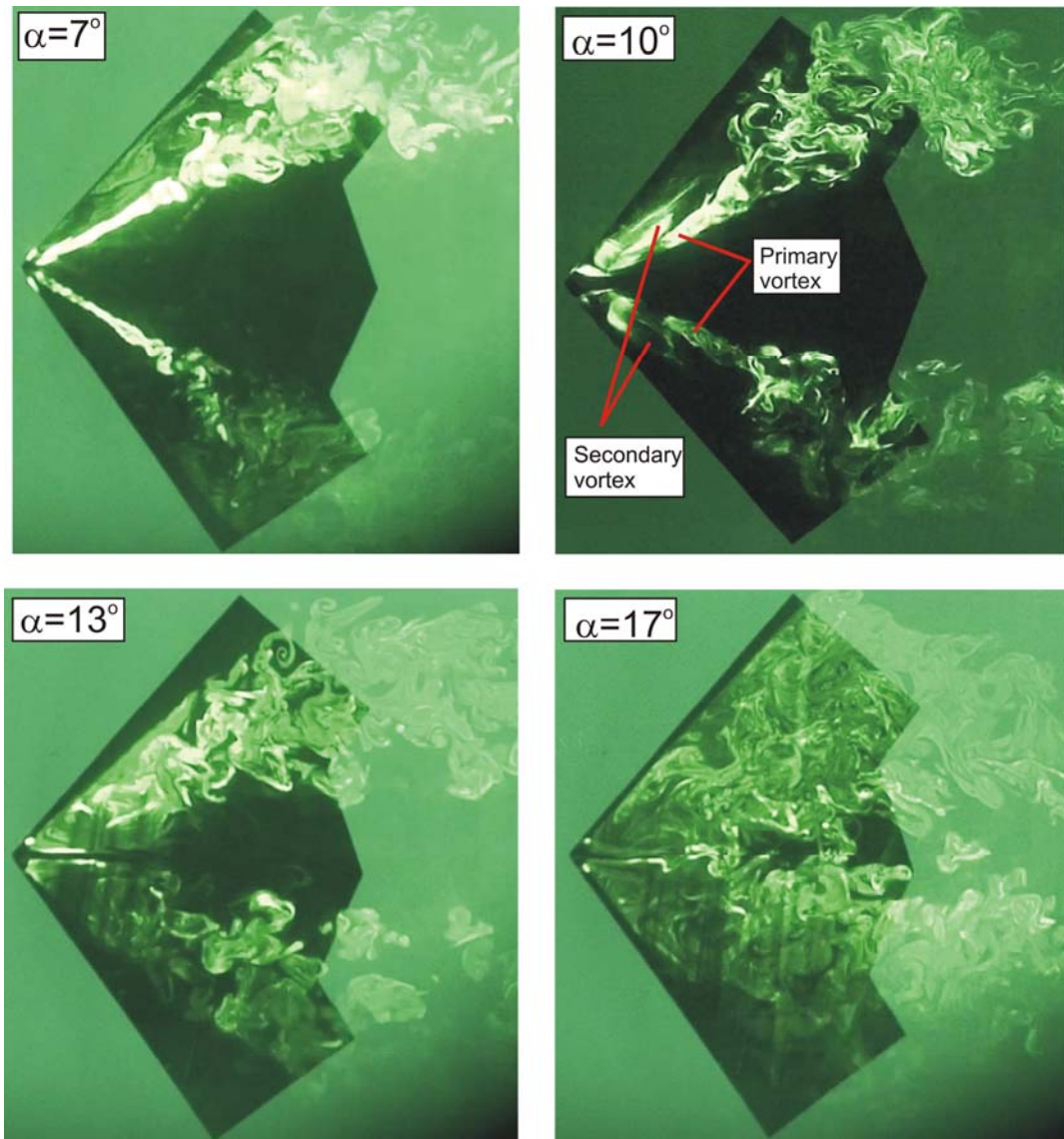
Figure. 4.12. Formation and development of spiral vortex, vortex breakdown as a function of angle of attack observed in plan-view plane.
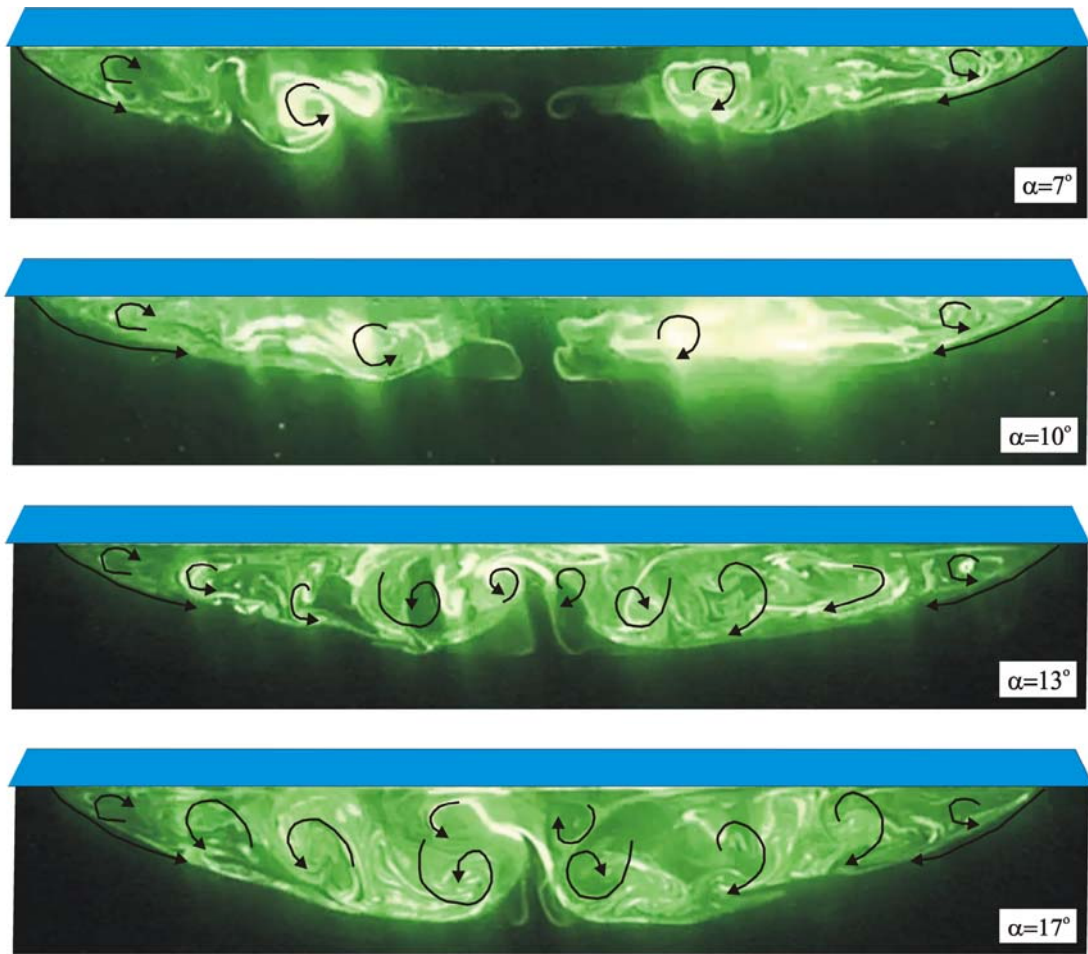
Figure. 4.13. The formation and development of a vortex structure in end-view plane.

4.2.5. Near-Surface Streamline Topology

Patterns of near-surface streamline, $<\Psi>$ topology for angles of attack of $7^o \leq \alpha \leq 17^o$ are presented in Figure 4.14. In the case of angle of attack $\alpha=7°$, positive bifurcation lines, L^+ which represents a line of attachment is developed on both sides of the central axis of the wing. Along the leading edge, negative bifurcation lines, L^- are formed indicating the separation of the flow. On these bifurcation lines, L^- saddle points, S take place. Here, streamlines merge into a single line expending all along the leading edges. These saddle points occur near the trailing edge of the lambda wing. A pair of foci which is designated as F_1 and F_2 begins to appear near the apex of the wing at angle of attack, $\alpha=10^o$. The positive bifurcation line of each vortex, L^+

gets closer to each other because of the enlargement approximation of the foci, F_1 and F_2 under higher angle of attack, α. In addition, a positive and negative bifurcation lines L^+, L^- are evident in all cases of angle of attack. As also Goruney and Rockwell (2009) stated a saddle point, S is always identifiable in the region near the intersection of the leading and trailing edges of the wing. A well-defined pair of foci, F_1 and F_2, which represents the center of an inward swirl pattern of streamlines and three-dimensional separation occurs immediately downstream of the wing apex for attack angle, $\alpha=10^o$. The positive bifurcation lines L^+ on both side of the chord axis get close to each other in the case of $\alpha=13^o$. In the case of angle of attack $\alpha=17°$, center of the foci, F_1 and F_2 moves further downstream comparing to the other cases. It is interesting to note that despite the onset of the large-scale a pair of foci, F_1 and F_2, all of the other critical points, that is, L^+, L^-, and S, are identifiable for angle of attacks $\alpha=13°$ and $17°$.
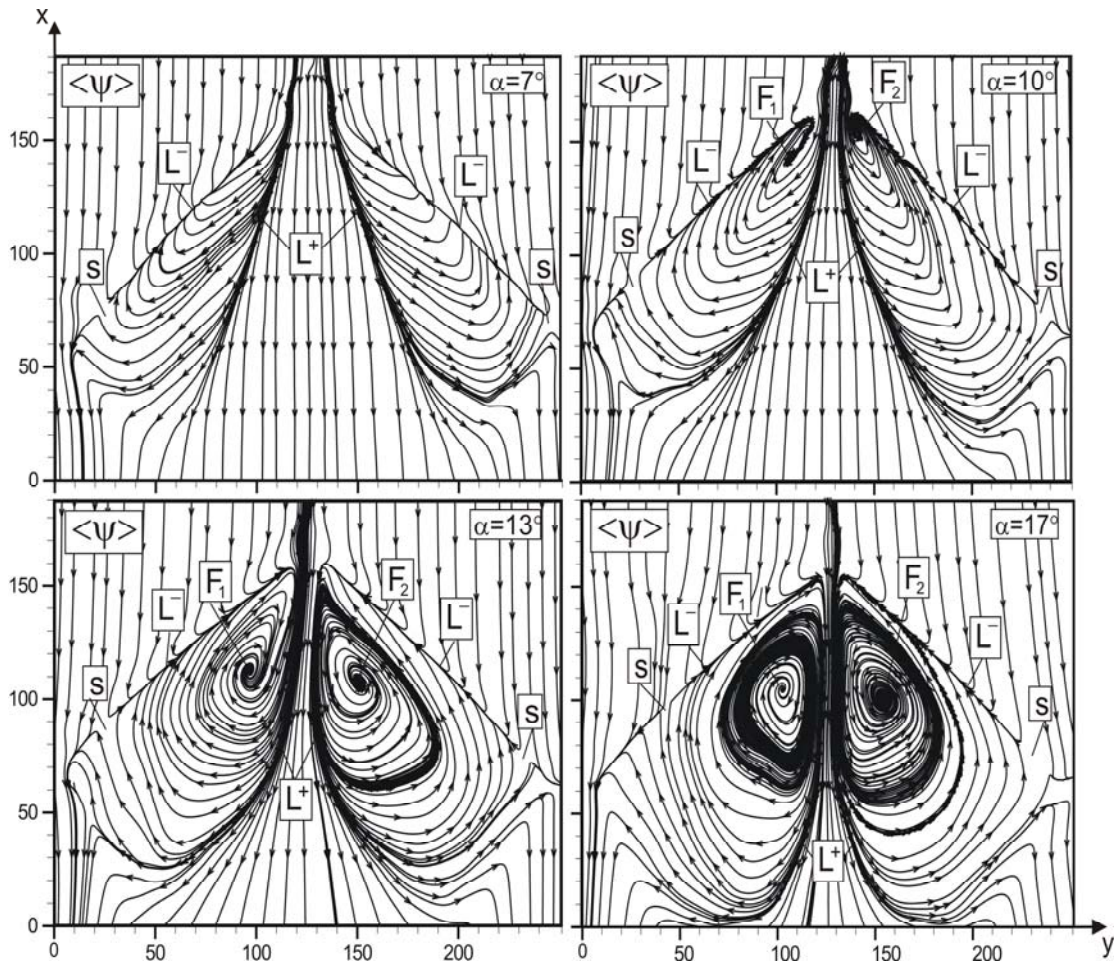
Figure. 4.14. Time-averaged patterns of near-surface streamline, $\langle\Psi\rangle$ for the range of angles of attack $7^o \le \alpha \le 17^o$.

4.2.6. Averaged Vorticity

Figure 4.15 shows the patterns of time-averaged vorticity, $\langle\omega\rangle$ for the range of angles of attack, $7^o \le \alpha \le 17^o$. To be able to make direct comparison between different cases of angles of attack, for the patterns of the time-averaged vorticity, $\langle\omega\rangle$ minimum and incremental values were taken $[\langle\omega\rangle]_{min} =0.4$ s^{-1} and $\Delta[\langle\omega\rangle]$ $=0.7$ s^{-1}, respectively for all cases. Contours represented by the solid and dashed lines, demonstrate positive and negative time-averaged vorticity, $\langle\omega\rangle$. The positive

orientation corresponds to counterclockwise rotation. On the other hand, the negative orientation corresponds to clockwise rotation. There is a pair of vortices which emanates from the leading edge of the lambda wing for all cases of angle of attack, α. Two well-defined clusters of negative and positive time-averaged vorticity, $<\omega>$ are developed along the central axis of the wing designed as A. Central vortices, C are occurred between clusters of negative and positive time-averaged vorticity, $<\omega>$. These central vortices, C are vanished at the angle of attack of $\alpha \geq 10^{o}$. The concentration of vorticity symbolized by E is well defined along starboard side of the wing which has also been detected by Yavuz et al., (2004). When the angle of attack is set to $\alpha=10°$ and further clusters of vorticity A is occupied most part of the wing surface. The magnitude of the vorticity is deteriorated as the angle of attack is increased. They occur due to the three dimensional instability of the shear layer separation from the windward surface of the wing. At angle of attack of $\alpha=10°$, the maximum value of vorticity, $<\omega>$ in the region near the apex is increased relative to the maximum value for the corresponding angle of attack of $\alpha=7°$. In the case of angle of attack of $\alpha=13^{o}$, the maximum value of vorticity, $<\omega>$ decreases comparing to the case of $\alpha=10^{o}$ since vortex breakdown takes place in close region of the apex of the wing. The maximum values of the time-averaged vorticity, $<\omega>$ are 4.6, 5.3, 4.6 and 3.2 for angles of attack, $\alpha =7°$, $10°$, $13°$, and $17°$, respectively as seen in Fig. 15.
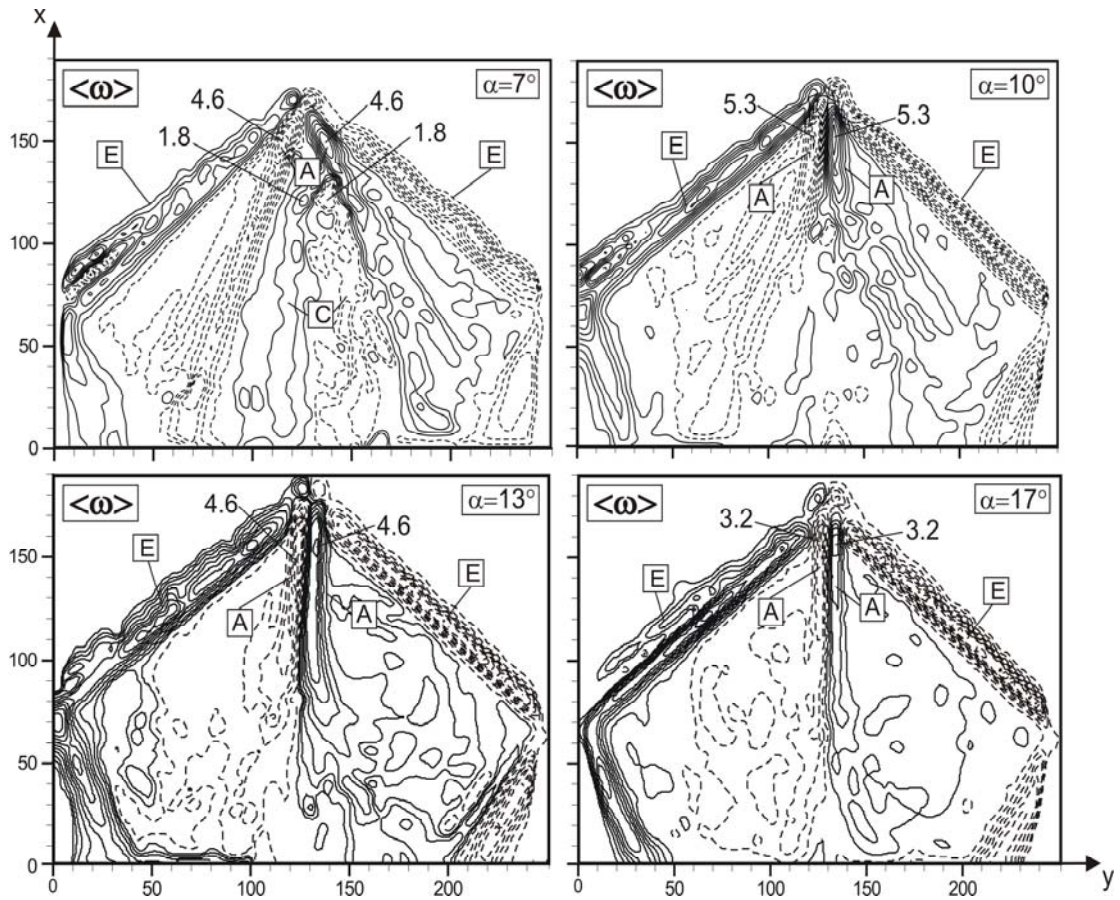
Figure. 4.15. Patterns of time-averaged vorticity, $\langle\omega\rangle$ for angles of attack $7^o \le \alpha \le 17^o$.

4.2.7. Streamline Topology in End-View Plane

Figure 4.16 shows patterns of time-averaged streamlines $\langle\Psi\rangle$ in the cross flow plane at a location x =0.6 C. A well-defined foci, F_1 and F_2 are presented on the cross-flow plane for all angles of attack by patterns of streamlines, $\langle\Psi\rangle$. Below foci, F_1 and F_2, saddle points, S occur on the boundary which is indicated by positive bifurcation lines, L^+. These positive bifurcation lines, L^+ can be recognized from the diverging motion of streamlines toward the single line. This boundary identifies the border between wake flow and free-stream flow regions as also stated by Taylor and Gursul (2004). A nodal point, N is existed at the central axis of the cross-flow plane for all angles of attack. It is known that flow structure is very sensitive to angle of

attack, α. Scale of the foci, F_1 and F_2 extends when the angle of attack, α is increased. This extention from the wing is caused by the extensively separated flow which is evident in the dye visualization shown in Fig. 4.13. On the other hand, saddle points, S which is indicated below foci, F_1 and F_2, are occurred further below from the wing surface at a higher angle of attack, α. Having the angle of attack of α=17°, saddle points, S are not only indicated on the below foci, F_1 and F_2 but also occurred on the bottom of the boundary of the separated flow region. Saddle point, S is shown at the central axis of the cross-flow plane on the close region of the wing for all angles of attack.
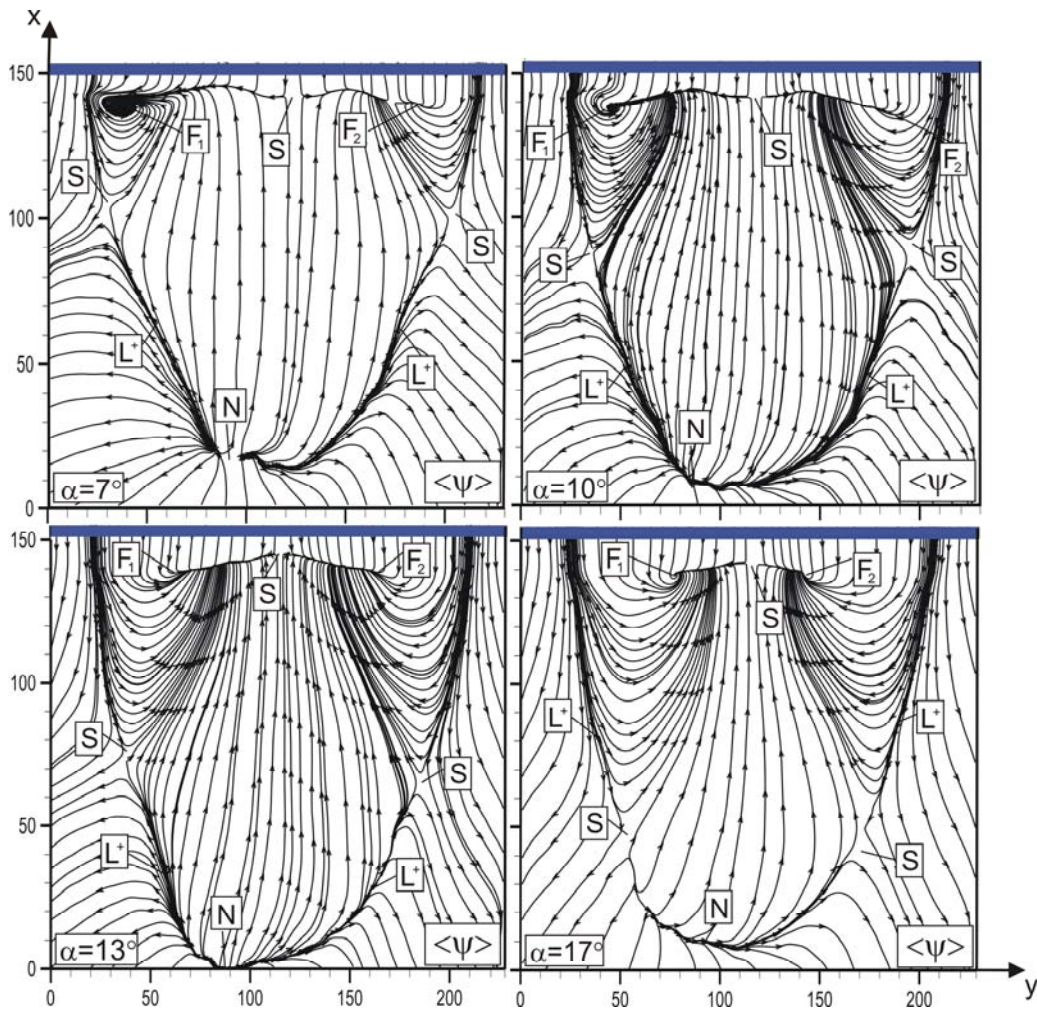
Figure. 4.16. Patterns of time-averaged streamline, <Ψ> topology for angles of attack, α=7°, 10°, 13° and 17°. Laser sheet and measuring plane are located at X/C=0.6.

4.2.8. Patterns of Averaged Vorticity and Fluctuating Velocity in End-View Plane

Alterations of vortex distributions on the lambda wing for Reynolds number of Re=10 000 depending on increasing angle of attack is presented in Figure 4.17. To allow direct comparison, the minimum and incremental values of patterns of time-averaged vorticity $<\omega>$ are maintained the same at all values of α =7°, 10°, 13°, and 17°. For the end-view measurement, it was determined that the major changes of the flow structure occurs just downstream of the vortex breakdown, and therefore the laser sheet is employed at this location such as x/C=0.6. The maximum values of the time-averaged vorticity, $<\omega>$ are 2, 1.6, 1.6 and 1.4 for angles of attack, α =7°, 10°, 13°, and 17°, respectively as seen in Fig. 4.17. It is found that by increasing the angle of attack, α values of the positive and negative time-averaged vorticity, $<\omega>$ are decreased and central points of these vortices move toward the central axis of the wing. It is more meaningful to explain the patterns of time-averaged vorticity $<\omega>$ with corresponding patterns of streamline, $<\Psi>$ topology shown in Fig. 4.16. As Yaniktepe and Rockwell (2004) stated that the location of an extremum of vorticity is not always coincident with the foci of the streamline pattern. In addition, the spatial extent of the large-scale swirl pattern of streamlines is substantially larger than the thickness of the elongated vorticity layer.

Figure 4.18 shows the root-mean-square (rms) of the vortical velocity fluctuation w_{rms} normalized by the freestream velocity U, that is, w_{rms}/U, as well as with the Reynolds-stress correlation $<v'w'>/U^2$, for angles of attack in the range of $7^{o}\leq\alpha\leq17^{o}$. The maximum values of the rms of the vortical velocity fluctuation, w_{rms}/U are 0.04, 0.06, 0.12 and 0.13 and for Reynolds-stress correlation $<v'w'>/U^2$ 0.005, 0.0075, 0.0085 and 0.010 for angles of attack of α =7°, 10°, 13°, and 17°, respectively. As a result, rms velocities, w_{rms}/U and the Reynolds-stress correlations increase due to the formation of the vortex breakdown in the location close to apex under high angle of attack condition. Maxima generally follow the maximum values

of time-averaged vorticity,$<\omega>$. That is, the largest velocity fluctuations occur in the region of maximum vorticity close to the central axis of the wing.
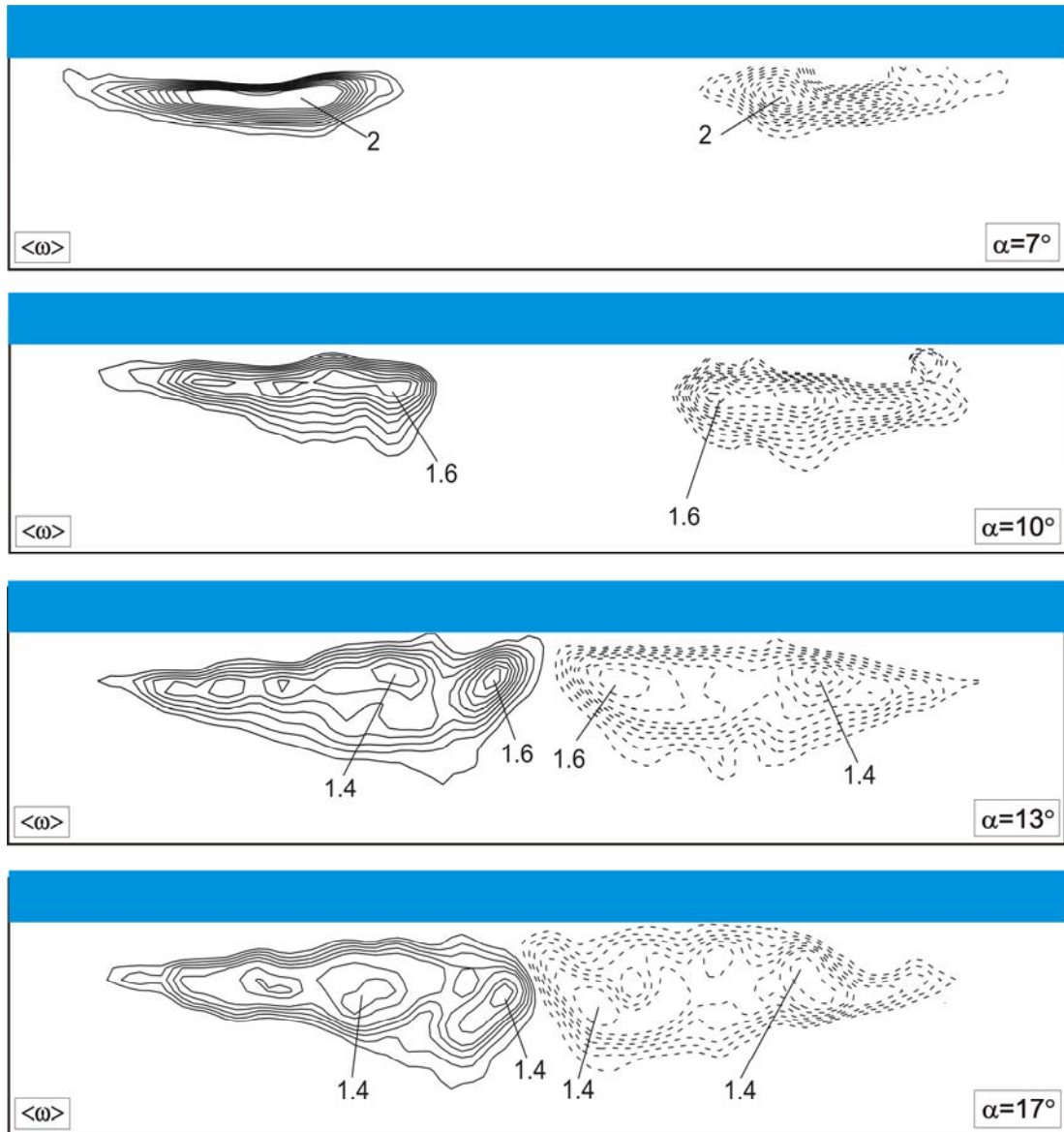
Figure 4.17. Patterns of averaged vorticity $<\omega>$ for angles of attack of α=7°, 10°, 13°, and 17°. Laser sheet is located at x/C = 0.6. For contours of averaged vorticity, minimum and incremental values are $[<\omega>]_{min} = \pm0.1$ s^{-1} and $\Delta[<\omega>] = 0.1$ s^{-1}.
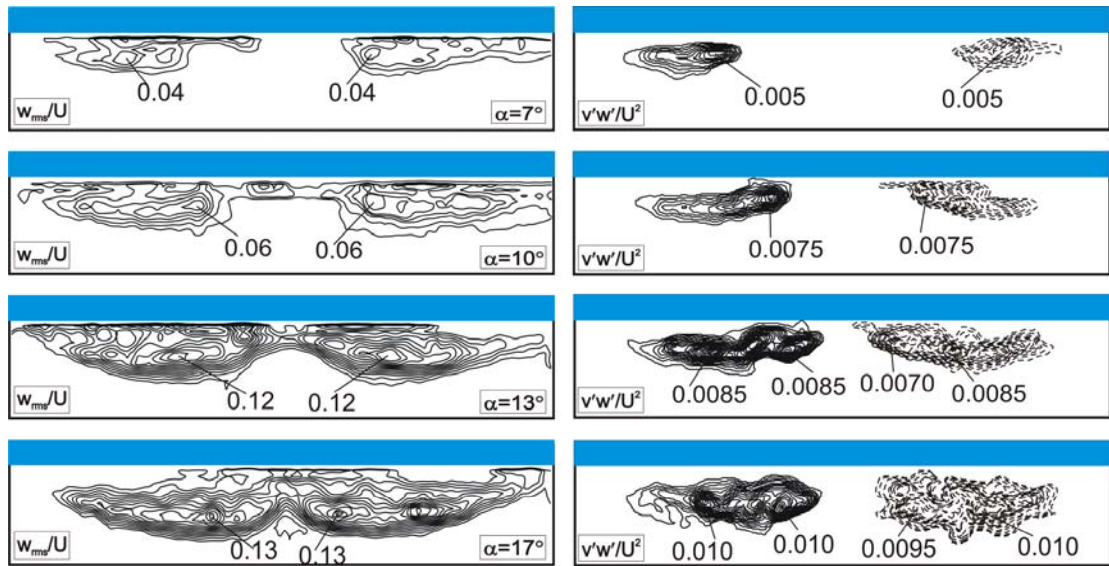
Figure 4.18. Contours of constant vertical (transverse) velocity fluctuation, w_{rms}/U, and Reynolds-stress correlation, $<v'w'>/U^2$. Angles of attack are α=7°, 10°, 13°, and 17°. Laser sheet is located at x/C = 0.6. For contours of constant velocity fluctuation, minimum and incremental values $[w_{rms}/U]_{min}=\mp 0.01$ and $\Delta[w_{rms}/U]=0.01$, $[<v'w'/U^2>]_{min}=\mp 0.0005$ and $\Delta[<v'w'/U^2>]=0.0005$.

4.2.9. Patterns of Fluctuating Velocity

Patterns of the root mean square of streamwise and transverse velocity components, u_{rms}/U and v_{rms}/U and Reynolds stress correlations, $<u'v'>/U^2$ normalized by free-stream velocity, U are presented in figure 4.19. The maximum values of the root mean square of streamwise velocity, u_{rms}/U component are 0.12, 0.14, 0.16 and 0.14 over the wing surface for the range of angle of attack of α=7°, 10°, 13° and 17° and as for the maximum values of the root mean square of transverse velocity, v_{rms}/U component over the wing surface are 0.08, 0.18, 0.18 and 0.14, respectively. The distributions of u_{rms}/U and v_{rms}/U over the wing surface are identical for all angles of attack, α. Consequently, the magnitudes of turbulence characteristics are gradually increased with the angles of attack, α= 7°, 10° and 13°

over the surface of the wing. But, at the highest angle of attack, $\alpha= 17°$, the maximum values of these flow characteristics are lower comparing to the case of $\alpha= 13°$.

Above referred Reynolds-stress values $\langle u'v' \rangle/U^2$ have relationship with the standard components of root-mean-square (rms) velocity fluctuations that are streamwise and transverse velocity components u_{rms}/U and v_{rms}/U. If the standard components of root-mean-square (rms) velocity fluctuation increase, Reynolds-stress values also increase. Although images were taken in close proximity to the surface of the wing, the structure of vortex breakdown has a considerable effect in the wake region. Reynolds-stress correlations $\langle u'v' \rangle/U^2$ as a set of extreme for all angles of attack appear on the identical locations. The concentration of Reynolds-stress distributions $\langle u'v' \rangle/U^2$ occupy a wide region over the wing surface in the case of higher angle of attack, α such as $\alpha=13°$ and $17°$. The maximum values of Reynolds-stress correlations, $\langle u'v' \rangle/U^2$ surface of the wing are 0.0035, 0.008, 0.012 and 0.010 for angles of attack, $\alpha=7°$, $10°$, $13°$ and $17°$, respectively. That is Reynolds-stress correlations, $\langle u'v' \rangle/U^2$ are gradually increased while the angle of attack, α is altered from $7°$ to $13°$. However, at the highest angle of attack $\alpha =17°$, the maximum value of Reynolds stress correlation is lower than that of the case of $\alpha =13°$.
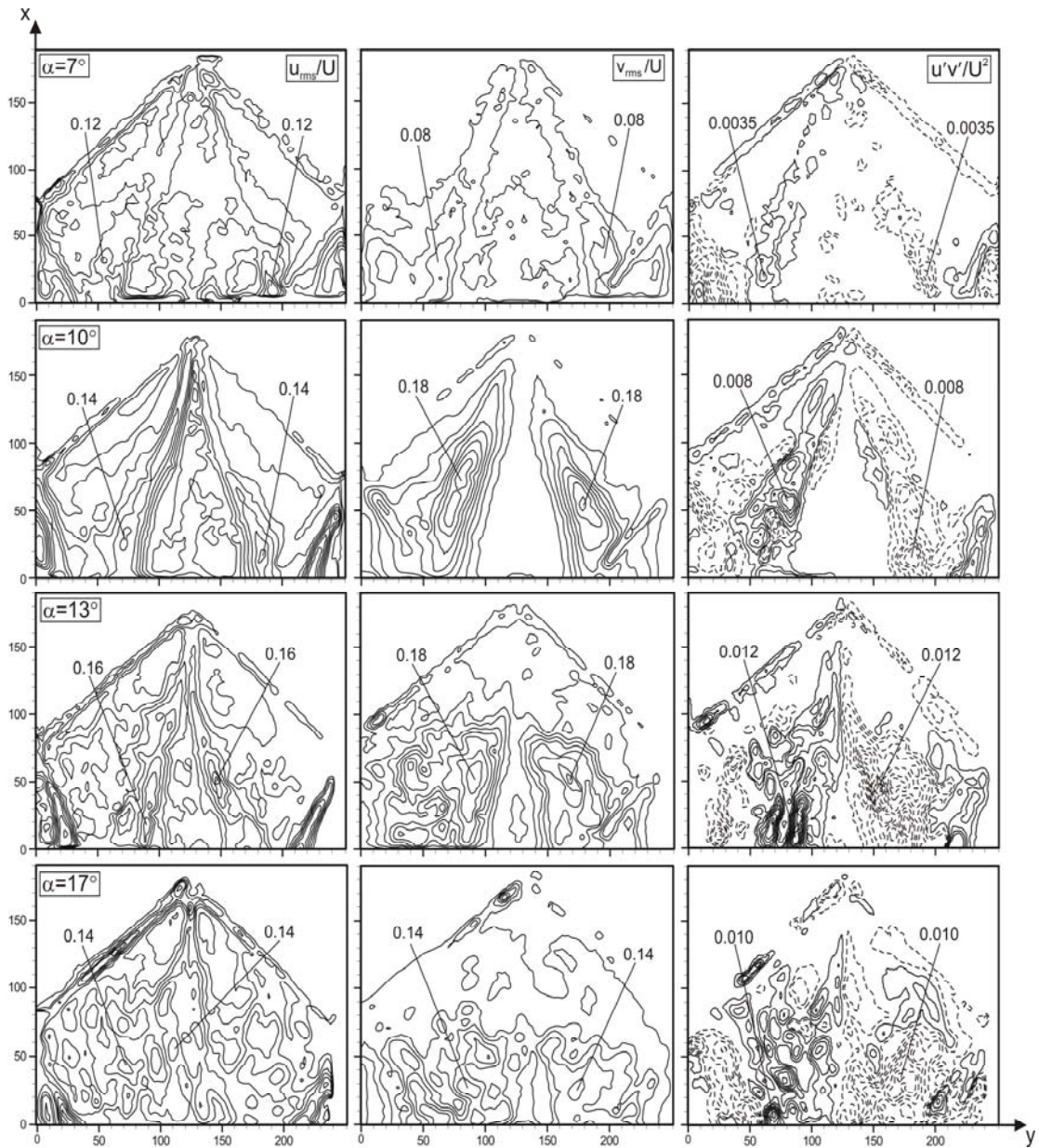
Figure 4.19. Consequence of angle of attack on patterns of rms of the streamwise, transverse velocity fluctuation and Reynolds stress correlation, respectively, u_{rms}/U, v_{rms}/U and $<u'v'>/U^2$. For contours of constant u_{rms}/U and v_{rms}/U, $[u_{rms}/U]_{min}=0.02$, and $\Delta[u_{rms}/U]=0.02$, $[v_{rms}/U]_{min}=0.02$, and $\Delta[v_{rms}/U]=0.02$. For contours of constant Reynolds-stress correlation, $[<u'v'>/U^2]_{min} = \pm\ 0.0005$, and $\Delta[<u'v'>/U^2] =0.0015$.

4.2.10. Patterns of Time-Averaged Velocity Components

The first column of Figure 4.20 shows the consequence of all angles of attack on the contours of streamwise velocity component, $\langle u \rangle/U$. The second column of the same figure shows the patterns of dimensionless transverse velocity component, $\langle v \rangle/U$ and the third column presents vertical velocity component, $\langle w \rangle/U$. Contours represented by the solid and dashed lines, demonstrate positive and negative streamwise, transverse and vertical velocity components, $\langle u \rangle/U$, $\langle v \rangle/U$ and $\langle w \rangle/U$, respectively. The minimum and incremental values of contours of dimensionless streamwise velocity, $\langle u \rangle/U$, transverse velocity, $\langle v \rangle/U$ and vertical velocity, $\langle w \rangle/U$ for all angles of attack were kept constant for better comparison between time-averaged velocity components.

The maximum values of positive streamwise velocity component, $\langle u \rangle/U$ are 0.95, 0.85, 0.75 and 0.40 and, magnitude of the maximum values of negative streamwise velocity component, $\langle u \rangle/U$ are 0.05, 0.15, 0.20 and 0.30 for angles of attack of $\alpha=7°$, 10°, 13° and 17°, respectively. As seen in the first image of the contours of streamwise time-averaged velocity component, $\langle u \rangle/U$, a negative velocity distributions take place on both side edges of the wing. While the maximum value of positive streamwise velocity component, $\langle u \rangle/U$ in the near surface of the wing decreases but, the negative streamwise velocity component, $\langle u \rangle/U$ increases as the angle of attack, α of the wing increases. When the angle of attack is increased, the vortex breakdown that is indicated on the both side of the wing chord axis occurs closer to the apex as seen from the dye visualization images presented in figure 4.12. So, it is well seen that this substantial alteration of the onset of vortex breakdown seems to have remarkable influence on the patterns of $\langle u \rangle/U$, $\langle v \rangle/U$ and $\langle w \rangle/U$ even in the near surface of the wing.

In the second column of Figure 4.20, there are two well-defined clusters of main positive and negative contours of transverse velocity component, $\langle v \rangle/U$ sembolized as A and placed on both sides of the lambda wing chord axis in the case of $\alpha=7°$ for transverse velocity component, $\langle v \rangle/U$. Also, a pair of clusters symbolized as B occurs along the side edges of the wing for angle of attack of $\alpha=7°$. On the other

hand, three different pairs of clusters of transverse velocity, $<v>/U$ components were developed over the wing surface in the cases of $α=10°$, $13°$ and $17°$. The first and second pair that are symbolized as A and B, it is defined above. The third pair that is symbolized as C takes place between clusters A and B. The transverse velocity patterns A and B on the left hand side of wing chord axis are positive, and the transverse velocity patterns A and B on the right hand side of the wing chord axis are negative. For the C, vice versa condition is valid. The maximum values of positive and negative transverse velocity components, $<v>/U$ are 0.35, 0.30, 0.30 and 0.25 for angles of attack of $α=7°$, $10°$, $13°$ and $17°$, respectively. The maximum value of transverse velocity component, $<v>/U$ decreases with higher angles of attack comparing to the streamwise velocity component, $<u>/U$.

In the third column of Figure 4.20, it is seen that, value of the vertical velocity components, $<w>/U$ is smaller than those of the streamwise and transverse velocity components, $<u>/U$ and $<v>/U$. The maximum values of positive and negative vertical velocity components, $<w>/U$ are shown as 0.15 over the surface of the wing for all the angles of attack, $α$.

Finally, it can be concluded that the magnitude of velocity components are lower over the wing surface at angle of attack of $α=17°$ because the separated flow covers whole wing surface.
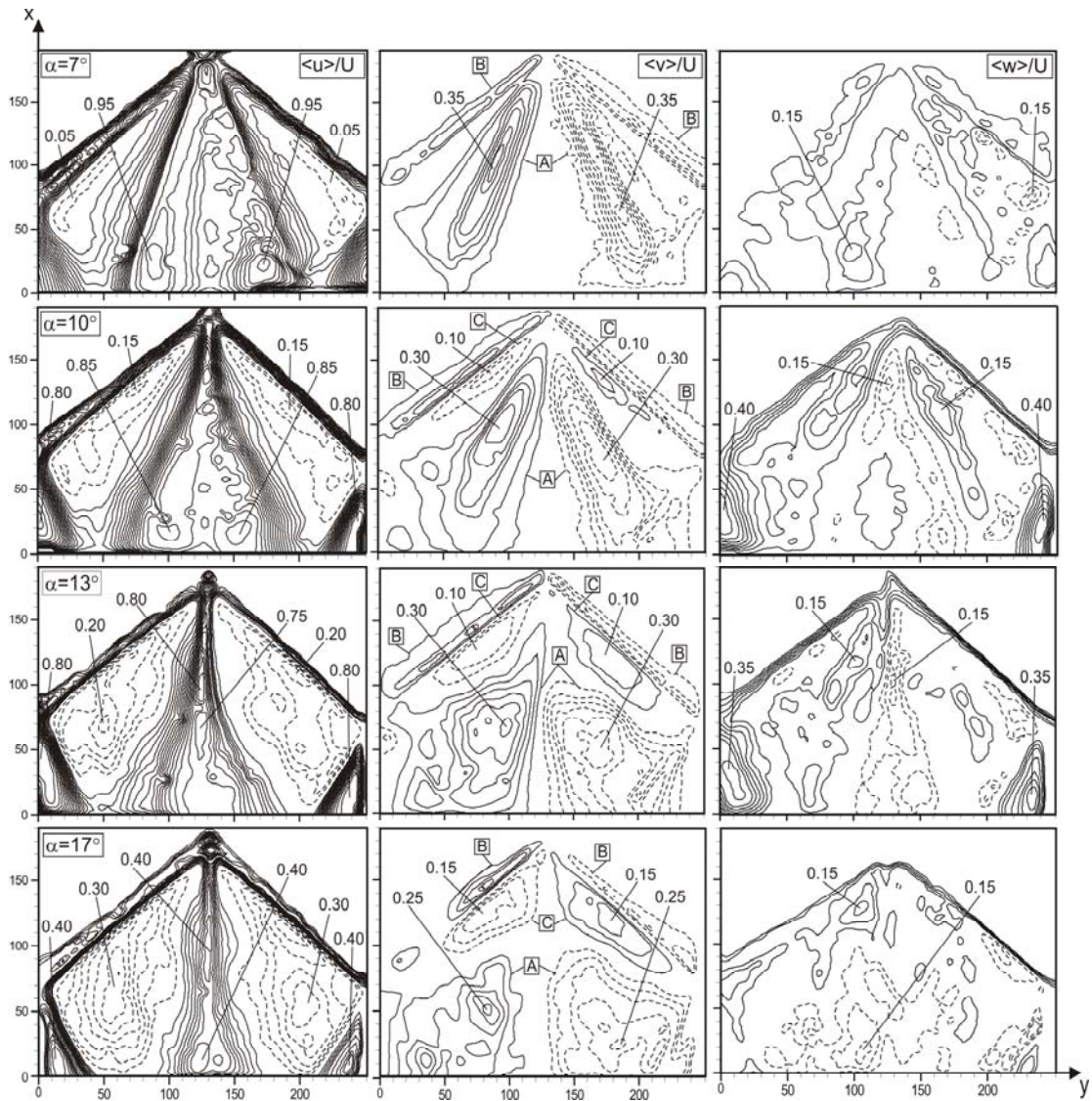
Figure 4.20. Patterns of time-averaged components of streamwise, [<u>/U], transverse, [<v>/U] and vertical [<w>/U] velocity. Minimum and incremental values are [<u>/U]$_{min}$ =0.05, [<v>/U]$_{min}$ =0.05, [<w>/U]$_{min}$ =0.05 and Δ[<u>/U] =0.05, Δ[<v>/U] =0.05, Δ[<w>/U] =0.05.

4.2.11. The Normalized Components of the Reynolds Normal Stresses and Turbulent Kinetic Energy (TKE)

The analysis of the dimensionless fluctuating velocity component indicates that the maximum of turbulence level occur along the shear layer. Figure 4.21 indicates streamwise, transverse and vertical Reynolds normal stress correlations, $<u'u'>/U^2,$

90

$<v\acute{}v\acute{}>/U^2$ and $<w\acute{}w\acute{}>/U^2$ to reveal its effect on turbulent kinetic energy under the variation of the angles of attack in the range of $7° ≤ α ≤ 17°$. The minimum and incremental values of contours for streamwise and transverse Reynolds normal stresses, $<u\acute{}u\acute{}>/U^2$, $<v\acute{}v\acute{}>/U^2$ are the same and equal to 0.002 and 0.002, respectively. Also the minimum and incremental values of contours for vertical Reynolds normal stresses, $<w\acute{}w\acute{}>/U^2$ are 0.002 and 0.005, respectively. Figure 4.21 shows that the maximum values of transverse, streamwise and vertical Reynolds normal stresses, $<u\acute{}u\acute{}>/U^2$, $<v\acute{}v\acute{}>/U^2$, $<w\acute{}w\acute{}>/U^2$ are gradually increased with angles of attack of α=7°, 10° and 13° over the surface of the wing. At the highest angle of attack $α$ =17°, the patterns of Reynolds stress correlations have a fundamentally different form and cover mostly broader areas over the surface of the wing comparing to other cases. For the higher values than angle of attack of α=13°, vortex breakdown occurs over the wing apex. As observed from the dye visualization, vortex breakdown flow structure spreads over the entire wing surface. This case decreases the value of fluctuating velocity. The maximum values of $<u\acute{}u\acute{}>/U^2$, $<v\acute{}v\acute{}>/U^2$ and $<w\acute{}w\acute{}>/U^2$ for angle of attack of α=17° are lower comparing to the cases of $α$ =10° and 13°. The maximum values of normalized streamwise Reynolds normal stress, $<u\acute{}u\acute{}>/U^2$ are 0.020, 0.026, 0.028 and 0.024 and for normalized transverse Reynolds normal stress, $<v\acute{}v\acute{}>/U^2$ the values are 0.014, 0.024, 0.026 and 0.022 and normalized vertical Reynolds normal stress, $<w\acute{}w\acute{}>/U^2$ are 0.022, 0.032, 0.037 and 0.027 for the angles of attack of α=7°, 10°, 13° and 17°, respectively.

Results of the turbulent kinetic energy, TKE for all angle of attack are shown in Figure 4.22. For minimum and incremental values of the contours of time-averaged turbulent kinetic energy, TKE was taken as $[<TKE>]_{min}$=0.005 and $\Delta[<TKE>]$=0.009, respectively. The maximum values of TKE for angles of attack of α=7°, 10°, 13° and 17° are 0.018, 0.026, 0.029 and 0.023, respectively. Turbulent kinetic energy, TKE is related to the normalized components of the Reynolds normal stresses, $<u\acute{}u\acute{}>/U^2$, $<v\acute{}v\acute{}>/U^2$ and $<w\acute{}w\acute{}>/U^2$. TKE increases gradually over the wing surface when the angles of attack is increased from α=7° to 13°. Here,

according to the vortex breakdown location which moves further upstream close to the leading edge of the wing, high rate of fluctuations in velocity components are detected. However, as seen in the case of α=17°, TKE values are lower than those values obtained in the cases of angles of attack of α =10° and 13°. In Figure 4.21, examining the maximum values of the normalized components of Reynolds normal stresses, $<u'u'>/U^2$, $<v'v'>/U^2$ and $<w'w'>/U^2$, it is seen that, the maximum value of the vertical Reynolds normal stresses, $<w'w'>/U^2$ is higher than the streamwise and transverse Reynolds normal stress, $<u'u'>/U^2$ and $<v'v'>/U^2$. Contribution of vertical Reynolds normal stress, $<w'w'>/U^2$ on the formation of TKE is higher compared to effects of the streamwise and transverse Reynolds normal stress, $<u'u'>/U^2$ and $<v'v'>/U^2$.
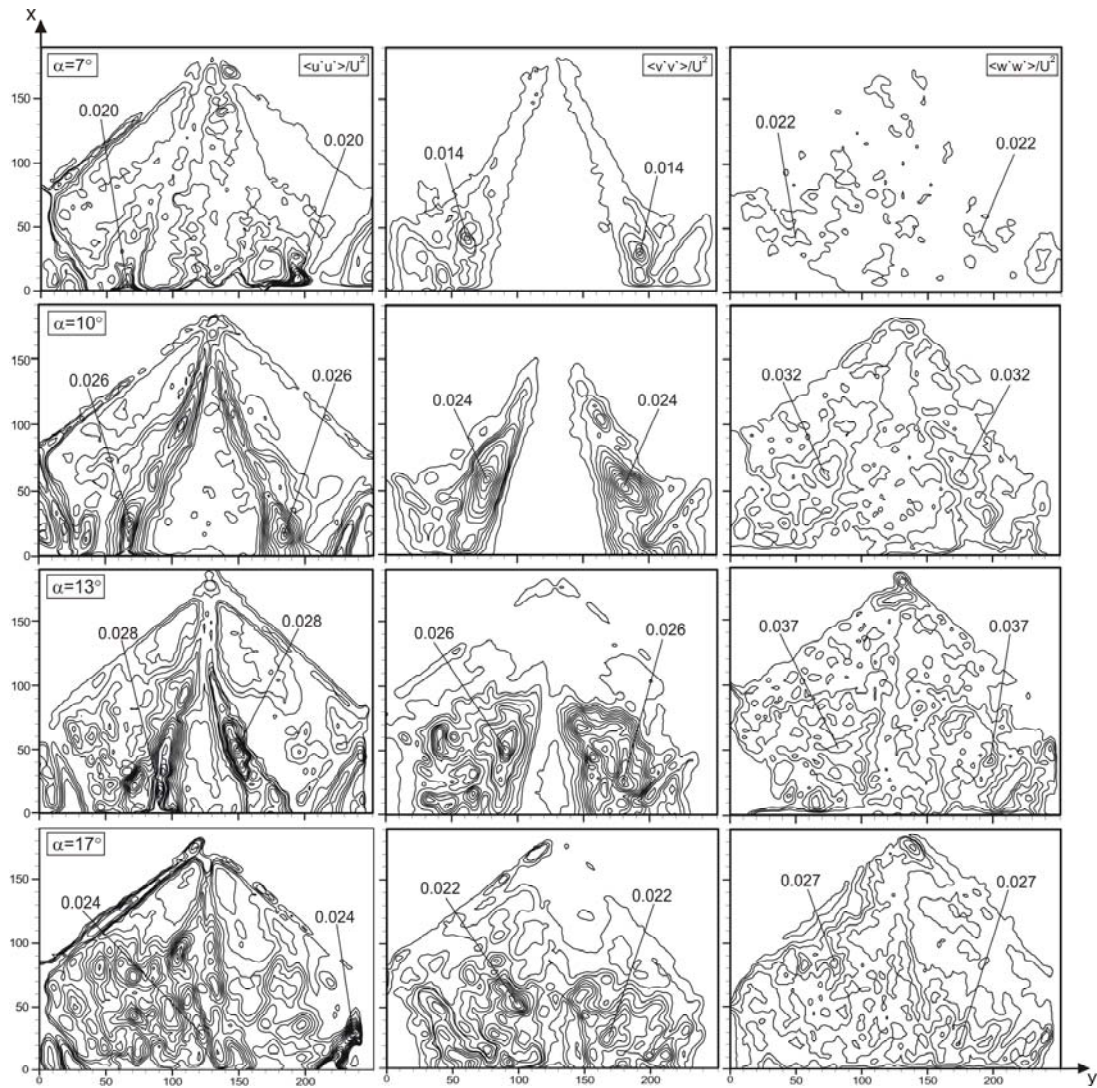
Figure 4.21. The contours of time-averaged Reynolds normal stress components for the angle of attack of $7° \leq \alpha \leq 17°$.
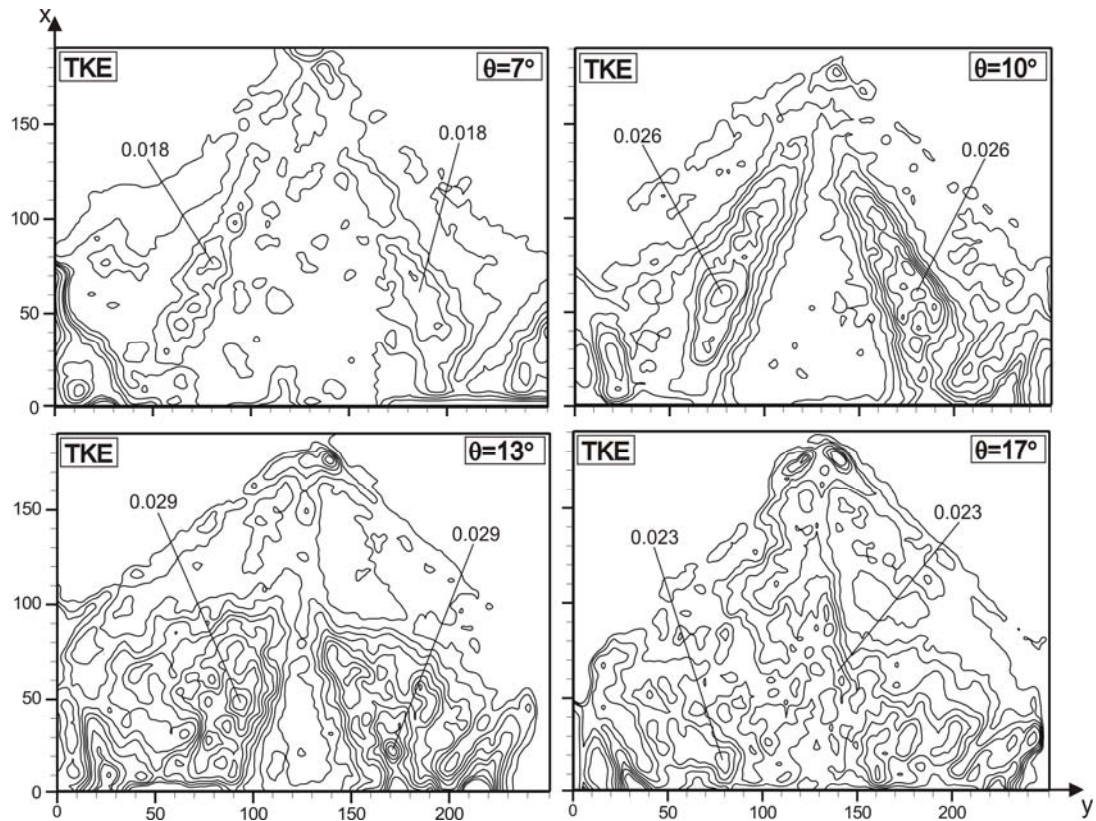
Figure 4.22. The contours of time-averaged turbulent kinetic energy (TKE) for the angle of attack of $7°≤α≤17^{o}$.

4.2.12. Velocity Vectors Distribution

The pattern of time-averaged distribution of velocity vectors, <V> over the lambda wing for the angle of attack of $α=10^{o}$ is presented in Figure 4.23. In this figure, dimensionless chord distances, x/C is presented as x/C=0.4, 0.6, 0.8 and 1.

At these dimensionless chord distances, x/C, the variation of velocity vectors along y axis is presented in Figure 4.24. Horizontal axis of the diagram shows dimensionless y/S value that evaluated by dividing the y axis values to the span, S. On the other hand, vertical axis of the figure shows dimensionless total velocity magnitude, U. It is understood that magnitude of the velocity is very low close to the wing edges and they increase by approaching the wing chord axis. Further away from the wing apex, i.e. at x/C=0.8 and 1, the magnitude of velocity increases in the outer region close to the side edges. Moreover, by drawing away from the wing apex,

94

as dimensionless chord distances, x/C is increased, for a certain angle of attack, the magnitude of velocity along the wing chord axis attenuate. Especially for α=17° and dimensionless chord distance of x/C=0.4, the level of dimensionless velocity vector along the chord axis is nearly 0.8, but by increasing the dimensionless chord length from x/C=0.6 to 1, i.e. moving away from wing apex, the magnitude of velocity gradually attenuates. For x/C=1, this value decreases to 0.39. The magnitude of velocity along the wing chord axis is lower with respect to the velocity magnitude in the close region to the chord axis. But, at a high angle of attacks, vortices formed on either side of the wing chord axis approach to the chord axis, and as a result of this, the interaction area of the vortex increases. Hence, at a low angle of attacks, for example α=7°, velocity magnitude on the wing chord axis is lower compared with the other angle of attack values.
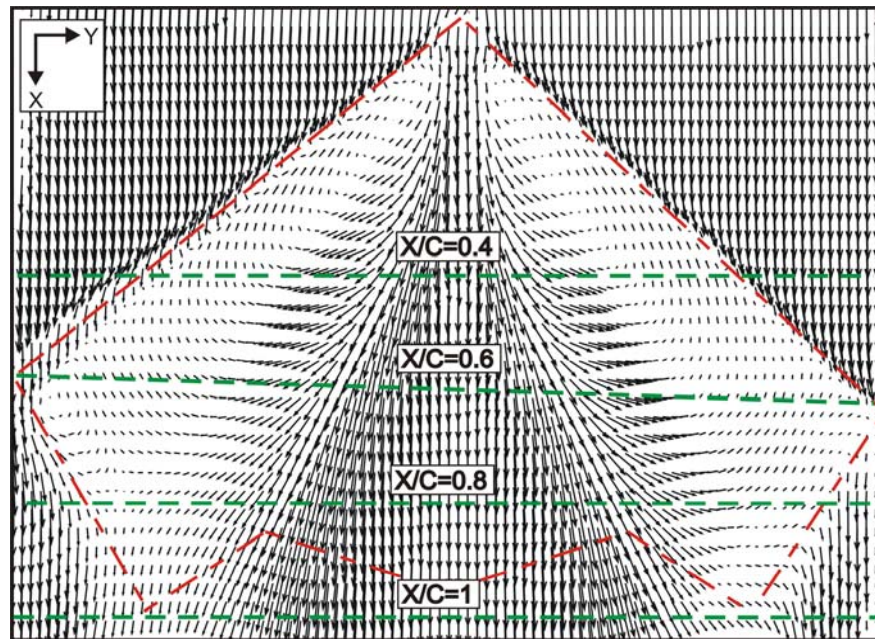
Figure 4.23. Pattern of time-averaged distribution of velocity vectors,<V> for angle of attack α=10°.
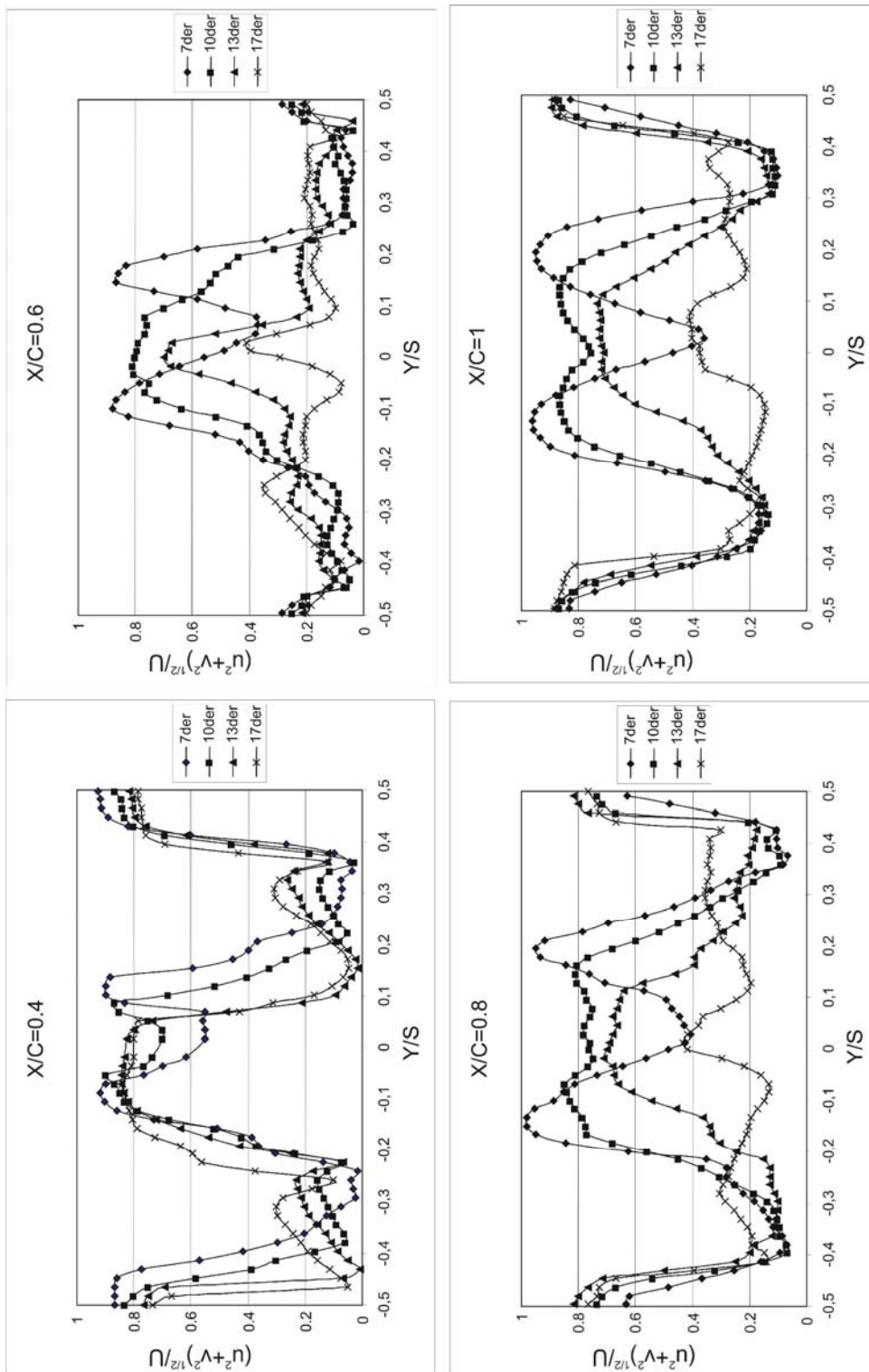
Figure 4.24. Diagram of velocity vectors,<V> at the ranges of Y/C=0.4, 0.6, 0.8 and 1 for all angles of attack.

4.3. Control of Vortex Breakdown over the Nonslender Lambda Wing

4.3.1. Introduction

Different planforms demand high performance at high angle of attack when undergoing dynamic motions. Previous studies of the UCAV planform considered only the flow structure on stationary planforms at defined angles of attack. The dynamics effects of a perturbed or pitching motion on the flow structure adjacent to the surface of the planform have been investigated in this section.

Relatively few investigations have addressed the flow structures on a delta wing under dynamics conditions. Among these, Yaniktepe and Rockwell (2004) and Ozgoren et al. (2002) studied the dynamics of vortices on a perturbed delta wing.

4.3.2. Objective of the Present Work

The overall aim of this investigation is to present controlling of flow structure on the surface of the lambda wing by leading-edge perturbations. In doing so, a technique of particle image velocimetry PIV is used to characterize the flow patterns in the near-surface region of the wing.

4.3.3. Experimental Arrangements and Instrumentations

Average free-stream velocity in the plan-view planes is U_{av} = 59.5 mm/sec which correspond to Reynolds numbers Re_c = 10 000 based on the chord (C) and Re_h =61 285 based on the open-channel hydraulic diameter for all experiments. The chord (C) of the lambda wing had a length of 168 mm. The sweep angle of the wing was specified as Λ = 40°. In addition, the wing had a thickness (t) of 3 mm, and was beveled on the windward side at an angle of 45°. The wing was subjected to small amplitude controlled perturbations of the form $\alpha(t)=\overline{\alpha} +\Delta\alpha\sin\omega_e t$, in which $\omega_e=2\pi f_e$. The period of excitation $T_e=2\pi/\omega_e$ was varied over the interval $0.5 \leq T_e \leq 1$ s. The averaged images for the perturbed wing are based on the instantaneous images at the

mean angle of attack $\overline{\alpha}$ =10°; the angle of attack of the corresponding stationary wing was α =10°. The amplitude of the wing perturbation was $\Delta\alpha$ =1°. The flow is also controlled by giving periodic perturbation motion to the wing. During the periodic perturbation motion, the flow is controlled along 3 seconds by giving perturbation motion to the wing and the wing remained fixed until there is no control effect of the flow (along the time 12 seconds that was defined by dye experiments) and then again perturbation motion is given to the wing. The amplitude of perturbation angle of attack for periodic perturbation is $\Delta\alpha$ =1° and periodic perturbation period is T_e=1s.

4.3.4. Comparison of Patterns of Surface Topology and Flow Structure for Stationary of the Wing

Figure 4.25 compares different types of surface patterns for stationary wing. The pattern of time-averaged velocity vector <V> shown in the top-left-hand side image indicates that the symmetrical flow topology occupies the whole wing surface, in the case of attack angle of α=10°. This image indicates that, the velocity vectors have large amplitude in the both side of central portion of the lambda wing. However, farther outboard from the central axis of the wing, the magnitude of velocity becomes small.

In the time-averaged vorticity, <ω> shown at the top right of Figure 4.25, minimum and incremental values were taken as $[<\omega>]_{min}$ =0.4 s^{-1} and $\Delta[<\omega>]$ =0.7 s^{-1}. Two well-defined clusters of negative and positive the time-averaged vorticity, <ω> are developed along the central axis of the wing designated as A. The concentration of vorticity symbolized by E is well defined along starboard side of the wing which has also been detected by (Yavuz et al., 2004).

Patterns of the root mean square of streamwise and transverse velocity components, u_{rms}/U and v_{rms}/U and Reynolds stress correlations, $<u'v'>/U^2$ normalized by free-stream velocity, U are presented in Figure 4.25. For contours of constant u_{rms}/U and v_{rms}/U, $[u_{rms}/U]_{min}$=0.02, and $\Delta[u_{rms}/U]$=0.02, $[v_{rms}/U]_{min}$=0.02, and $\Delta[v_{rms}/U]$=0.02. On the other hand, for contours of constant Reynolds-stress

correlation, $[<u'v'>/U^2]_{min}$ =0.0005, and $\Delta[<u'v'>/U^2]$ =0.0015. Reynolds-stress values $<u'v'>/U^2$ have relationship with the standard components of root-mean-square velocity fluctuation that are streamwise and transverse velocity components u_{rms}/U and v_{rms}/U. If the standard components of root-mean-square velocity fluctuation increase, Reynolds-stress values also increase. It is seen that, streamwise velocity components u_{rms}/U are smaller than transverse velocity components v_{rms}/U. So, effect of transverse velocity components v_{rms}/U on the formation of Reynolds stress correlations, $<u'v'>/U^2$ are higher than streamwise velocity components u_{rms}/U.

The result of dye visualization experiments shows that this elongated separated flow region can take on an interesting dual vortex structure. At upstream locations near the apex, the long, and thin shear layer that emanates from the leading edge of the lambda wing terminates the formation of the primary vortex. Further downstream a secondary vortex, with vorticity of the same sign as the primary vortex, emerges in the separated shear layer outboard of the primary vortex creating a dual vortex structure. This secondary vortex, which is slightly weaker and smaller than the primary vortex, arises from the interaction of the secondary flow with the primary shear layer.
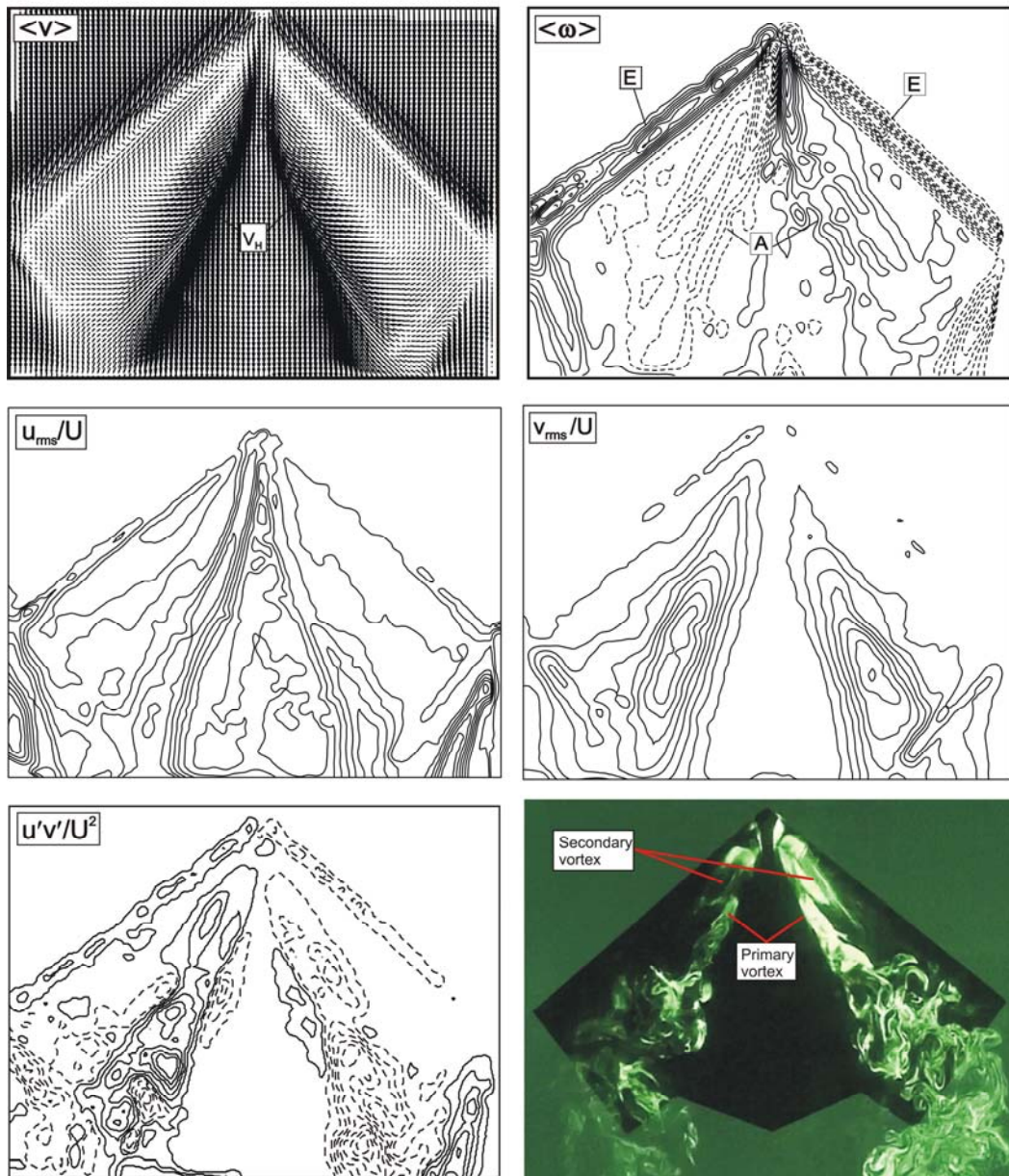
Figure 4.25. Comparison of patterns of wing surface topology for angle of attack of α=10°.

4.3.5. Effect of Wing Perturbations on Flow Structure

For the lambda wing model, in the near-surface plane, dye experiment results of flow structure along central axis of leading edge vortices are given in Figure 4.26. The values of mean and perturbation angles of attack are $\bar{\alpha}$ =10° and $\Delta\alpha$ =1°, respectively. The period of excitation, denoted on Figure 4.26 are T_e =0.5 and 1 s. The amplitude of attack angle, $\Delta\alpha$ =1° was sellected to determine whether such a small displacement amplitude could significantly affect the flow structure or not.

At the top the left of image, vortex pairs that are formed on the wing surface are seen at stationary wing for α=10°. As seen in figure, vortex breakdown occurs nearly at the x/C=0.4. Examining the cinema recordings of dye experiments, it is seen that vortex breakdowns are not formed at the same point every time. In another words, vortex breakdowns on both side of the wing chord axis occur at the same time but, while one moves towards to wing apex, the other one moves in opposite direction. Namely, an unsteady condition is valid.

At the top right of image, the behaviors of leading edge vortices are investigated in the case of continuous perturbation of the wing given by a servo motor with the perturbation period of T_e=0.5 s and amplitude of perturbation angle of attack $\Delta\alpha$=1°. As seen in the image, locations of vortex breakdown get closer to the wing apex compared to the case of the stationary wing and averaged location of vortex breakdown occurs at the point of x/C=0.4.

At the bottom left of Figure 4.26 shows the pattern of dye experiments under the continuous perturbation condition with period of T_e=1 s. Vortex breakdown occurs nearly at x/C=0.2 in this case. Vortex breakdowns away from to wing apex compared to the perturbation period T_e=0.5 s.

Last image of the second column of Figure 4.26 presents leading edge vortex formations and vortex breakdowns which are investigated under the periodic perturbation condition. In the case of periodic perturbation, intervals of oscillations are 3 seconds, and the wing was kept stationary for the period of 12 seconds, amplitude of perturbation angle of attack was $\Delta\alpha$=1° and periodic perturbation period was T_e=1s. For this condition, it was seen that locations of vortex breakdown move

close to the trailing edge of the wing. In another words, vortex breakdowns are delayed compared with other cases.
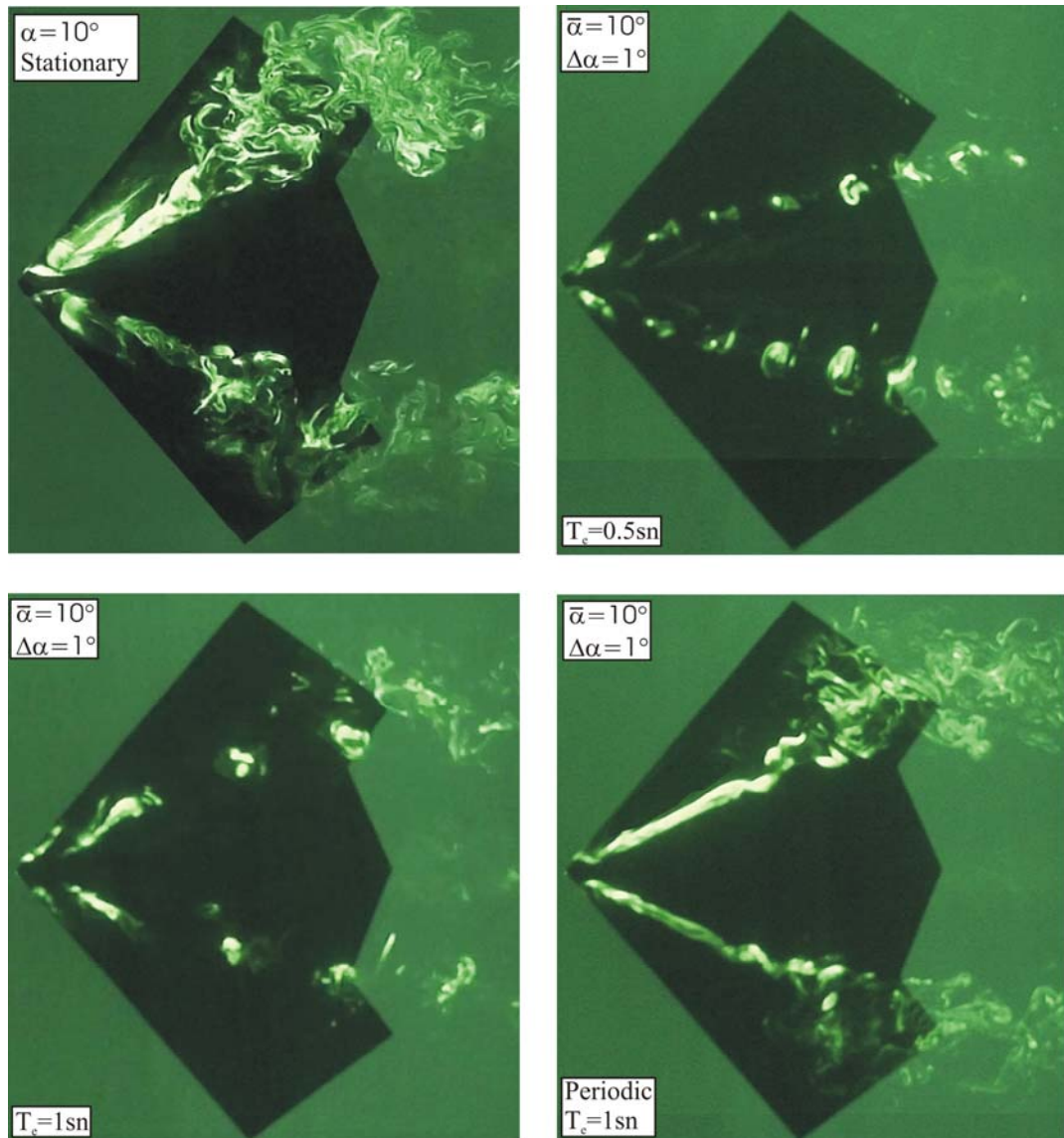
Figure 4.26. Dye visualizations of the lambda wing for stationary, continuous and periodic perturbation conditions at perturbation period of T_e =0.5 and 1s and amplitude $\Delta\alpha$ =1°.
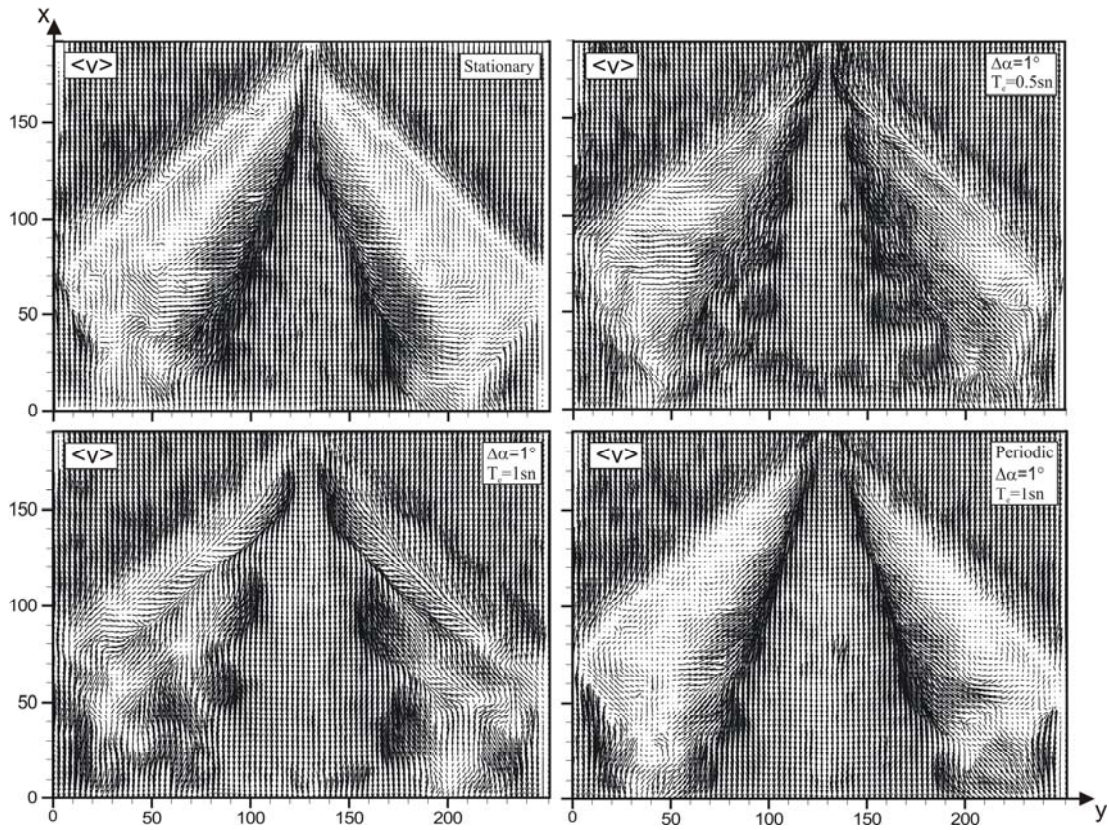
Figure 4.27. Patterns of instantaneous velocity vectors, V for mean angle of attack, $\overline{\alpha} = 10^o$.

The behavior of the near-surface flow structure and instantaneous velocity vectors, V presented Figure 4.27 under the effect of perturbation when the mean angle of attack is $\overline{\alpha} = 10°$ and amplitude of perturbation angle of attack as $\Delta\alpha = 1^o$, having periods as $T_e = 0.5$ s and 1s. As seen in figure, locations of vortex breakdown moves towards to the wing apex. Examining all instantaneous images, the flow structure is symmetrical. Vortex breakdown is occurred after a certain distance from the wing apex as seen in the instantaneous images. Instantaneous velocity vectors are presented in the last image of column Figure 4.27 when the lambda wing is perturbed periodically. As seen from dye visualization experiments, the location of vortex breakdown moves further down stream when the wing is under effect of periodic perturbation with the period of $T_e = 1$ s and amplitude of $\Delta\alpha = 1^o$ for 3 seconds. As seen as the perturbation is stopped the location of vortex breakdown returns to its initial

location after 12 seconds. Examining all instantaneous velocity vectors, V it seen that vortex breakdown is occurred a way from apex of the wing compared with stationary wing.

Figure 4.28 shows the patterns of time-averaged vorticity, $<\omega>$ for stationary, continuous perturbation and periodic perturbation cases. To be able to make direct comparison between different cases, the patterns of the time-averaged vorticity, $<\omega>$ minimum and incremental values were taken $[<\omega>]_{min}=0.4$ s^{-1} and $\Delta[<\omega>]=0.7$ s^{-1}, respectively for all cases. Contours represented by the solid and dashed lines, demonstrate positive and negative time-averaged vorticity, $<\omega>$ respectively. The positive orientation corresponds to counterclockwise rotation. On the other hand, the negative orientation corresponds to clockwise rotation. Two well-defined clusters of negative and positive time-averaged vorticity, $<\omega>$ are developed along the central axis of the wing represented as A for all conditions. When the perturbation period is set to $T_e=0.5$ s and further main clusters of vorticity A are occupied less part of the wing surface. The concentration of vorticity symbolized by E is well defined along starboard side of the wing which was also detected by Yavuz et al., (2004). In the case of perturbation and periodic perturbation period of $T_e=1$ s, central vortices, C are occurred between clusters of negative and positive time-averaged vorticity, $<\omega>$. Vorticity levels for the perturbed wing are generally lower than those of stationary wing. The maximum values of the contours of time-averaged vorticity, $<\omega>$ for stationary, continuous perturbation of $T_e=0.5$ and 1 s and periodic perturbation of $T_e=1$ s conditions are 5.3, 3.9, 3.2 and 2.5, respectively. In the case of periodic perturbation period of $T_e=1$ s, the maximum value of vorticity, $<\omega>$ in the near region of the wing is lower than the maximum values for other conditions due to late occurrence of vortex breakdown from apex of the wing.
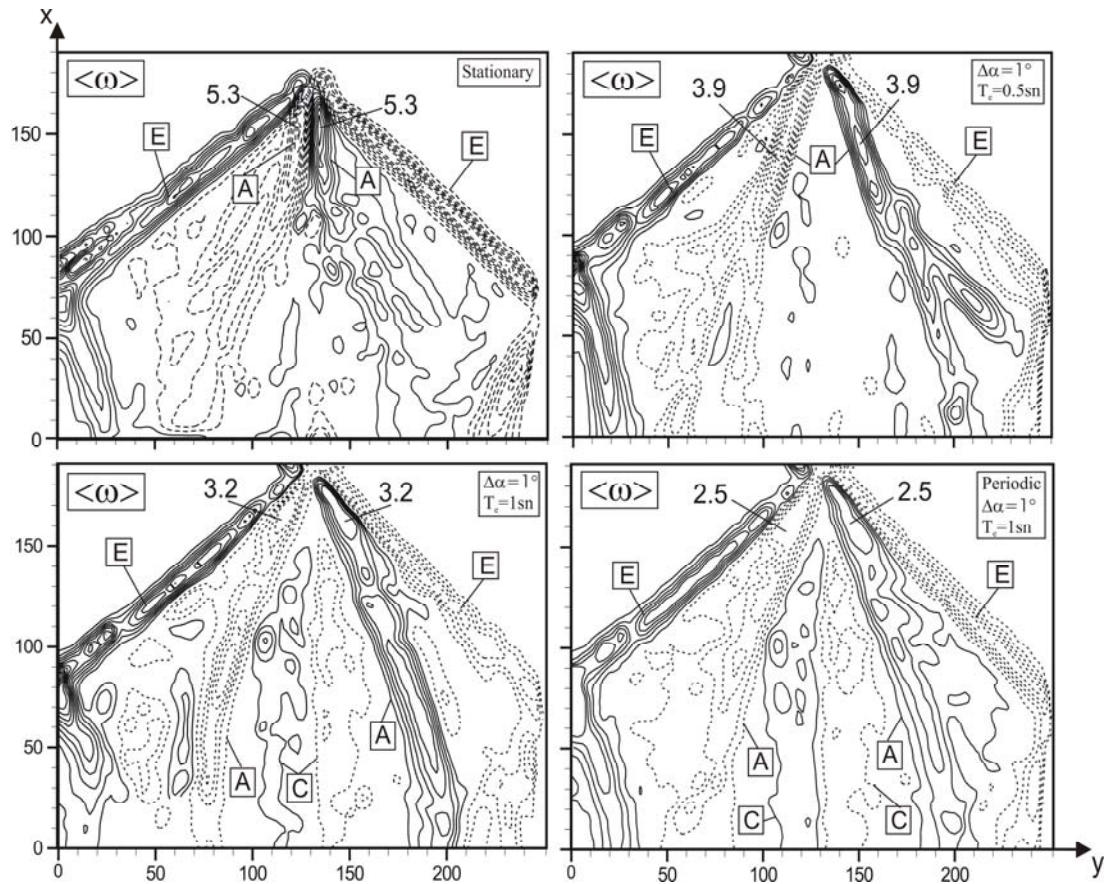
Figure 4.28. Patterns of time-averaged vorticity, <ω> for mean angle of attack, $\overline{\alpha}$ =10°.

Patterns of near-surface streamline, <Ψ> topology are presented in Figure 4.29 for the cases of stationary wing, continuously perturbed wing and periodicly perturbed wing. In the case of stationary wing for mean angle of $\overline{\alpha}$ =10°, positive bifurcation lines, L^+ which represent a line of attachment is developed on both sides of the central axis of the wing. Along the leading edge, negative bifurcation lines, L^- are formed indicating the separation of the flow. On these bifurcation lines, L^- saddle points, S take place. Here, streamlines merge into a single line expending all along the leading edges. These saddle points occur near the trailing edge of the lambda wing. A well-defined a pair of foci, F_1 and F_2, which represent the center of an inward swirl pattern of streamlines and three-dimensional separation occurs immediately downstream of the wing apex for stationary conditions. The positive bifurcation line of each vortex, L^+ moves away from each other for the cases of

continuously perturbed wing with T_e =0.5 and 1 s and periodically perturbed wing with T_e =1 s. In addition, a positive and negative bifurcation lines (L^+ and $\overline{L}$) are evident in all cases. The direction of the positive bifurcation line, L^+ at all cases of perturbation is actually reversed, relative to that negative bifurcation line, $\overline{L}$ on the stationary wing. Moreover, for all perturbed wing cases, the large-scale of swirling pattern, so prevalent in the pattern of stream lines <Ψ> on the stationary wing, is no longer evident and, note that the saddle points also no longer exist. In the case periodically perturbed wing with T_e =1 s, the spanwise extent, β of the inflow region of the streamline patterns is significantly increased.
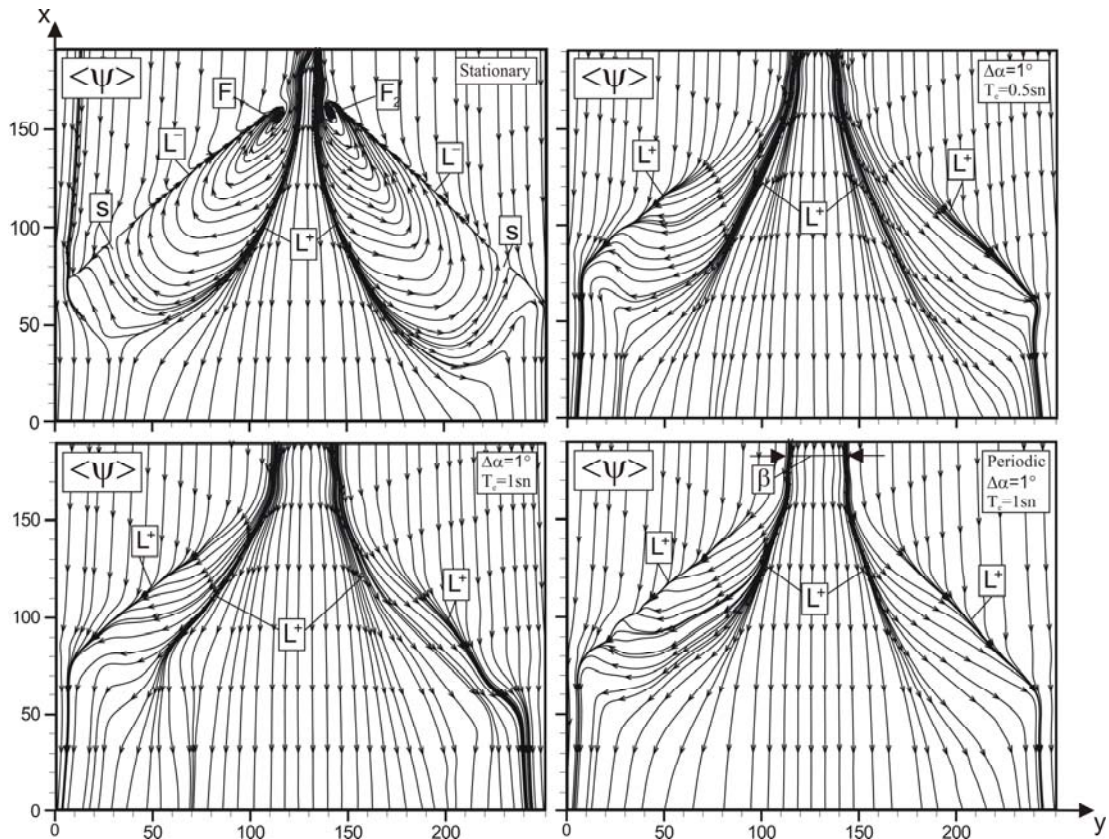
Figure 4.29. Time-averaged patterns of near-surface streamline, <Ψ> for mean angle of attack, $\overline{\alpha}$ =10°.

Figure 4.30 shows the time-averaged velocity vectors, <V>, field over the lambda wing for all wing cases. The distributions of time-averaged velocity vectors,

<V>, show that velocity vectors have relatively high magnitude on both side of the mid-chord axis, however, farther outboard from the plane of symmetry. The magnitude of velocity becomes relatively small which coincides with bifurcation lines. The spatial extent of the region of very low velocity at all perturbed wing cases is decreased comparing to the case of stationary wing. Furthermore, though a well-defined swirl pattern of velocity exists at the stationary wing case, absence of swirling patterns of velocities for the cases of continuously perturbed wing with T_e =0.5 and 1 s and periodically perturbed wing with T_e =1 s is evident in the near region of the apex. In the central portion of each of these swirl patterns, the magnitude of, <V>, is very small.
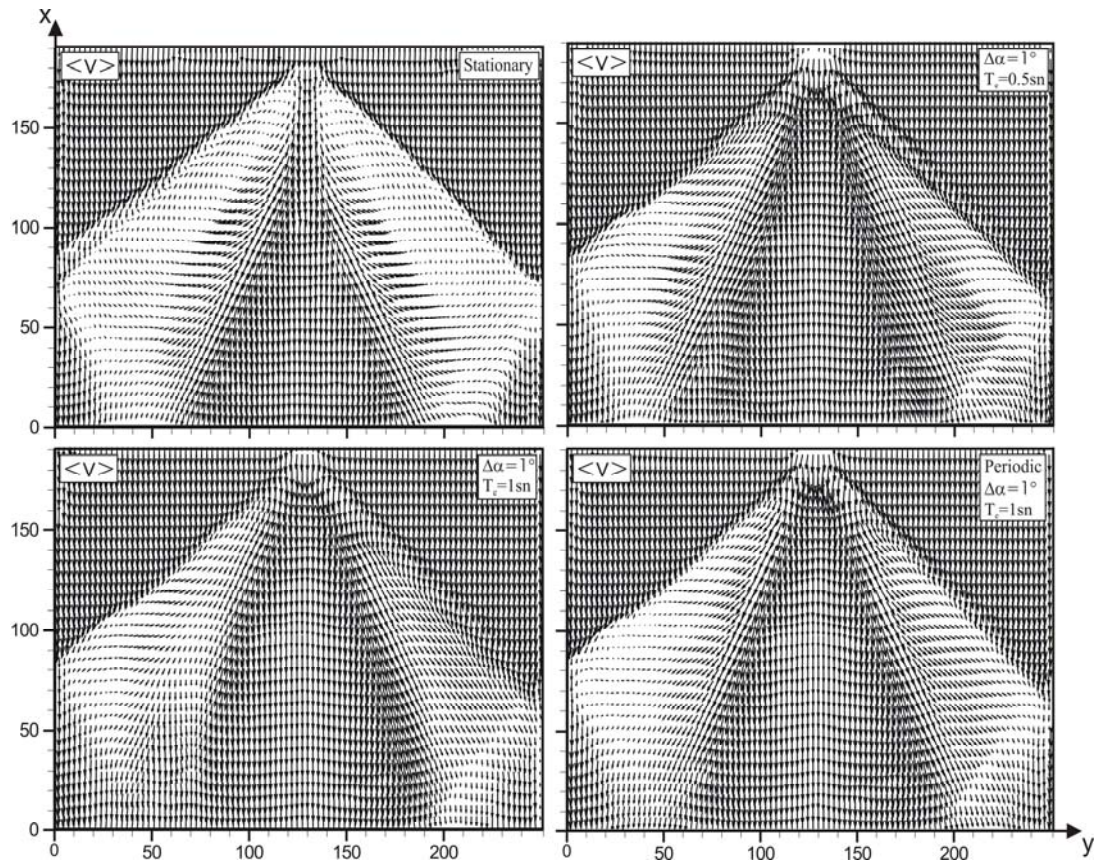
Figure 4.30. Time-averaged patterns of near-surface velocity, <V > for mean angle of attack, $\overline{\alpha}$ =10°.

Figure 4.31 shows the contours of streamwise velocity component, $<u>/U$ for stationary, continuous perturbation and periodic perturbation wing cases. Contours indicated by the solid and dashed lines, respectively, represent negative and positive $<u>/U$, in which the positive sign, corresponds to the upward direction. The minimum and incremental values of contours of dimensionless streamwise velocity, $<u>/U$, due to the previously mentioned reasons were kept constant for better comparison between the time-averaged streamwise velocity components.

    The maximum values of positive streamwise velocity components, $<u>/U$ are 0.85, 1.15, 1.00 and 1.10 for the cases of stationary wing, continuously perturbed wing with T_e =0.5 s and 1 s and periodically perturbed wing with T_e =1 s, respectively. As seen in the case of stationary wing the contours of streamwise time-averaged velocity component, $<u>/U$, has a negative velocity distributions on both side edges of the wing. Magnitude of the maximum values of negative streamwise velocity component, $<u>/U$ are 0.15 for the case of stationary wing and negative streamwise velocities are vanished for all other cases. The maximum values of the positive streamwise velocity component, $<u>/U$ for all cases are the same downstream of the trailing edge. When the lambda wing is subjected to perturbations with a small-amplitude over a certain range of periods, vortex breakdowns that are indicated on both sides of the wing chord axis occur closer to the apex as seen from the dye visualization images presented in Figure 4.26 On the other hand, these vortex breakdowns for the case of periodic perturbation having T_e =1 s further downstream occur away from the apex. Finally, it is remarkable that this discernible alteration of the onset of vortex breakdown seems to have supstantial influence on the patterns of $<u>/U$ even in the near surface of the wing.
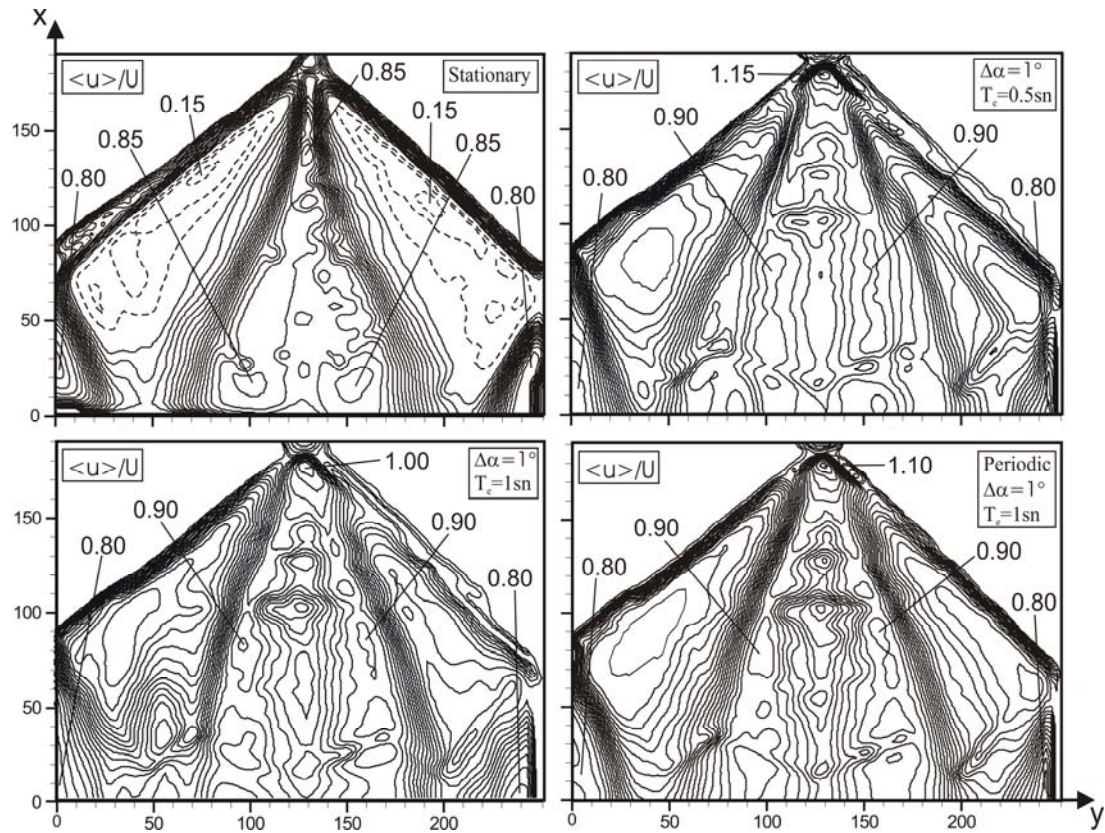
Figure 4.31. Time-averaged component of streamwise, [<u>/U] velocity for the
mean angle of attack, $\overline{\alpha}$ =10°. Minimum and incremental values are
[<u>/U]$_{min}$ =0.05 and Δ[<u>/U] =0.05.

Figure 4.32 shows the consequence of the perturbations on the contours of
transverse velocity <v>/U, relative to the stationary wing condition. Three different
pairs of clusters of transverse velocity, <v>/U components are developed over the
wing surface for the stationary wing condition. The first pair that is symbolized as A,
generates two well-defined clusters of main positive and negative contours of
transverse velocity component, <v>/U at both sides of the wing chord axis for all
conditions. Also, the second pair of clusters symbolized as B occurs along the side
edges of the wing. The third pair that is symbolized as C takes place between clusters
A and B for only stationary wing condition. For the C, vice versa condition is valid,
i.e. transverse velocity patterns of C on the left hand side of the wing are negative,
velocities on the right hand side of the wing are positive. The third pair of clusters, C

is vanished for all other conditions. Patterns of transverse velocity which are symbolized as A and B on the left hand side of wing chord axis are positive, and the transverse velocity patterns of the A and B on the right hand side of the wing chord axis are negative.

The maximum values of positive and negative transverse velocity components, $<v>/U$ are 0.30, 0.35, 0.25 and 0.35 for the stationary, continuous perturbation having T_e =0.5 and 1 s and periodic perturbation having T_e =1 s conditions, respectively. Perturbing the wing with the period of T_e =1 s results in a substantial reduction of the peak value of $<v>/U$. Taking the values of continuous perturbation as T_e = 1 s and periodic perturbation as T_e =1 s, the maximum values of $<v>/U$ higher than the values for the stationary wing case.
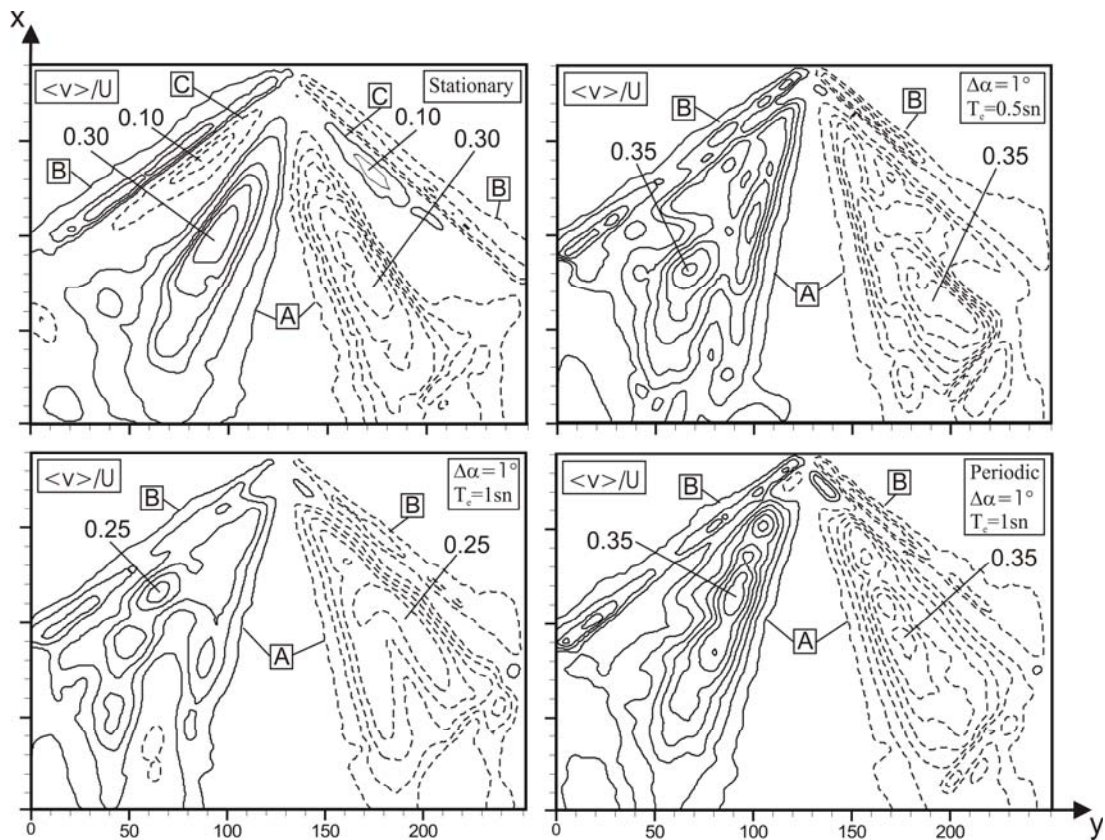
Figure 4.32. Time-averaged component of transverse, [$<v>/U$] velocity for the mean angle of attack, $\bar{\alpha}$ =10°. Minimum and incremental values are [$<v>/U]_{min}$ =0.05 and $\Delta[<v>/U]$ =0.05.

Figure 4.33 presents the time-averaged contours of vertical velocity component, <w>/U for stationary, continuous perturbation and periodic perturbation conditions. The maximum values of the vertical velocity components, <w>/U are smaller than the streamwise and transverse velocity components, <u>/U and <v>/U over the lambda wing surface for all cases. The maximum values of positive and negative vertical velocity components, <w>/U for the stationary, continuous perturbation with T_e =0.5 and 1 s and periodic perturbation with T_e =1 s cases are shown as 0.15, 0.25, 0.20 and 0.20, respectively. The maximum values of vertical velocity component, <w>/U for all conditions are lower than streamwise velocity component, <u>/U downstream of the trailing edge.
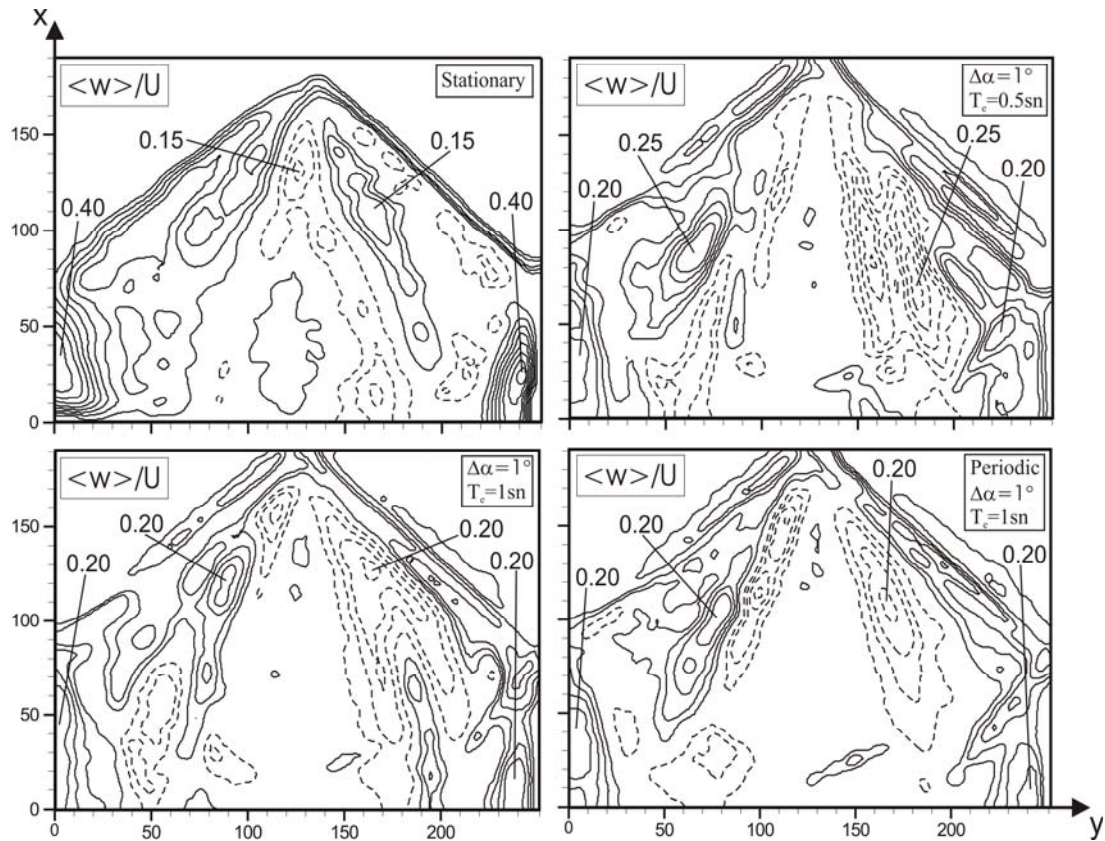

Figure 4.33. Time-averaged component of vertical, [<w>/U] velocity for the mean angle of attack, $\overline{\alpha}$ =10°. Minimum and incremental values are [<w>/U]$_{min}$ =0.05 and Δ[<w>/U] =0.05.

111

The analysis of the dimensionless fluctuating velocity component indicates that the maximum of turbulence level occur along the shear layer. Figure 4.34 indicates streamwise, transverse and vertical Reynolds normal stress correlations, $<u\acute{}u\acute{}>/U^2$, $<v\acute{}v\acute{}>/U^2$ and $<w\acute{}w\acute{}>/U^2$ to reveal its effect on turbulent kinetic energy for all wing cases. The minimum and incremental values of contours for streamwise, transverse and vertical Reynolds normal stresses, $<u\acute{}u\acute{}>/U^2$, $<v\acute{}v\acute{}>/U^2$ and $<w\acute{}w\acute{}>/U^2$ are the same and equal to 0.002 and 0.005, respectively. Figure 4.34 shows that the maximum values of streamwise and vertical Reynolds normal stresses, $<u\acute{}u\acute{}>/U^2$ and $<w\acute{}w\acute{}>/U^2$ for the continuously perturbed wing case with T_e =0.5 and mean angle of attack, $\overline{\alpha}$ =10° is the lowest according to the other oscillation cases over the surface of the wing. On the other hand, maximum values of normalized transverse Reynolds normal stress, $<v\acute{}v\acute{}>/U^2$ are the same and equal to 0.032 for all cases. The maximum values of normalized streamwise Reynolds normal stress, $<u\acute{}u\acute{}>/U^2$ are 0.022, 0.037, 0.057 and 0.0047 and for normalized vertical Reynolds normal stress, $<w\acute{}w\acute{}>/U^2$ is 0.032, 0.062, 0.112 and 0.082 for stationary wing case, continuously perturbed and periodically perturbed wing cases, respectively.

Results of the turbulent kinetic energy, TKE for all cases are shown in Figure 4.35. For minimum and incremental values of the contours of time-averaged turbulent kinetic energy, TKE was taken as $[<TKE>]_{min}$=0.01 and $\Delta[<TKE>]$=0.005, respectively.

The maximum values of TKE for cases of stationary wing continuously perturbed wing and periodically perturbed wing are 0.030, 0.040, 0.055 and 0.050, respectively. Turbulent kinetic energy, TKE is related to the normalized components of the Reynolds normal stresses, $<u\acute{}u\acute{}>/U^2$, $<v\acute{}v\acute{}>/U^2$ and $<w\acute{}w\acute{}>/U^2$. TKE increases gradually over the wing surface when oscillations are given to the wing. In Figure 4.34, examining the maximum values of the normalized components of Reynolds normal stresses, $<u\acute{}u\acute{}>/U^2$, $<v\acute{}v\acute{}>/U^2$ and $<w\acute{}w\acute{}>/U^2$, it is seen that, the maximum value of the vertical Reynolds normal stresses, $<w\acute{}w\acute{}>/U^2$ is higher than the streamwise and transverse Reynolds normal stress, $<u\acute{}u\acute{}>/U^2$ and $<v\acute{}v\acute{}>/U^2$ for all perturbation conditions. Contribution of vertical Reynolds normal stress,

$<w'w'>/U^2$ on the formation of TKE is higher compared to the effects of the streamwise and transverse Reynolds normal stresses, $<u'u'>/U^2$ and $<v'v'>/U^2$.
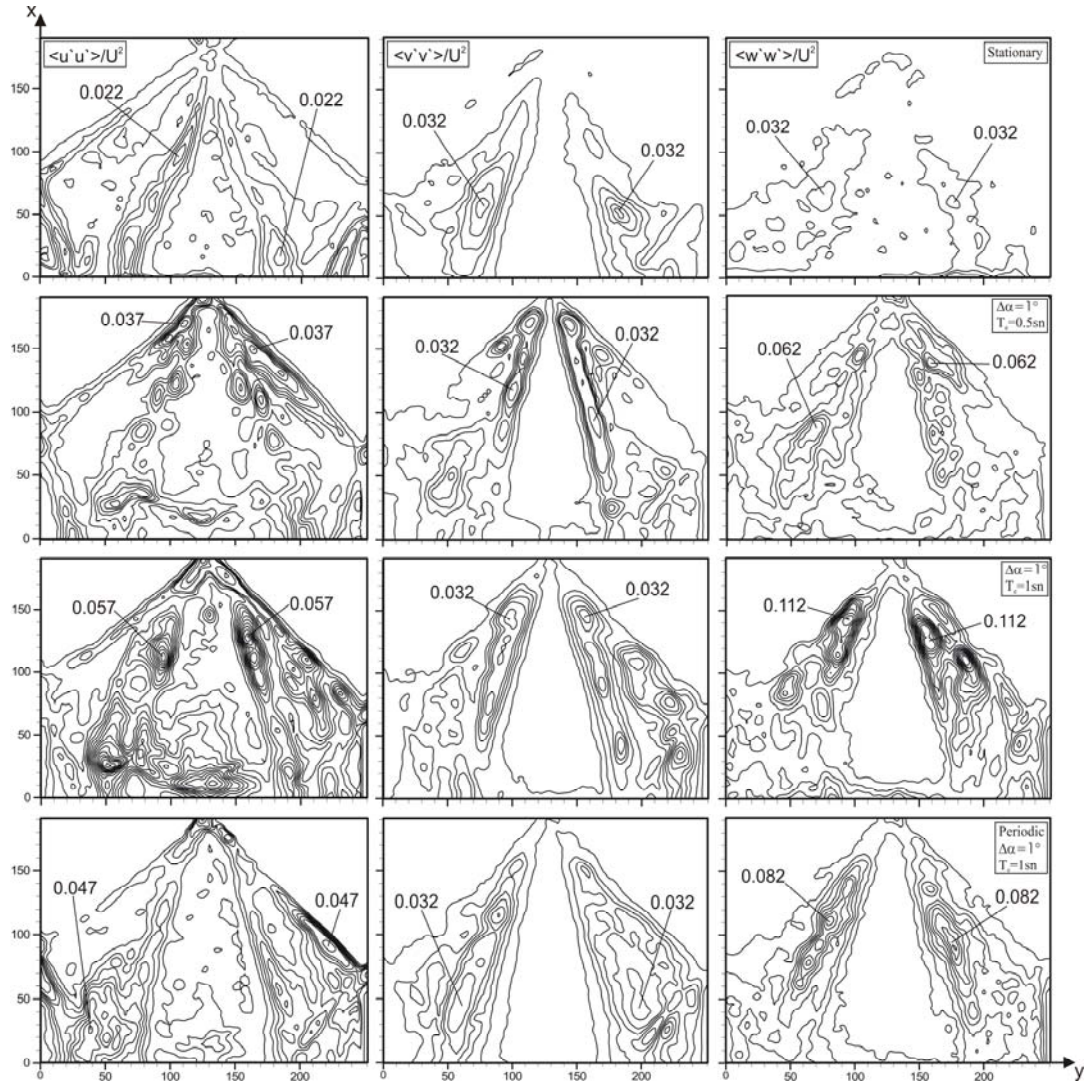
Figure 4.34. The contours of time-averaged Reynolds normal stress components for the mean angle of attack, $\overline{\alpha}$ =10°.
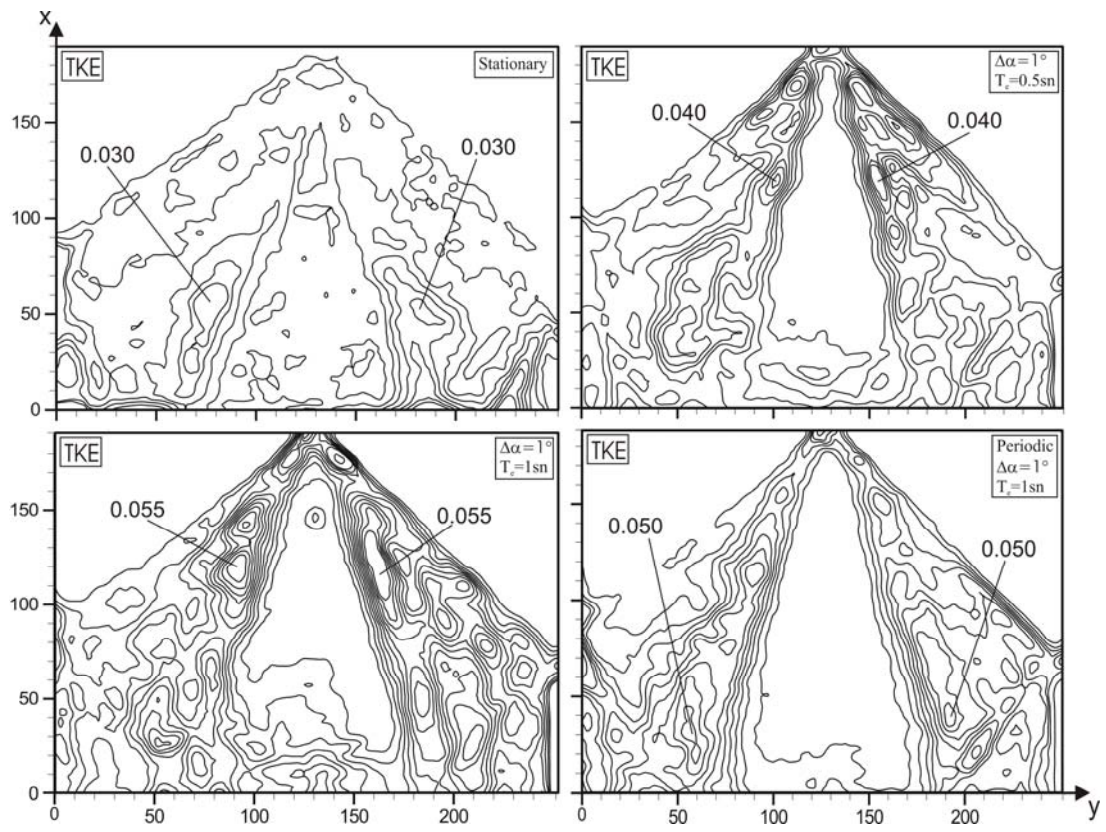
Figure 4.35. The contours of time-averaged turbulent kinetic energy (TKE) for the mean angle of attack, $\overline{\alpha} = 10°$.

5. CONCLUSIONS

5.1. Overall Conclusions

The flow structure on the diamond and lambda wings of low sweep angle exhibits a number of distinctive characteristics, relative to the extensively investigated case of a slender, highly-swept delta wing. The main purpose of the present study is to investigate details of flow structure over the diamond and lambda wings, in plan-view and end-view planes.

5.1.1. Effect of Yaw Angle over the Diamond Wing for Angle of Attack of $\alpha=10°$

The present investigation focuses on a number of fundamental phenomena, which are formation and development of leading-edge vortices, vortex breakdown, three dimensional separation and non-steady flow structure over a diamond wing. These phenomena are inspected both qualitatively and quantitatively using dye visualization and the Particle Image Velocimetry (PIV) technique. The wing has a leading edge sweep angle of $\Lambda=40^{o}$ and the changes in the flow structure were obtained by varying yaw angle of the diamond wing within the range of $0^{o}\leq\theta\leq15^{o}$.

At zero yaw angle, two symmetrical leading edge vortices emanating from the wing apex are observed. Vortex breakdown and stagnation point occur along the central axis of these vortices. Symmetrical flow structure deteriorates with yaw angle changes of the diamond wing. However, this deterioration is not clearly observed for the yaw angles less than $\theta=4°$. When the yaw angle is increased beyond $\theta=4°$, vortex breakdown occurs in the downstream region of the diamond wing's trailing edge of the leeward side but vortex breakdown takes place close to the apex of the wing on the windward side.

Positive and negative streamwise, $<u>/U$ and transverse, $<v>/U$ velocity regions occur on the diamond wing for zero yaw angle. By increasing yaw angle, a decrease in the negative streamwise velocity, $<u>/U$ on the leeward side of the wing is seen. In addition, negative velocity region on the leeward side of the wing is vanished

when yaw angle is set to $\theta=15°$. In terms of transverse velocity component, $<v>/U$, three different pairs of clusters of transverse velocity component, $<v>/U$ are developed over the surface of the wing. These pairs are affected with yaw angle variation. For example, when yaw angle is set to $\theta=15^o$, two different pairs of clusters of transverse velocity component, $<v>/U$ remain on the diamond wing.

Patterns of the root mean square of streamwise and transverse velocity components, u_{rms}/U and v_{rms}/U reveal that the maximum values of u_{rms}/U and v_{rms}/U decrease with increasing yaw angle since the vortex breakdown location moves towards the trailing edge on the leeward side of the wing. But, these components, u_{rms}/U and v_{rms}/U are not affected by the yaw angle on the windward side of the wing. The maximum value of Reynolds-stress correlation $<u'v'>/U^2$ decreases over the surface of the wing when the yaw angle is increased.

For all yaw angles, the maximum value of the transverse Reynolds normal stress, $<v'v'>/U^2$ is smaller than those of streamwise and vertical Reynolds normal stresses, $<u'u'>/U^2$ and $<w'w'>/U^2$ over the surface of the wing. This result reveals that the effect of transverse Reynolds normal stresses on the turbulent kinetic energy is less effective compared to the effects of streamwise and vertical Reynolds normal stresses, $<u'u'>/U^2$ and $<w'w'>/U^2$. The change in the turbulent kinetic energy on the windward side of the wing is negligibly small with yaw angle.

5.1.2. Effect of Yaw Angle over the Diamond Wing for Angle of Attack of $\alpha=7°$

The main issues of this work are formation and development of the vortices on the leading edge of the wing, vortex breakdown and flow separation. According to flow direction of the diamond wing; changes of flow structure are observed by varying the yaw angle between the ranges of $0^0 \leq \theta \leq 15^0$. From the measured instantaneous velocity vectors; the time-averaged vorticity $<\omega>$, streamlines $<\psi>$, velocity vectors, $<V>$ the root mean square of streamwise and transverse velocity components, u_{rms}/U and v_{rms}/U, and Reynolds stress correlations, $<u'v'>/U^2$ are calculated for the values of angle of attack equals to $\alpha=7°$, and a variety of yaw

angles both in plan view and end view planes. Briefly, the characteristic properties of the flow structure are tried to be explained on the diamond wing models.

Location of the vortex breakdown and flow symmetry change rapidly varying the yaw angle. The unsteady vortex flow structure that is formed on the wing surface, affects the symmetry which is found at both side of the wing central axis. There is not much difference between two vortex structures for $\theta \geq 4°$. But, for the yaw angle of $\theta \leq 6°$, the similarity of the spiral vortices are deteriorates. The spiral vortex that is formed on the windward side of the wing breaks down earlier. But, other spiral vortex breakdown occurs further downstream with respect to the wing apex.

If the angle of attack is set to $\alpha=7^{0}$ leading edge vortex begins with a spiral structure and then vortex breakdown takes place creating a separated flow region. As a result, after the vortex breakdown, the wing surface is exposed to unsteady flow loadings.

5.1.3. Variation of the Flow Structure for different angles of attack over the Lambda Wing

The present investigation focuses on a fundamental flow phenomena, which are formation and development of leading-edge vortices, vortex breakdown and three dimensional separation and stall, and disorganized flow structure in the plan-view plane in close proximity to the surface of the wing having leading edge sweep angle of $\Lambda=40^{o}$ to investigate both qualitatively and quantatively using dye visualization and the PIV technique.

In the plan-view plane, examining all dye visualization experiments, there is a symmetrical time-averaged flow structure on both sides of wing chord axis over the lambda wing in all cases of angles of attack. Also, there is a coherent pair of leading-edge vortices starting from the apex of the wing. The structure of these coherent leading edge vortices decomposes developing vortex breakdown further downstream in the freestream flow direction. The vortex breakdown is developed on the apex of the wing for angles of attack of $\alpha=13°$ and $17°$. A pair of foci F_1 and F_2 begins to appear near the apex in the plan-view plane close to the wing surface for attack

angle, α=10° presented by the streamline topology, <Ψ>. Domain of these pair of foci, F_1 and F_2 is enlarged and, the positive bifurcation lines, L^+ on both side of the chord axis are developed which get closer to each other for higher angle of attack, α. The maximum value of the contours of the time-averaged vorticity, <ω> is the highest for the angle of attack of α=10° in comparison to the other cases of attack angles, α. The maximum values of the time-averaged velocity components decrease on the other hand, the magnitude fluctuating velocities increase near the wing surface when the angle of attack, α is increased. However, at the highest angle of attack α =17°, the patterns flow characteristics have a fundamentally different structures. The maximum values of fluctuating velocities at α =17° is substantially lowered than the case of α =13°. Turbulent kinetic energy, TKE which is related to fluctuating velocities increases over the wing surface having angles of attack of α=7°, 10° and 13°.

In the end-view plane at a location x/C=0.6, as soon as vortex breakdown occurs a coherent leading edge vortex core disintegrates into small scale vortices. The main spanwise rotating vortices occur close to the central axis of the lambda wing. By increasing the angle of attack, α area or diameter of the separated flow increases and the separated flow covers the wing surface entirely. It is found that by increasing the angle of attack, α values of positive and negative time-averaged vorticity, <ω> are lowered and central points of cluster of vorticity approach to the central axis of the wing. Fluctuations in the vertical root-mean-square velocities, w_{rms}/U and the Reynolds-stress correlations increase due to the formation of the vortex breakdown in location close to the apex under a high angle of attack, α.

5.1.4. Perturbations of the Lambda Wing: Control of Vortex Breakdown

The present study also investigates the flow characteristics over a lambda wing on cross-flow planes where vortex breakdown and stall phenomena occur. As a consequence, the important issues of the flow structure can be summarized as follows:

The focus of the present investigation is given on the vertical flow structure exist in the near-surface of the wing having low sweep angle and sufficiently high angle of attack. The aforementioned representations are provided for the case of the stationary wing, as well as for the wing subjected to small-amplitude perturbations.

For the case of the stationary wing, the time-averaged patterns of streamline, $<\Psi>$ topology show well-defined critical points, which are symmetrical with respect to the plane of symmetry of the wing. The unsteady aspects of the near-surface velocity fluctuations are evident in corresponding patterns of Reynolds normal stress correlations, $<u'v'>/U^2$ especially in regions beneath vortex breakdown.

Perturbing the lambda wing can modify the time-averaged flow structures to a moderate level. But, velocity fluctuations gradually increase during the wing perturbation in the near-surface of the wing. This magnification of fluctuations happen due to the vibration of the wing caused perturbation. It is thought that in the real application one should only perturb a small size mechanism in the apex region in order to minimize the vibrated surface (wall) effect. These alterations are demonstrated in terms of the time-averaged streamline, $<\Psi>$ topology and the corresponding time-averaged velocity vectors over the wing surface. The number of critical points of the topology can be reduced in the presence of perturbations. Furthermore, a significant reduction in the magnitude of the surface-normal vorticity is attainable at certain locations along the wing surface. Turbulent kinetic energy, TKE is related to fluctuating velocities. TKE increases over the wing surface in all cases since the fluctuations in velocity components are magnified because of the whole wing is perturbed.

5.2. Suggestions for Future Studies

Unsteady pressure or force measurement must be studied in order to obtain further insight into the induced loading from the unsteady processes of vortex breakdown and stall under yaw angle.

REFERENCES

ADRIAN, R. J., 2005. Twenty Years of Particle Image Velocimetry. Experimental Fluids, Vol. 39, pp. 159–169.

AKILLI, H., SAHIN, B. AND ROCKWELL, D., 2001. Control of Vortex Breakdown by a Transversely-Oriented Wire. Physics of Fluids, Vol. 13, No. 2, pp. 452-463.

AKILLI, H., ŞAHIN, B., AND ROCKWELL, D., 2003. Control Of Vortex Breakdown By a Coaxial Wire. No. 1, Vol. 15, pp. 123-133.

ANDERSON, J.D., 2001. Fundamentals of Aerodynamics. McGraw-Hill Higher Education, ISBN 0-07-118146-6.

BREITSAMTER C., 2008. Unsteady Flow Phenomena Associated With Leading-Edge Vortices. Progress in Aerospace Sciences, Vol. 44, pp. 48–65.

CANPOLAT, C., YAYLA, S., SAHIN, B., AND AKILLI, H., 2009. Dye Visualization of the Flow Structure over a Yawed Nonslender Delta Wing. The Journal of Aircraft, Vol. 46, No. 5.

CUI, Y. D. , LIM T. T., TSAI H. M., 2007. Control of Vortex Breakdown over a Delta Wing Using Forebody Slot Blowing. AIAA Journal, Vol. 45, No. 1.

COTON F. N., JUPP M. L., AND GREEN R. B., 2001. Analysis Of Unsteady Pressure Signals On Pitching Delta Wing. AIAA Journal, Vol. 39, No. 9.

DENİZ, S., AND STAUBLİ, T., 1997. Oscillating Rectangular And Octagonal Profiles : Interaction Of Leading-And Trailing-Edge Vortex Formation. Journal of Fluids and Structures, Vol. 11, pp. 3 − 31.

DANTEC DYNAMICS v4.71 Flowmap Software Manual.

DENG, Q., GURSUL, I., 1997. Vortex Breakdown Over A Delta Wing With Oscillating Leading Edge Flaps. Experiments in Fluids, Vol. 23, pp. 347-352 (Springer-Verlag).

ELKHOURY, M. AND ROCKWELL, D., 2004. Visualized Vortices on Unmanned Combat Air Vehicles Planform: Effect of Reynolds Number. Journal of Aircraft", Vol. 41, No. 5, pp. 1244-1246.

GALLANZI, M. F., 1998. High Accuracy Measurement of Unsteady Flows Using Digital Particle Image Velocimetry. Optics & Laser Technology, Vol. 30, Pp. 349-359.

GORDON, S.T. AND GURSUL, I., 2004. Lift enhancement over a flexible delta wing. AIAA paper, No. 2618, pp. 1-11.

GORDNIER, R.E., VISBAL, M.R., 2004. Computation Of The Aeroelastic Response Of A Flexible Delta Wing At High Angles Of Attack. Journal of Fluids and Structures 19, pp.785–800.

GORUNEY, T., ROCKWELL, D., 2009. Flow Past a Delta Wing with a Sinusoidal Leading Edge: Near-Surface Topology and Flow Structure. Exp Fluids, Vol. 47, pp. 321–331.

GURSUL, I. AND YANG, H., 1995. On Fluctuations of Vortex Breakdown Location", Physics of Fluids, Vol. 7, No. 1, pp. 229-231.

GURSUL, I., GORDNIER, R. AND VISBAL, M., 2005a. Unsteady Aerodynamics of Non-slender Delta Wings. Progress in Aerospace Sciences Vol. 41, pp. 515–557.

GURSUL I., 2005b. Review of Unsteady Vortex Flows over Slender DeltaWings. Journal of Aircraft, Vol. 42, No. 2.

GURSUL, I., VARDAKİ, E., MARGARİS, P., AND WANG, Z., 2006. Control of Wing Vortices. Department of Mechanical Engineering University of Bath, BA2 7AY, United Kingdom.

GURSUL, I., WANG, Z., VARDAKİ, E., 2007. Review Of Flow Control Mechanisms Of Leading-Edge Vortices. Progress in Aerospace Sciences 43, pp. 246–270.

HART, D. P., 2000. PIV Error Correction. Experiments in Fluids, Vol:29, pp.13-22.

HEBBAR, S. K., PLATZER, M. F., FRITZELAS, A. E., 2000. Reynolds Number Effects On The Vortical-Flow Structure Generated By A Double-Delta Wing. Experiments in Fluids, Vol. 28, pp. 206-216.

HERON, I., AND MYOSE, R.Y., 2004. On the Impingement of a Von Karman Vortex Street on a Delta Wing. 22nd Applied Aerodynamics conference and exhibit, pp.16-19.

HUANG, H., DABIRI, D., and GHARİB, M., 1997. On Errors of Digital Particle Image Velocimetry. Measurement Science and Technology, Vol.8, pp.1427–1440.

KAWAZOE H., KATO S., 2006. Effects of Leading Edge Seperation Vortex of Flexible Structure Delta Wing on Its Aerodynamic Characteristics. Jsme International Journal, Series B, Vol. 49, No. 4.

KHAN, F.R., RİELLY, C.D., BROWN, D.A.R., 2006. Angle-Resolved Stereo-Pıv Measurements Close To A Down-Pumping Pitched-Blade Turbine. Chemical Engineering Science, Vol. 61, pp. 2799 – 2806.

KUROSAKA, M., KİKUCHİ, M., HİRANO, K., YUGE, T., AND INOUE H., 2003. Interchangeability of Vortex-Breakdown Types. Experiments in Fluids, Vol. 34, pp. 77–86.

LEE, M., HO, C. M., 1989. Vortex Dynamics of Delta Wing. Ph. D. Thesis, Department of Aerospace Engineering University of Southern California.

LEVİNSKİ, O., 2001. Review of Vortex Methods for Simulation of Vortex Breakdown. Airframes and Engines Division Aeronautical and Maritime Research Laboratory, DSTO-TR-1211, Commonwealth of Australia.

LİN, H., 1998. Vortex Breakdown Over Delta Wings in an Unsteady Free Stream. Ph.D. thesis, University of Southern California.

LUCCA-NEGRO, O., AND O'DOHERTY, T., 2001. Vortex Breakdown: a Review. Progress in Energy and Combustion Science, Vol. 27, pp. 431-481.

MATSUNO, T., AND NAKAMURA, Y., 2000. Self-Induced Roll Oscillation of 45 Degree Delta Wings. 38th AIAA Aerospace Sciences Meeting and Exhibit.

MENKE, M., YANG, H. AND GURSUL, I., 1999. Further Experiments On Fluctuations Of Vortex Breakdown Location. AIAA Paper No. 96-0205, 34th Aerospace Sciences Meeting and Exhibit, January 15-18, Reno, NV.

MITCHELL, A., MOLTON, P., BARBERIS, D., DELERY, J., 1999. Characterization of Vortex Breakdown by Flow Field and Surface Measurements. AIAA 3202.

MOCHIZUKI, S., YAMADA, S., AND OSAKA H., 20006. Reynolds Stress Field In a Turbulent Wall Jet Induced By a Streamwise Vortex With Periodic Perturbation. Experiments in Fluids, Vol. 40, pp. 372–382.

MOUL, T. M., FEARS, S. P., ROSS, H. M. AND FOSTER, J. V., 1995. Low-Speed Wind-Tunnel Investigation of the Stability and Control Characteristics of a Series of Flying Wings With Sweep Angles of 60°. NASA Technical Memorandum 4649.

OL, M. V., AND GHARIB, M., 2001. The Passage Toward Stall of Nonslendar Delta Wings at Low Reynolds Number. AIAA, pp. 2001-2843.

OZGOREN, M., 2000. Impingement of Vortex Breakdown upon an Edge: Flow Structure and Origin of Loading. Ph. D. Thesis, pp. 32.

OZGOREN, M., SAHIN, B., AND ROCKWELL, D., 2001. Perturbations Of A Delta Wing: Control Of Vortex Buffeting. Journal of Aircraft, No.6, Vol. 38.

OZGOREN, M., SAHIN, B., AND ROCKWELL, D., 2002. Vortex Structure on a Delta Wing at High Angle-of-Attack. AIAA Journal, Vol. 40, No. 2, pp. 285-292.

PRASAD, A. K., AND ADRIAN, R. J., 1995. Scheimpflug Stereocamera for Particle Image Velocimetry to Liquid Flows. Applied Optics, Vol. 34, pp. 7092-7099.

RENAC, F., BARBERİS, D., AND MOLTON, P., 2005. Control of Vortical Flow over a Rounded Leading-Edge DeltaWing. AIAA Journal, Vol. 43, No. 7.

ROCKWELL, D. 2000. Imaging of Unsteady Sperated Flows: Global Approaches to New Insight. Experiments in Fluids, Vol. 29, No.7, pp. 255-273.

SAHIN, B., AKILLI, H., LIN, J.-C. AND ROCKWELL, D., 2001. Vortex Breakdown Edge Ineraction: Consequence of Edge Oscillations. AIAA Journal, Vol. 39, No.55, pp. 865-876.

SARPKAYA, T., 1971. On Stationary and Traveling Vortex Breakdowns. Journal of Fluid Mechanics, Vol. 45, No. 3, pp. 545-559.

YAYLA, S., CANPOLAT, C., SAHIN, B., AND AKILLI, H., 2009. Effect of Yaw Angle on the Formation of Vortex Breakdown over the Diamond Wing Journal of Thermal Science and Technology, Accepted for Publication.

SOHN, M. H., LEE, K. Y., AND CHANG, J. W., 2004. Vortex Flow Visualization of a Yawed Delta Wing with Leading-Edge Extension. Journal of Aircraft, Vol. 41, No. 2.

SOLOFF, S. M., ADRIAN, R. J., and LIU, Z. C., 1997. Distortion Compensation for Generalized Stereoscopic Particle Image Velocimetry. Measurement Science and Technology, Vol. 8, Pp. 1441–1454.

TAYLOR, G. S., SCHNORBUS, T., AND GURSUL, I., 2003. An Investigation of Vortex Flows over Low Sweep Delta Wings. AIAA Fluid Dynamics Conference, 23-26 June, Orlando, FL.

TAYLOR, G.S., GURSUL, I., 2004. Buffeting Flows Over A Low-Sweep Delta Wing. AIAA Journal, Vol. 42, No. 9.

TURNEY, D. E., ANDERER, A., AND BANERJEE, S., 2009. A Method for Three-Dimensional Interfacial Particle Image Velocimetry (3D-IPIV) of an Air–Water Interface. Measurement Science and Technology, Vol. 20, 045403 (12pp).

VAN DOORNE, C. W. H., WESTERWEEL, J., 2007. Measurement of Laminar, Transitional and Turbulent Pipe Flow Using Stereoscopic-Piv. Exp Fluids, vol. 42, Pp:259–279.

VERHAAGEN, N. G., AND NAARDING, S. H. J., 1989. Experimental and Numerical Investigation of Vortex Flow over a Sideslipping Delta Wing. Journal of Aırcraft, Vol. 26, No. 11.

VIIERU, D., TANG, J., LIAN, Y., LIU, H., AND SHYY, W., 2006. Flapping and Flexible Wing Aerodynamics of Low Reynolds Number Flight Vehicles. 44th AIAA Aerospace Sciences Meeting and Exhibit, Reno, Nevada 9 - 12 January.

WANG, J. J., ZHANG, W., 2008. Experimental Investigations on Leading-Edge Vortex Structures for Flow over Non-Slender Delta Wings. Chin.Phys.Lett., Vol. 25, No. 7.

WANG, J. J., AND XU, Y., 2004. Experimental Studies on Control of DeltaWing Aerodynamics", AIAA Journal Vol. 42, No. 2.

WASZAK, R. M., JENKİNS, N. L., AND IFJU, P., 2001. Stability and Control Properties of an Aeroelastic Fixed Wing Micro Aerial Vehicle. AIAA Paper 2001-4005, presented at the AIAA Atmospheric Flight Mechanics Conference and Exhibit, Montreal, Canada, Aug. 6-9.

WESTERWEEL, J., 1994. Efficient Detection of Spurious Vectors in Particle Image Velocimetry Data. Experiments in Fluids, Vol. 16, Issue: 3-4, Pp. 236-247.

WESTERWEEL, J., 1993. Digital Particle Image Velocimetry, Theory and Application. Delft University Pres.

WIENEKE, B., 2005. Stereo-Pıv Using Self-Calibration on Particle Images. Experiments in Fluids, vol.39, Pp:267–280.

WILLERTY, C., 1997. Stereoscopic Digital Particle Image Velocimetry for Application in Wind Tunnel Flows. Measurement Science and Technology, Vol. 8, Pp. 1465–1479.

YANIKTEPE B. AND ROCKWELL D., 2004. Flow Structure on a Delta Wing of Low Sweep Angle. AIAA Journal, Vol. 42, No. 3.

YANIKTEPE B. AND ROCKWELL D., 2005. Flow Structure on Diamond and Lambda Planforms:Trailing-Edge Region. AIAA Journal, Vol. 43, No. 7.

YANIKTEPE B. 2006. Origin and Control of Vortex Breakdown of Unmanned Combat Air Vehicles. Ph. D. Thesis, pp. 3.

YAVUZ, M., and ROCKWELL, D., 2006. Control of Flow Structure on Delta Wing with Steady Trailing-Edge Blowing. AIAA Journal, Vol. 44, No. 3.

YAVUZ, M., ELKHOURY, M., and ROCKWELL, D., 2004. Near-Surface Topology and Flow Structure on a Delta Wing. AIAA Journal, Vol. 42, No. 2, pp. 332-340.

CIRRICULUM VITAE

Sedat YAYLA 1977 yılında Van'da doğdu. İlk, orta ve lise eğitimini Van'da tamamladı. 2000 yılında Karadeniz Teknik Üniversitesi, Müh.-Mim. Fakültesi, Makine Mühendisliği bölümünden mezun oldu. 2000-2001 yılları arasında Jandarma Ana Tamir Fabrika Komutanlığı'nda (Güvercinlik/Ankara) proje mühendisi olarak askerlik görevini tamamladı. 2002 yılında Yüzüncü Yıl Üniversitesi, Müh.-Mim. Fakültesi, Makine Mühendisliği bölümünde Araştırma Görevlisi olarak göreve başladı. 2005 yılında Yüzüncü Yıl Üniversitesi, Fen Bilimleri Enstitüsü, Makine Mühendisliği Anabilim Dalında yüksek lisans öğrenimini tamamladı. Aynı yıl içerisinde Çukurova Üniversitesi, Fen Bilimleri Enstitüsü, Makine Mühendisliği Anabilim Dalında doktora öğrenimine başladı. Evli ve bir çocuk babasıdır.

APPENDIX A

Vorticity Evaluation

For 2-D flows, the out-of-plane component of vorticity is given by:

$$\Omega = \frac{1}{2}\left(\frac{\partial v}{\partial x} - \frac{\partial u}{\partial y}\right)$$

The most common way to compute this expression numerically is to approximate the partial derivatives with finite difference. Using central differences at an interior point to leads to:

$$\Omega_{ij} = \frac{1}{2}\left(\frac{v(i+1, j) - v(i-1, j)}{2\delta_x} - \frac{u(i, j+1) - u(i, j-1)}{2\delta_y}\right)$$

Any computation involving derivatives is very sensitive to noises that are the primary reason to try to smooth out the velocity field before computation of the vorticity, strain rate or similar gradient quantities.

Another way around the noise problem for the particular case of the computation of vorticity is to use a self-smoothing method derived from the Stokes theorem. This the so-called circulation method that the user can choose to compute the vorticity in NFILVB.

The stokes theorem can be formulated as:

$$\iint \left(\vec{\nabla} \times \vec{u}\right) d\vec{s} = \oint \vec{u} d\vec{l}$$

Assuming that the vorticity is constant all over the unit surface formed by the four grid cells surrounding a given point, the vorticity a that point is given by:

$$\Omega = \frac{1}{4\delta_x \delta_y} \oint \vec{u} d\vec{l}$$

where the integral is the circulation of the velocity around the path formed by the sides of the unit surface.

APPENDIX B

Bilinear Interpolation

To fill the gaps left in the data grid by the interrogation system NFILVB is using a bilinear least square fit technique.

Knowing the data values $u_1,\ldots, u_n$ at the N nearest neighbor location of a point where the data u is missing, the idea is to find a value for u that does not deviate too much from these values. To realize this goal, in a least square technique, one has to minimize the merit function:

$$\chi^2 = \sum_{k=1}^{N} \frac{|u_k - u|^2}{\sigma_k}$$

As suggested by Adrian et al., NFILVB is applying this method to a linear model of the 2 components of velocity:

$u = a_0 + a_1 x + a_2 y$

$v = b_0 + b_1 x + b_2 y$

using the 5 nearest neighbors of a missing data. The standard way to deal with the measurement errors σ_k, on each data u_k, when they are not known, is to set them to 1. The minimum of the merit function:

$$\chi^2 = \sum_{k=1}^{5} |u_k - (a_0 + a_1 x + a_2 y)|^2$$

occurs when:

$$\frac{\partial \chi^2}{\partial a_0}(x_k, y_k) = \frac{\partial \chi^2}{\partial a_1}(x_k, y_k) = \frac{\partial \chi^2}{\partial a_2}(x_k, y_k) = 0 \quad \text{for k=1,\ldots,5}$$

This is a linear system of 15 equations and 3 unknowns that is solved using the Singular Value Decomposition (SVD) technique described in the Numerical Recipes books.

Gaussian Smoothing

To reduce the measurement noises in the velocity data from PIV, a local weighted averaging technique is used in NFILVB. The weights used are Gaussian:

$$u(x_i, y_j) = \sum_{m=-4}^{4} \sum_{k=-4}^{4} w_{km} u(x_{i-k}, y_{j-m})$$

where:

$$w_{km} = \frac{\omega_{km}}{\sum_{k=-4}^{4} \sum_{m=-4}^{4} \omega_{km}}$$

and $\quad \omega_{km} = e^{\frac{2(k^2 + m^2)}{\sigma^2}}$

The parameter σ is the smoothing parameter that the user is asked for when running NFILVB. It controls how fast the Gaussian ω is decaying and therefore, determines the contributions of the surrounding points to the average value.

APPENDIX C

Averaged Flow Structure

Calculation of the averaged quantities was performed according to the equations listed in the flowing table. Each averaged parameter was calculated at each spatial coordinate (x,y) by considering the average of all instantaneous values (x,y). The terminology for each of the averaged parameters and the dimensionless equation employed to determine the averaged parameter as follows:

$<V> \equiv$ averaged (or mean) total velocity

$$< V > \equiv \frac{1}{N} \sum_{n=1}^{N} V_n (x, y)$$

$<u>$ = averaged value of streamwise component of velocity

$$< u > \equiv \frac{1}{N} \sum_{n=1}^{N} u_n (x, y)$$

$<v>$ = averaged value of transverse component of velocity

$$< v > \equiv \frac{1}{N} \sum_{n=1}^{N} v_n (x, y)$$

$<\omega>$ = mean value of vorticity

$$< \omega > \equiv \frac{1}{N} \sum_{n=1}^{N} \omega_n (x, y)$$

u_{rms} = root-mean-square of u component fluctuation

$$u_{rms} \equiv < u >_{rms} \equiv \left[\frac{1}{N} \sum_{n=1}^{N} [u_n (x, y) - < u(x, y) >]^2 \right]^{\frac{1}{2}}$$

v_{rms} = root-mean-square of v component fluctuation

$$v_{rms} \equiv \; <v>_{rms} \; \equiv \left[\frac{1}{N} \sum_{n=1}^{N} [v_n(x,y) - <v(x,y)>]^2 \right]^{1/2}$$

$<u'v'>$ = averaged value of Reynolds stress correlation

$$<u'v'> = \frac{1}{N} \sum_{n=1}^{N} [u_n(x,y) - <u(x,y)>][v_n(x,y) - <v(x,y)>]$$

$<u'w'>$ = averaged value of Reynolds stress correlation

$$<u'w'> = \frac{1}{N} \sum_{n=1}^{N} [u_n(x,y) - <u(x,y)>][w_n(x,z) - <w(x,z)>]$$

TKE= a mean Turbulent Kinetic Energy (TKE) value

$$TKE = \frac{1}{2}(\overline{u'^2} + \overline{v'^2} + \overline{w'^2})$$